IOWA STATE UNIVERSITY
Digital Repository

2014

Development of matrix-assisted laser desorption ionization-mass spectrometry imaging (MALDI-MSI) for plant metabolite analysis

Andrew Korte
Iowa State University

Follow this and additional works at: https://lib.dr.iastate.edu/etd

Part of the Analytical Chemistry Commons

www.manaraa.com

Development of matrix-assisted laser desorption ionization-mass spectrometry imaging (MALDI-MSI) for plant metabolite analysis

by

Andrew R. Korte

A dissertation submitted to the graduate faculty

in partial fulfillment of the requirements for the degree of

DOCTOR OF PHILOSOPHY

Major: Analytical Chemistry

Program of Study Committee:
Young-Jin Lee, Major Professor
R. Sam Houk
Basil Nikolau
Emily Smith
Patricia Thiel

Iowa State University

Ames, Iowa

2014

.

TABLE OF CONTENTS

ACKNOWLEDGMENTS

ABSTRACT

This thesis presents efforts to improve the methodology of matrix-assisted laser desorption ionization-mass spectrometry imaging (MALDI-MSI) as a method for analysis of metabolites from plant tissue samples. The first chapter consists of a general introduction to the technique of MALDI-MSI, and the sixth and final chapter provides a brief summary and an outlook on future work.

The second chapter (following a general introduction) illustrates how MALDI-MSI of metabolites can be combined with genomics knowledge to infer functional genomic information. Wild-type *Arabidopsis* flower petals were investigated for their content of three flavonoids (kaempferol, quercetin, and isorhamnetin) and their glucosides, and compared to a well-understood flavonoid mutant (*tt7)*. Spatially non-uniform accumulation/depletion of flavonoids is observed between the wild-type and mutant, and metabolite abundances are compared to infer information about localized gene expression.

The third chapter demonstrates a novel small molecule application for a matrix previously used for MALDI-MSI of lipids (1,5-diaminonaphthalene, DAN). DAN was compared to other common MALDI matrices for its efficiency in ionization of several plant metabolite standards, and was found to be comparable or superior for all tested metabolites. DAN was then applied to image a range of classes of metabolites from a cross-section of corn leaf.

The fourth chapter presents a novel acquisition method, in which high-mass resolution and tandem MS scans are acquired in alternating polarities during a single

MALDI-MSI experiment. This methodology yields highly information-rich datasets, allowing for the generation of images from either high-resolution, accurate mass measurements or specific MS/MS or MS^n transitions in both polarities, greatly expanding the number of detectable metabolites.

The fifth chapter describes modifications made to the instrument laser optics to significantly enhance the achievable spatial resolution for MALDI-MSI on the system. A combination beam expander/spatial filter and aspheric focusing optics are used to reduce the laser spot size at the sample surface. This high-resolution configuration is then used to image metabolites from a corn leaf cross-section at 5 µm resolution, revealing single-cell metabolite localizations within the tissue.

CHAPTER 1

GENERAL INTRODUCTION

Background

Mass spectrometry is a widespread and powerful technique for the chemical analysis of biological tissues. It provides versatility, selectivity, and high sensitivity. When combined with separation techniques such as chromatography, it can provide reliable identification and quantification of compounds from complex mixtures[1]. Mass spectrometry has been applied to analysis of a vast range of biologically-relevant sample types and compounds of interest, including sugars[2], lipids[3], peptides and proteins[4], drugs of abuse[5], nucleotides and nucleosides[6], and many more.

Depending on the protocol used, mass spectrometry analysis of biological tissue can involve a number of steps, including sample harvesting/collection, homogenization, extraction, centrifugation, enrichment/cleanup, derivitization, chromatographic separation, and finally detection. While these methods are well-established and reliable, the numerous processing steps destroy any information relating to the spatial distribution of analytes.

Mass spectrometry imaging (MSI) is a technique that seeks to utilize the analytical advantages of mass spectrometry (versatility, selectivity, and sensitivity) while preserving the spatial information inherent in the sample. MSI has seen application to many of the same types of tissues and compounds as bulk tissue analysis, and a number of useful reviews are available[7-12].

The most crucial step in mass spectrometry imaging is ionization of compounds of interest from the tissue sample. A number of ionization techniques have been developed for or adapted to MSI, the most common being matrix-assisted laser desorption ionization (MALDI), secondary ion mass spectrometry (SIMS), desorption electrospray ionization (DESI), and laser ablation-electrospray ionization (LAESI). The principles and relative advantages and disadvantages of these processes are discussed by Lee et al[10].

Of these techniques, MALDI is the most common and is the focus of this work. In MALDI-MSI, a matrix is applied to the surface of the sample is irradiated with a laser. The matrix serves to absorb the laser energy, causing local heating and desorption of matrix and sample material. A fraction of desorbed compounds are ionized, either within the tissue prior to desorption or in gas-phase reactions in the plume generated by laser irradiation[13]. These ions are passed further into the instrument for analysis. Like the other ionization methods used for MSI, MALDI represents a compromise among several factors, including achievable spatial resolution, softness of ionization (the extent to which ions fragment before detection), and required sample preparation[14].

MALDI-MSI can be performed in one of two different modes: microscope mode or microprobe mode. In microscope mode, ions are generated from a large region on the surface of the sample and transmitted to a position-sensitive detector with their spatial distribution preserved. Ions therefore reach the detector in a spatial pattern representative of their distributions within the tissue, and images can be generated based on the positions where they strike the detector[15]. In microprobe mode, by far the more common technique, only a small region of the tissue is probed for each spectrum (or image pixel), and images are generated by

extracting the intensity of a given signal from the spectra and plotting it as a function of x-y position on the tissue[16].

Although microscope mode typically provides faster acquisition and decouples the achievable spatial resolution from the diffraction limit of the laser[17], microprobe mode allows for the use of higher-resolution mass analyzers such as FT-ICR or Orbitrap. It is also compatible with MS techniques that provide additional chemical information, such as ion mobility spectrometry or tandem mass spectrometry. For the purposes of this dissertation, the work and discussion to follow will focus on the microprobe mode.

The majority of the applications of MSI demonstrated thus far have been for investigation of animal tissues. Plant tissues, however, provide an equally intriguing system for study, and some efforts have been made to study metabolites in plant tissue by MSI[18-25]. Plant metabolism is highly complex; it has been estimated that the plant kingdom may make use of as many as 200,000 distinct metabolites[26]. Additionally, plant metabolism is often highly localized, with metabolite content varying significantly between organs and tissue types[27]. Coupling the chemical selectivity of mass spectrometry to spatial sampling for imaging provides a powerful tool for the investigation of plant metabolism.

The focus of this work, therefore, is to develop MALDI-MSI into a more powerful and more versatile tool for the investigation of plant metabolic biology. The following work presents a number of advances regarding this objective, and addresses a range of topics within the scope of MALDI-MSI: applications, sample preparation, acquisition, and instrumentation.

MALDI-MSI: General Workflow

The workflow for a typical microprobe MALDI-MSI experiment of the kind described in this dissertation is illustrated in Figure 1, and is described below. An in-depth procedure describing tissue preparation and MALDI-MSI analysis is provided in the Appendix.

Immediately after tissue harvesting, the sample is flash-frozen in liquid nitrogen. For delicate tissues, such as the leaves used in chapter 5 of this work, the sample is simultaneously embedded in a supporting medium to allow for cutting of thin sections. The tissue is placed into a mold and the embedding solution is poured into the mold. The mold is then floated on liquid nitrogen to rapidly freeze the sample and embedding medium.

After freezing, the tissue/embedding medium block is transferred to a chamber (cryostat) that has been pre-cooled to a suitable temperature for cutting (approx. −20 °C). The tissue is allowed to equilibrate to the cryostat temperature, then thin (~5-50 µm) sections are cut from it (cryosectioning). These sections are either mounted onto glass slides or collected on adhesive tape. The tissues are kept frozen and freeze-dried to provide an intact, dry tissue section for analysis. Rapid freezing after harvest and maintaining the samples at subzero temperature until freeze-drying is critical in order to avoid turnover of metabolites as a result of tissue damage[28]. If the sample to be investigated is the surface of an intact tissue, as in Chapter 2 of this work, embedding and sectioning are not needed and the sample is simply vacuum-dried.

Next, a MALDI matrix is applied to the surface of the section. For most organic matrices, this can be accomplished by sublimation-vapor deposition, in which the matrix is heated under

vacuum and allowed to condense onto the sample. For matrices not amenable to sublimation

(e.g. inorganic nanoparticles), application can be accomplished by spraying[20] or sputter-

coating[29].

Following matrix application, the sample is inserted into the mass spectrometer, and a

series of points over the sample surface are irradiated by a focused laser beam (the microprobe

mode described above). At each of these points, a mass spectrum is recorded and stored.

After the defined area is scanned, images for specific *m/z* can be reconstructed from the

intensity of those signals at each x-y position.

Dissertation Organization

This dissertation is divided into six chapters.   The first chapter, above, serves as a

general introduction to the technique of MSI and provides context for our efforts to develop

the technique for the analysis of plant metabolites. Chapters two to four are reproductions of

papers published in peer-reviewed journals. The second chapter presents an application of

MALDI-MSI to *Arabidopsis* surface metabolites, and demonstrates how metabolite MSI can be

used to infer functional genomic information. Chapter three describes our work on the

adaptation of a MALDI matrix previously used for lipids to target small metabolites of interest

for plant tissue imaging. The fourth chapter details an instrumental methodology developed to

increase the chemical information that can be obtained from an imaging experiment performed

on a single tissue section. Chapter five presents modifications to the beam delivery optics to

reduce the laser spot size at the sample surface to ~5-6 µm, and the use of this modified system

for single-cell level imaging of corn leaf tissues. The sixth and final chapter summarizes the

work performed and provides outlook for future work and applications of the developed

instrumentation and methodologies.

Figure
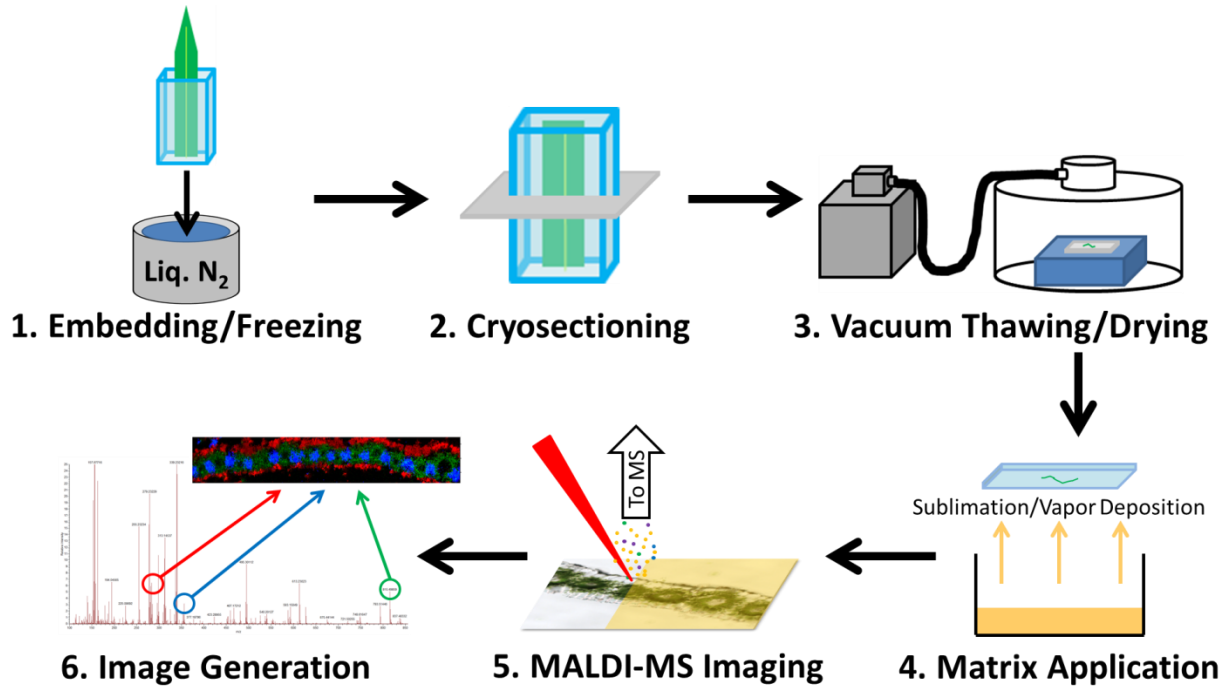
Figure 1. Sample workflow for a MALDI-MSI experiment.

CHAPTER 2

MASS SPECTROMETRIC IMAGING AS A HIGH-SPATIAL RESOLUTION TOOL FOR FUNCTIONAL GENOMICS: TISSUE-SPECIFIC EXPRESSION OF *TT7* INFERRED FROM HETEROGENEOUS DISTRIBUTION OF METABOLITES IN *ARABIDOPSIS* FLOWERS

Andrew R. Korte, Zhihong Song, Basil J. Nikolau, and Young Jin Lee

Abstract

Laser desorption/ionization (LDI) mass spectrometry imaging (MSI) was used to acquire chemical images of flavonoid metabolites on the surface of wild-type and mutant (tt7) Arabidopsis thaliana flowers. Flavonoids were localized to the petals and carpels of flowers, with tissue heterogeneity in the petals. Specifically, kaempferol and/or its glycosides were abundant in the distal region of petals and quercetin and its downstream flavonoids were highly enriched in the more proximal region of petals. As a result of a mutation in the TT7 gene which blocks the conversion of dihydrokaempferol to dihydroquercetin, the downstream metabolites, quercetin, isohamnetin, and their glycosides, were not observed in the mutant flowers. Instead, the metabolites in an alternative pathway, kaempferol and/or its glycosides, were as highly abundant on the proximal region of the petals as in the distal region. In addition, the combined flavonoid amounts on the proximal region of petals in the wild-type are almost

equivalent to the amounts of kaempferol and/or its glycosides in the mutant. This strongly suggests that the expression of the TT7 gene is localized on the proximal part of the petal while the other genes in the upper stream pathway are evenly expressed throughout the petal. Most importantly, this work demonstrates MSI of metabolites can be utilized for the localization of gene expression.

Introduction

Mass spectrometry imaging (MSI) is a technique that has emerged over the last decade as a complement to other molecular methods for localizing the spatial distribution of biochemicals[30]. MSI involves the desorption of molecules directly from a tissue surface and subsequent analysis of the desorbed molecules by mass spectrometry. Desorption is commonly accomplished by means of a laser[16], ion beam[31], or solvent spray[32], with each method offering advantages and disadvantages[7]. Regardless of the desorption method, MSI provides several advantages over traditional localization methods that require either dissection or fractionation, followed by extraction and gas chromatography (GC)- or liquid chromatography (LC)-MS analysis. It provides high-resolution spatial information that cannot be reasonably achieved by dissection or fractionation[33]. For example, Römpp et al. recently demonstrated 5 μm resolution on mouse and human tissues for a matrix-assisted LDI (MALDI) MSI system[34]. MSI requires less tissue sample than a typical dissection/extraction experiment and a complete dataset can be obtained from a single sample, while GC- or LC- based methods often require numerous samples per dataset[35]. In general, MSI is also less labor-intensive than other

spatially-resolved techniques such as microdissection, because it does not require manual collection and separation[36].

MSI has seen extensive applications with human and animal tissues, including lipid mapping[37], drug distribution[38], and cancer biomarkers[39]. Applications to plants, by contrast, have been relatively limited. Cha et al. acquired chemical images of flavonoids and epicuticular surface lipids on *Arabidopsis thaliana* leaves and flowers and observed the effect of light exposure on flavonoid accumulation[19, 40]. Hölscher et al. demonstrated matrix-free imaging of *Arabidopsis* and *Hypericum* metabolites at a 10 µm spatial resolution[41]. Anderson et al. used MSI to examine the distribution of a pesticide, nicosulfuron, in sunflower stems[42]. Vertes' group has applied laser ablation electrospray ionization (LAESI)-MS to 3-dimensional imaging of Peace lily and Zebra plant metabolites[43]. We have demonstrated high spatial resolution MSI of a whole flower, imaging metabolites to the level of a single cell[20]. We recently developed and applied a multiplex MS imaging methodology to differentiate structural isomers of flavonoids in *Arabidopsis*. This method simultaneously obtains high mass resolution spectra and high spatial resolution images in a single experiment[23]. Recent review article provides detailed information about MSI technology as a tool study plant metabolites[10].

Arabidopsis is a staple species for investigating plant biology, and has been used as a model organism for nearly 30 years[44]. For this reason, it presents an excellent system for the development and demonstration of MSI in plants. Sequencing of the *Arabidopsis* genome was completed in 2000[45]. Baerenfaller et al. conducted an extensive proteomics-based investigation on *Arabidopsis* with organ-level specificity, noting significant qualitative and quantitative protein expression differences among several tissues sampled[46]. Analogous

transcriptomics datasets provide access to the global expression potential of the *Arabidopsis* genome[47, 48]. Despite these large scale omics efforts, there is much about the metabolism of *Arabidopsis* that remains to be discovered. Most of all, the functions of a large portion of *Arabidopsis* genes remain unknown, owing largely to the fact that a majority of metabolites in this organism are unidentified[49].

Identification and characterization of these metabolites is of critical importance to further understanding of the biology of *Arabidopsis*, and by extension of plant biology in general. One way of studying unknown gene functions and their metabolomic effect is through large scale profiling of plants that carry knock-out alleles (e.g., www.plantmetabolomics.org[50]). Comprehensive understanding of gene functions and metabolism however, require knowledge of spatial distribution as well as metabolite composition. Current metabolomic profiling procedures are based on traditional dissection and digestion/extraction methods, which allows for only organ-level localization data[27]. MSI offers the potential to efficiently map the localization of metabolites at the level of a single-cell[20], making it a promising tool for the understanding of functional genomics with high spatial precision.

The present study is intended to evaluate the utility of LDI-MSI in plant functional genomics by studying the highly-localized distribution of metabolites in an *Arabidopsis* mutant. A mutant associated with the biosynthesis of flavonoids, *tt7*, was chosen for the current study because of the high abundance of flavonoids on the surface of flower petals and the negligible impact of the mutation on overall metabolism. Flavonoids are a class of plant secondary metabolites that are produced from chalcones and have been shown to act in hormone signaling, ultraviolet protection, and cell development[51], and they primarily exist in tissues as

glycosylated derivatives[35]. The *TT7* gene codes for flavonoid 3'-hydroxylase (F3'H), an enzyme responsible for the 3'-hydroxylation of flavonoids, such as the conversion of dihydrokaempferol to dihydroquercetin. The *TT7* mutation results in a deficiency in F3'H[52], effectively blocking the production of the flavonoids quercetin and isorhamnetin and their glycoside derivatives (Scheme 1). In this study, we have compared MS images of whole flowers and petals of wild-type and *tt7* mutant plants, to investigate the consequences of the *tt7* mutation at high spatial resolution. We have also investigated the difference between the use of colloidal graphite as a matrix and matrix-free LDI.

Experimental

Chemicals

Colloidal graphite aerosol spray was obtained from Alfa Aesar (Ward Hill, MA, USA). Murashige and Skoog basal salt mixture, HPLC grade acetonitrile and methanol, and flavonoid standards such as rutin, quercitrin (quercetin rhamnoside), kaempferol, quercetin, and apigenin were obtained from Sigma-Aldrich (St. Louis, MO, USA). All other chemicals were purchased from Fisher Scientific (Fairlawn, NJ, USA).

Plant growth conditions

Arabidopsis thaliana ecotype Landsberg *erecta* (Ler-0) and *tt7* mutant (ABRC genetic stock CS88, which carries the *tt7-1* allele) were obtained from the Arabidopsis Biological Resource Center (Columbus, OH). Seeds were sterilized and sown on Murashige and Skoog

basal salt mixture (MS) media in Petri dishes. The dishes were placed in the growth room for 15 days after breaking seed dormancy by maintaining them at 4°C for 3 days. On the 19th day the seedlings were transferred to soil in 5 cm $\times$ 5 cm pots for continuous growth.   Plants were then maintained at 24°C and ambient humidity with an illumination of 85 µE m^{-2}s^{-1} until collection. Whole flowers and petals used for imaging were collected 30 to 32 days and 40 to 42 days after sowing, respectively. Flowers for extraction and LC-MS quantification were collected 42 to 45 days after sowing.

MS imaging sample preparation

Petals and whole flowers were immobilized on stainless steel sample plates with conductive double-sided tape (3M, St. Paul, MN, USA). The application of very light, uniform pressure with the tape backing and a soft stream of helium gas made it possible to attach the samples with minimal damage from forceps or other equipment. The plates with the samples attached were then placed into a vacuum chamber and dried at ~50 torr for 30 minutes.

A commercial airbrush (Aztek A470; Testor, Rockford, IL, USA) was modified to an oscillating spray device[53] by replacing the inner spraying tip with a fused silica capillary (100 µm i.d., 360 µm o.d.; Polymicro Technology, Phoenix, AZ, USA) for homogeneous matrix application. Colloidal graphite aerosol spray was diluted 8:1 with 2-propanol. This solution was transferred to the modified airbrush through a syringe pump (Fisher Scientific, Pittsburgh, PA, USA) and sprayed onto plant tissues by nebulizing with N$_2$ gas at a pressure of 40 psi. The distance between the tip of the capillary and the sample plate was kept at 9 cm. Matrix flow

rate was set at 50 µL min^{-1} and a total volume of 300 µL was applied to each sample.

Mass spectrometry imaging

MS images were acquired using a MALDI linear ion trap–Orbitrap hybrid mass spectrometer (MALDI LTQ-Orbitrap Discovery; Thermo Scientific, San Jose, CA, USA). Images were mostly collected using the linear ion trap rather than the higher-resolution Orbitrap to reduce acquisition time. The mass spectrometer was equipped with an intermediate-pressure MALDI source using a nitrogen laser (MNL 100; Lasertechnik Berlin, Berlin, Germany) with an output wavelength of 337 nm, maximum pulse energy of 80 µJ, and repetition rate of 60 Hz. A 3-mm aperture was placed in the beam path to reduce the spot size at the sample surface to 35-40 µm, as determined by observation of burn marks on a thin film of α-cyano-hydroxycinnamic acid.

Optical images were obtained using the camera integrated into the MALDI source. MS images were collected in negative ion mode with a 50 µm raster step size. Laser power and the number of sweep shots (shots fired without collecting spectra, needed for some graphite-coated samples to remove excess matrix over the sample surface) were optimized for individual experiments. Each spectrum was obtained from two laser shots, and 10 spectra were averaged for each pixel. Images were generated using ImageQuest (v.1.0.1; Thermo Scientific).

LC-MS quantification

300 to 500 mg of whole flower samples was pulverized in a mixer mill (MM301, Retsch,

Germany). Two ml of hot methanol (60 °C) was added and the solution was spiked with apigenin (13.5 µg) as an internal standard for the normalization of total amounts injected. The solution was then heated at 80 °C for 60 minutes and sonicated for 30 minutes. The extracts were centrifuged at 13,000 x g for 5 minutes to pellet insoluble debris and the supernatant was subjected to LC-MS analysis on an Agilent (Palo Alto, CA, USA) 1100 LC/MSD ion trap system at a flow rate of 0.4mL min^{-1}. Chromatography was conducted with a Phenomenex Luna Phenyl column (150 x 2.0 mm, 5 µm particle size) and an elution gradient from 17% to 100% Solvent B in 47 minutes. (Solvent A: 10 mM NH_4OAc, pH 5; Solvent B: 9:1 CH_3CN:MeOH). The mass spectrometer was operated in negative ion mode in electrospray ionization with a source voltage of 3.0 kV, skimmer at 40.0 V, capillary exit at 153.9 V, nebulizer pressure of 35.0 psi, dry gas (nitrogen) flow of 10.0 L/min, drying gas temperature of 350 °C, and a scan range of m/z 100-1000 at two scans per second.

LC-MS data sets were analyzed with Bruker DataAnalysis version 4.2. Flavonoid and flavonoid glycosides were identified either by comparison with standard compounds or by referencing previous work[40, 54]. Relative quantification was performed by normalizing the peak area of the extracted ion chromatogram from each flavonoid to that of the internal standard apigenin.

Results and Discussion

Whole flower imaging

Fig. 1 shows optical images and MS images for kaempferol, quercetin, and isorhamnetin aglycones of wild-type and *tt7* flowers with colloidal graphite as a matrix. Examination of the spectra indicated that flavonoids were the predominant species observed in both wild-type and *tt7* flowers and were localized to the petals and carpels, as observed previously[40]. Representative mass spectra from the middle region of petals are shown in Fig. 2, and mass spectra from carpels are provided in the supplementary information (Fig. S1). Kaempferol (K, *m/z* 285.1) is localized mostly in the petals, especially from the center to the distal end of the petals, and along the carpels of both flowers. Quercetin (Q, *m/z* 301.1) and isorhamnetin (I, *m/z* 315.1) are seen nearer the proximal end of wild-type petals, in good agreement with previous work[23, 40, 41]. Quercetin and isorhamnetin, however, are not detectable in the *tt7* flower, suggesting that the synthesis of these compounds is almost completely blocked in the *tt7* mutant flowers. The distribution of glycosylated derivatives (not shown) is similar to that of the aglycones. Flavonoid signals (kaempferol, quercetin, and isorhamnetin in WT, only kaempferol in *tt7*) were also observed along the carpel, which was not previously detected when an oversampling method was used to reduce the sampling size[40], suggesting better sensitivity is possible with the use of a narrow laser beam.

The flavonoids studied herein all exhibit strong absorption at the laser wavelength used, and thus can be imaged without the use of a matrix[23, 41]. Images were obtained both using colloidal graphite as a matrix and with no added matrix. Both conditions produced adequate

signal for imaging of all flavonoid aglycone and glycoside species. However, use of colloidal graphite as a matrix was found to consistently improve glycoside signal relative to aglycone signal (Fig. 2). This suggests that although flavonoids can be detected without a matrix, the presence of a matrix reduces the fragmentation by minimizing direct photon absorption (See next section for more discussion about in-source fragmentation of flavonoid glycosides). Graphite, however, produces a background consisting of C_n^- clusters up to about m/z 400, which may cause interferences with some analytes. Additionally, there is a space-charge effect with colloidal graphite as a result of overfilling the ion trap under the laser conditions used, resulting in the apparent mass shift, particularly at low m/z values (Fig. 2b and 2d).

The difficulty of firmly and flatly attaching such organs as stamens and carpels without damaging them, and the tendency of intact flowers to partially detach from the surface during the drying step led to inconsistent ion yield from the surfaces of these structures. This inconsistency complicates quantitative comparison between samples, and therefore further studies focused on detached petals, which could be more easily and reliably fixed to the MALDI plate.

LC-MS quantification and glycoside fragmentation

LC-MS analysis was performed for quantitative comparison of flavonoids in extracts prepared from whole flowers of wild-type and *tt7* plants (Fig. 3). Absolute quantification is not plausible because most of the flavonoids are not commercially available, particularly glycosides; hence, this study is designed for the relative comparison of each flavonoid between wild-type and tt7. As in the MSI experiments, quercetin and isorhamnetin and their glycoside derivatives

were not detected in extracts from *tt7* flowers. Instead, an slightly but significantly increased

abundance of kaempferol and its glycosides was observed, indicating that the block in *TT7*

functionality leads to the alternative metabolism of the TT7 substrate (i.e., dihydrokaempferol).

In contrast to our MSI experiments however, the LC-MS results indicate that the vast majority

of flavonoids exist as glycosides, especially as diglycosides, with the aglycone forms of

kaempferol, quercetin, and isorhamnetin being undetectable in both wild-type and *tt7* flowers.

This result is similar to an LC-MS study of flavonoid extracts in *Arabidopsis* by Yonekura-

Sakakibara and coworkers[55]. They could not detect quercetin, isorhamnetin, or their glycoside

derivatives in *tt7* or kaempferol aglycone in wild-type. They also noted an increased amount of

kaempferol glycosides in *tt7* compared to the wild-type. Previous flavonoid LDI-MSI has also

shown a similar result, namely high abundance of aglycones as compared to glycosides on

Arabidopsis petal surfaces[23, 40].

This discrepancy in the relative glycoside-aglycone abundance between LC-MS and MSI

methods suggests two possibilities. First, it could be attributed to a difference in sampling

depth between LC-MS and LDI-MS. LC-MS experiments were performed on extracts of

homogenized flowers, while LDI-MS samples only the flower and petal surface (to a depth of

<1μm). Harborne and Williams reported that while flavonoids in leaves typically exist as

glycosylated species in vacuoles, they have also been observed as aglycones in the cuticle[56].

Another possibility is that the glycoside bonds fragment readily under LDI conditions. To test

this latter explanation we performed LDI-MS analysis of authentic standard compounds of

flavonoid glycosides, and confirmed that significant fragmentation of these bonds led to

decreased signal for the glycoside derivatives (Fig. S2 and Fig. S3). Specifically, the abundance

of the molecular ion of the flavonoid monoglycoside (quercetin-rhamnoside) is only ~15% and 35% of the quercetin fragment in LDI-MS, without or with graphite matrix respectively (Fig. S2b and Fig. S3b). This is similar to the ratios of flavonoid aglycones vs. monoglycosides observed in flowers shown in Fig. 2. LDI-MS of a flavonoid diglycoside standard, rutin (quercetin-3-(rhamnoside-glucoside)), also showed significant fragmentation, but the unfragmented diglycoside form was more stable (~40-60% of quercetin fragment under both conditions in Fig. S2c and Fig. S3c) than the monoglycoside (Fig. S2b and Fig. S3b). It is worth mentioning that endogeneous diglycosides in *Arabidopsis* flower (e.g., kaempferol-hexoside-rhamnoside and quercetin-hexoside-rhamnoside in Fig. 2) are known to be glycosylated in the 3- and 7-hydroxyl positions of flavonoid aglycone (i.e., kaempferol-3-O-glucoside-7-O-rhamnoside, quercetin-3-O-glucoside-7-O-rhamnoside[55]) and fragmentation of both the glycoside bonds to produce the aglycone should be even less likely.

Hence, both the explanations – differences in the flavonoid forms between surface and bulk tissue, and LDI-induced fragmentation of glycosides – might have contributed to the difference between LC-MS and LDI-MS results. Because of the uncertainty in fragmentation yields on the tissue surface and unknown fragmentation efficiency of native flavonoids with glycosides on the 3- and 7-hydroxyl positions, we cannot conclusively determine the ratios of aglycones, monoglycosides, and diglycosides present on the flower surface. However, it is most likely that the apparent high abundance of aglycones on the flower surface in LDI-MS is overrepresented, and the actual abundance of aglycones, if they are present at all, may be considerably less.

Petal imaging and flavonoid signal comparison

Fig. 4 shows the optical and MS images of flavonoids and flavonoid glycosides for wild-type and *tt7* petals using colloidal graphite as a matrix. As in the images of whole flowers, kaempferol (K, *m/z* 285.1) and its rhamnoside and hexoside-rhamnoside derivatives (K-R, *m/z* 431.1; K-H-R, *m/z* 593.1) are localized between the distal and mid parts of wild-type petals. Quercetin (Q, *m/z* 301.1) and its hexoside-rhamnoside derivative (Q-H-R, *m/z* 609.1) are localized in the proximal portion of the petal but do not extend all the way to the base of the petal. The same is true for isorhamnetin and its rhamnoside and hexoside-rhamnoside derivatives (I, *m/z* 315.1; I-R, *m/z* 461.1; I-H-R, *m/z* 623.1). Kaempferol hexoside and quercetin rhamnoside are structural isomers with an identical chemical composition ($C_{21}H_{20}O_{11}$) and both were detected in their deprotonated forms as ions of *m/z* 447.1. The image of *m/z* 447.1 shows significant intensity in both the distal (kaempferol-dominated) and proximal (quercetin/isorhamnetin-dominated) regions in wild-type petals. We have previously used tandem MS imaging to distinguish the two isomers and showed that kaempferol hexoside and quercetin rhamnoside have distinct distributions that match their respective aglycones[23].

In the *tt7* mutant petals, ion signals from quercetin, isorhamnetin, and their derivatives are undetectable above noise levels. Therefore, in these analyses the *m/z* 447.1 ion (which could be attributed to either quercetin rhamnoside or kaempferol hexoside) was solely ascribed to kaempferol hexoside. Hence, the spatial distribution of kaempferol and/or its derivatives (kaempferol rhamnoside, kaempferol hexoside, and kaempferol hexoside-rhamnoside) was different from that found in the wild-type petals. Specifically, the kaempferol derivatives extended over the proximal region of petals where quercetin and its derivatives were present in

wild-type petals. The same results were observed without the use of colloidal graphite as a matrix (Fig. S3).

For semi-quantitative comparisons of flavonoids between wild-type and *tt7* petals, the ion signal for each species was averaged over 25 pixels in each of the proximal (quercetin-dominated in wild-type plants) and distal (kaempferol-dominated) regions in three petal replicates. In these comparisons ion signals were normalized on the basis of total ion count (TIC) per pixel that was interrogated. We chose the regions where the flavonoid distributions were relatively homogeneous, as represented by the highlighted squares shown in Fig. 2. These results are shown in Fig. 5; the analogous analysis conducted without a matrix is shown in Fig. S5. As compared to the wild-type petals, kaempferol and its glycoside derivatives were significantly increased in the proximal region of *tt7* petals. The average kaempferol aglycone signal was about 4.5 times higher in *tt7* petals than in wild-type petals, and the kaempferol rhamnoside signal was nearly ten times higher in *tt7* petals. As expected from LC-MS data (Fig. 3) and whole flower LDI-MSI images (Fig. 1), quercetin and isorhamnetin and their derivatives were almost entirely absent. The apparent residual quercetin and isorhamnetin are a result of spectral noise (see Fig. 2c, d).

These MSI results can be compared to the analogous data obtained from LC-MS analysis of extracts prepared from the entire flowers. As determined by LC-MS the kaempferol-derivatives were at concentrations 1.2-1.5 times higher in *tt7* plants as compared to the wild-type (Fig. 3). This apparent quantitative difference between the MSI and LC-MS data is probably due to a combination of several reasons, but primarily the fact that the proximal region of petals where kaempferol is significantly increased represents only a small percentage

of the overall flower biomass. LC-MS data are from extracts that collectively sample the entire flower and reflect only the slight overall increase in kaempferol.

It is important to note that there are limitations to the quantification accuracy of the current method and MSI in general. The high degree of fragmentation of flavonoid glycosides makes it difficult to compare their abundances relative to the aglycones, as the glycoside fragments cannot be distinguished from the natural aglycones. Additionally, the ionization efficiency from one sample to the next, or even across a single sample, may not be uniform; thus ion signals may vary from spot to spot. Normalization to matrix or other representative ion signal can partially solve such problems[20]. In the current study, TIC was used for normalization because of the absence of such representative peaks. This allows relative comparison of each metabolite, but differences in ionization efficiency for each compound prevent absolute quantification. Co-application of suitable standard compounds with the matrix, such as isotopically-labeled synthetic metabolites, may allow for higher confidence in quantitative imaging experiments[57]. Our own testing of standard compounds, however, indicates very little difference in ionization efficiencies between kaempferol and quercetin. Hence, a relative, semi-quantitative comparison among kaempferol, quercetin, and isorhamnetin is plausible within aglycones, monoglycosides, or diglycosides.

The localization observed for kaempferol, quercetin, and isorhamnetin may offer insights into the distribution of the F3'H enzyme. The high abundance of kaempferol and kaempferol glycosides and the absence of quercetin, isorhamnetin, and derivatives thereof in the distal region of wild-type petals suggests F3'H may not be localized to that part of the petal, but may be more concentrated in the proximal region of the petal, where accumulation of

quercetin and isorhamnetin is observed. Consistent with this hypothesis is the finding that in the *tt7* mutant, kaempferol and its derivatives hyper-accumulate in the proximal region of the petal, replacing the quercetin and isorhamnetin and derivatives which normally occur in that region in the wild-type petals (Figure 4 and 5). In these *tt7* petals, the levels of kaempferol and kaempferol glycosides are comparable between the proximal and distal regions.

These findings suggest that the synthesis of dihydrokaempferol occurs fairly uniformly throughout the petal, and in the proximal region of wild-type petals ~80% is converted to dihydroquercetin by F3'H, and on to the downstream metabolites of quercetin, isorhamnetin, and their derivatives. And indeed consistent with this model, the sum of the normalized semi-quantitative ion signals of the three aglycones in the proximal region of wild-type petals gives a signal level that is comparable to the *tt7* kaempferol signal (the inset figure in Fig. 5). The same semi-quantitative comparison could be made for mono-glycosides of rhamnoside and hexoside (the inset figure of Fig. 5) and di-glycosides (not shown). Although we cannot conclusively reject the possibility that these flavonoids might migrate after synthesis, the high degree of metabolite localization on the petals suggests this is not the case. Further confirmation of this enzyme localization could be provided by the direct immunolabeling or fluorescent tagging of the F3'H enzyme itself.

Conclusions

MSI was used to map differentially-distributed flavonoid metabolites on the surface of wild-type and mutant *Arabidopsis thaliana* flowers. These data demonstrate the potential of

MSI as a tool for functional genomics. The results of the MSI experiments are in good agreement with parallel LC-MS analyses, with quercetin and isorhamnetin production being completely blocked in the *tt7* mutant. Additionally, the finding that the normally quercetin- and isorhamnetin-rich but kaempferol-poor region in wild-type petals became kaempferol-rich in the *tt7* mutant, suggests that kaempferol accumulation is an alternative metabolic fate in the absence of *TT7* functionality. The heterogeneous distribution of the largely non-mobile quercetin and isorhamnetin suggests a heterogeneous localization of the associated F3'H enzyme in wild-type plants. Moreover, the relatively homogeneous distribution of kaempferol (and its derivatives) in the *tt7* mutant petals suggests that the upstream genes in the flavonoid pathway are expressed homogeneously (or are at least non-limiting) throughout the petals. This work is the first example to demonstrate the use of MSI of metabolites as a tool for functional genomics, particularly for the localization of gene action. As new developments continue to make higher-resolution imaging possible, MSI will allow for the visualization of gene expression at the single-cell level, without the need for invasive, time-consuming fluorescent tagging or immunolabeling.
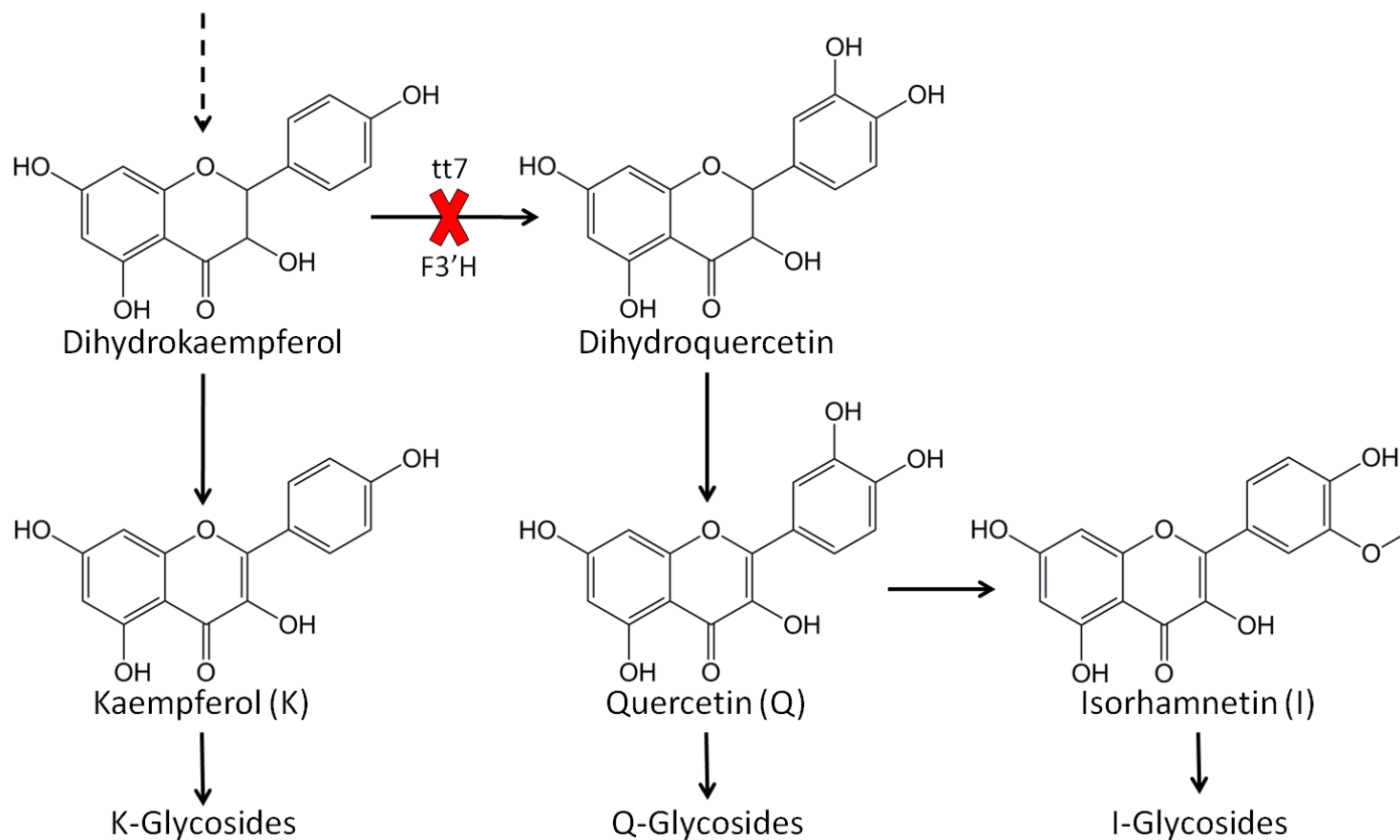
Scheme 1. Partial flavonoid synthesis pathway in *Arabidopsis thaliana*[52].
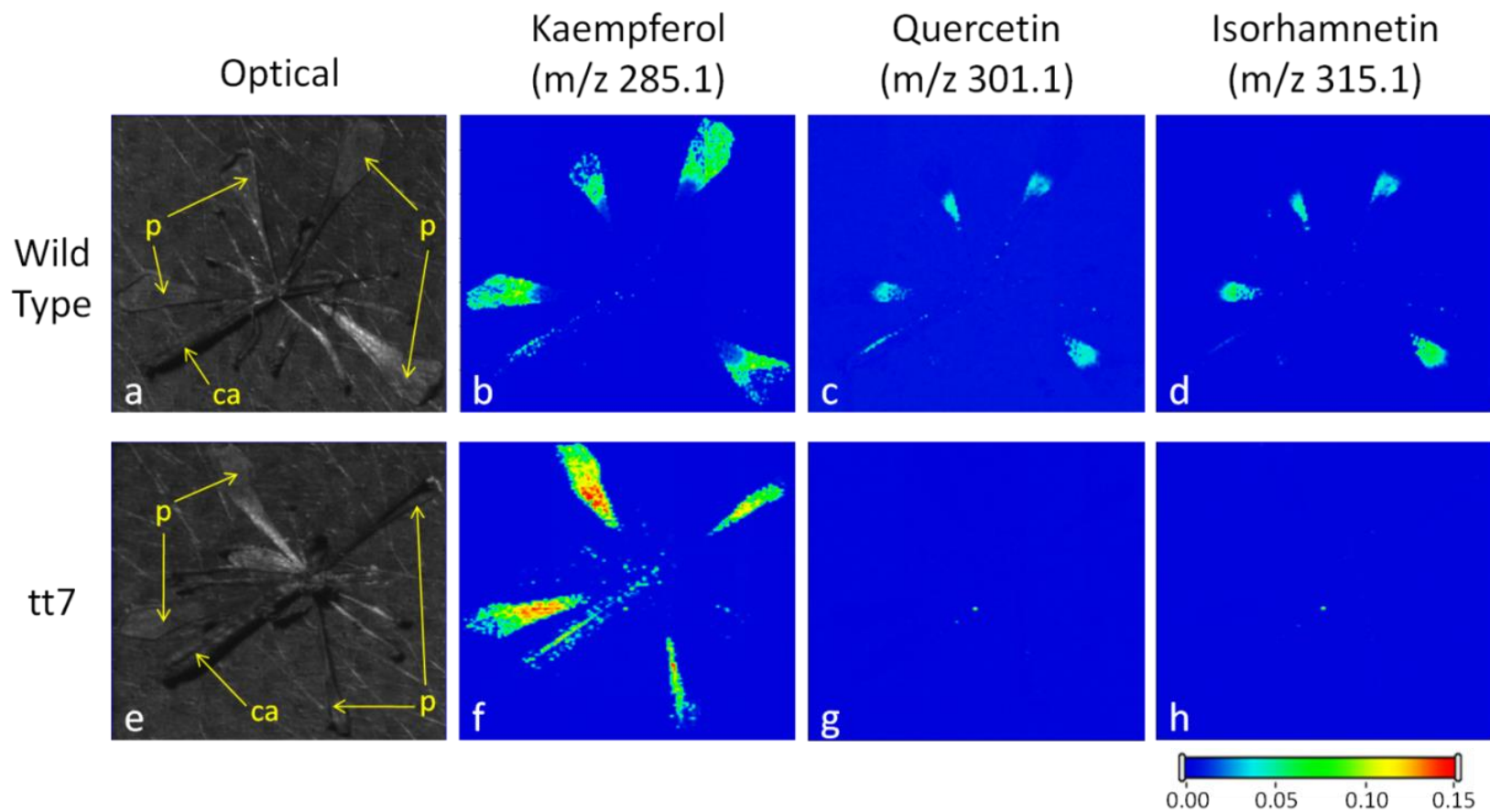
Figure 1. Flavonoid image on whole flower. Optical and MS images of whole wild-type (*a-d*) and *tt7* mutant (*e-h*) *Arabidopsis thaliana* flowers obtained using colloidal graphite as a matrix. Signals are normalized to total ion count. All plotted m/z represent the deprotonated pseudo-molecules, [M-H]⁻. Flavonoid signals are localized to the petals (p) and carpels (ca), and no flavonoid signals were observed from the other flower organs.
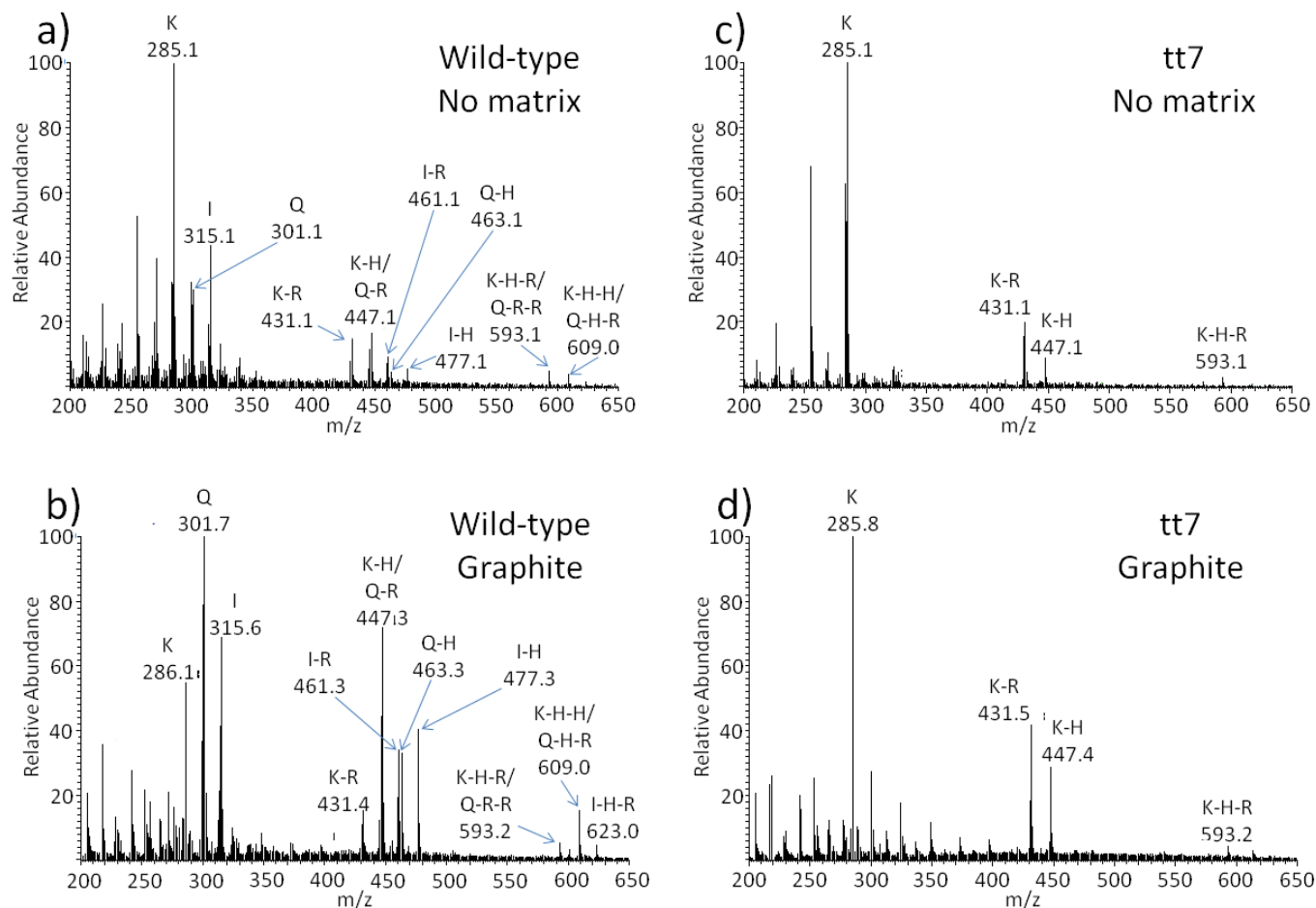
Figure 2. Mass spectra on petals. LDI-mass spectra obtained from wild-type (*a, b*) and *tt7* mutant (*c, d*) *Arabidopsis thaliana* petals without a matrix (*a, c*) and with colloidal graphite as a matrix (*b, d*). Peaks corresponding to kaempferol (K), quercetin (Q), and isorhamnetin (I) are labeled, as are their rhamnose (-R) and hexose (-H) glycosides. The spectra are from a single pixel at the region approximately 2/3 of the distance from the tip to the base of the petal where signals for kaempferol and quercetin/isorhamnetin species overlap.
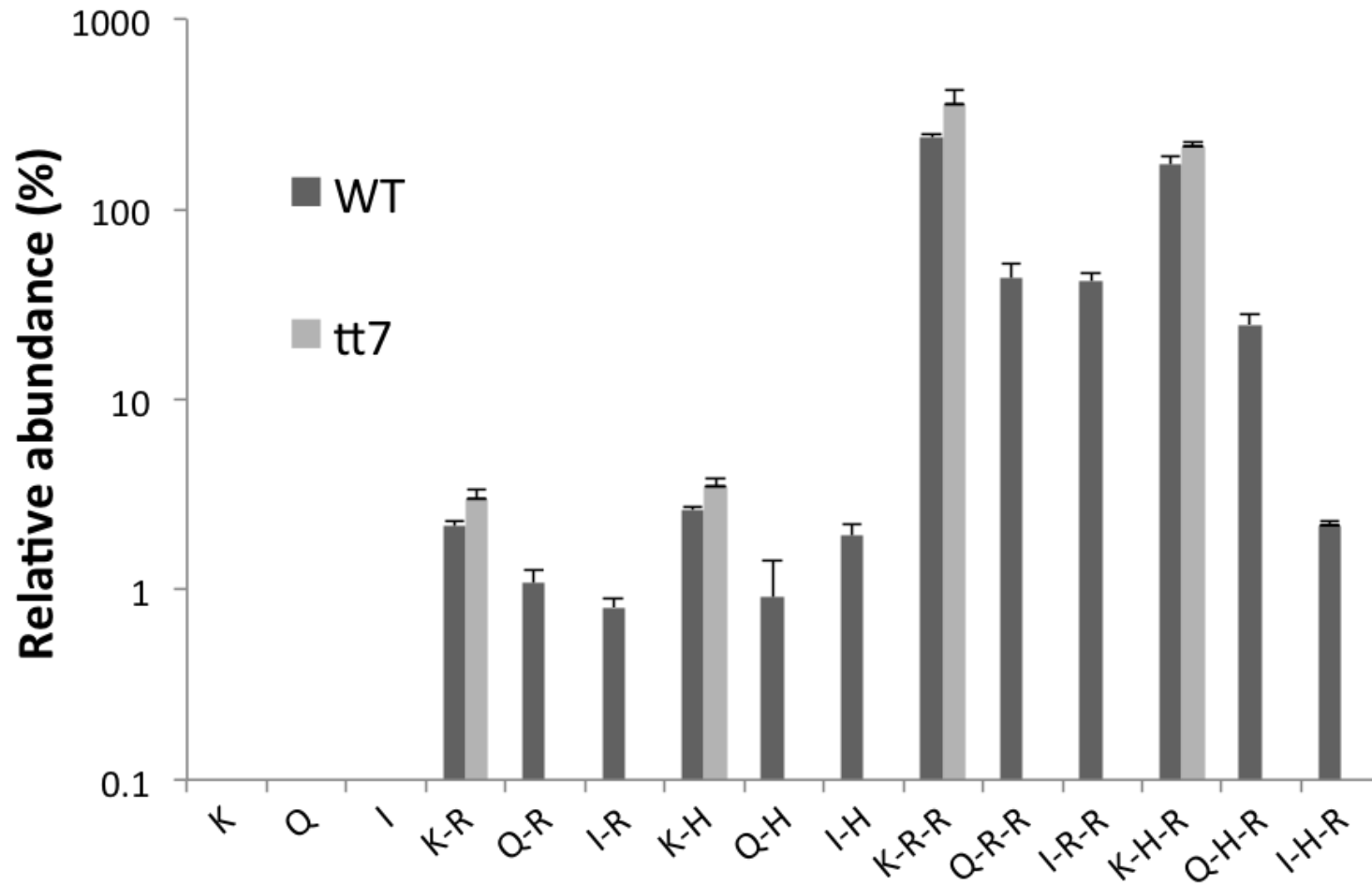
Figure 3. LC-MS Quantification of flavonoids in whole flowers. Relative amounts of several flavonoid and flavonoid glycosides in wild-type and *tt7* mutant *Arabidopsis* flowers, as determined by LC-MS analysis of extracts prepared from whole flowers. Relative abundances are calculated from the extracted ion chromatogram of each species to that of apigenin.

Figure 4. Flavonoid image on petals. Optical and MS images of wild-type (***top series***) and tt7 mutant (***bottom series***) *Arabidopsis thaliana* petals showing distributions of kaempferol (K), quercetin (Q) and isorhamnetin (I), along with their rhamnose (R) and hexose-rhamnose (H-R) glycosides. Colloidal graphite was used as a matrix and signals are normalized to total ion count (TIC). All plotted *m/z* represent the deprotonated pseudo-molecules, [M-H]⁻. The distal and proximal regions used for subsequent analysis are labeled in the optical image and black squares on the kaempferol images represent approximate regions chosen for quantitation in Fig. 5.

Figure 5. Semi-quantification of flavonoids in distal and proximal region of petals. Relative ion signals of flavonoid aglycones and glycosides in two regions of wild-type (WT) and *tt7* mutant *Arabidopsis* petals. The values are obtained from 25 pixels in each region of MS images in three petal replicates. Error bars represent one standard deviation. All signals are normalized to TIC. Data was collected with the use of colloidal graphite matrix. Inset shows a comparison of summed kaempferol, quercetin, and isorhamnetin aglycone and glycoside signals from WT petals, and kaempferol aglycone and glycoside signals from *tt7* petals. In the calculation of inset data, the *m/z* 447 ion (kaempferol hexoside/quercetin rhamnoside) was assumed to be entirely due to quercetin rhamnoside in WT, and entirely due to kaempferol hexoside in *tt7*.

Supplemental Figures
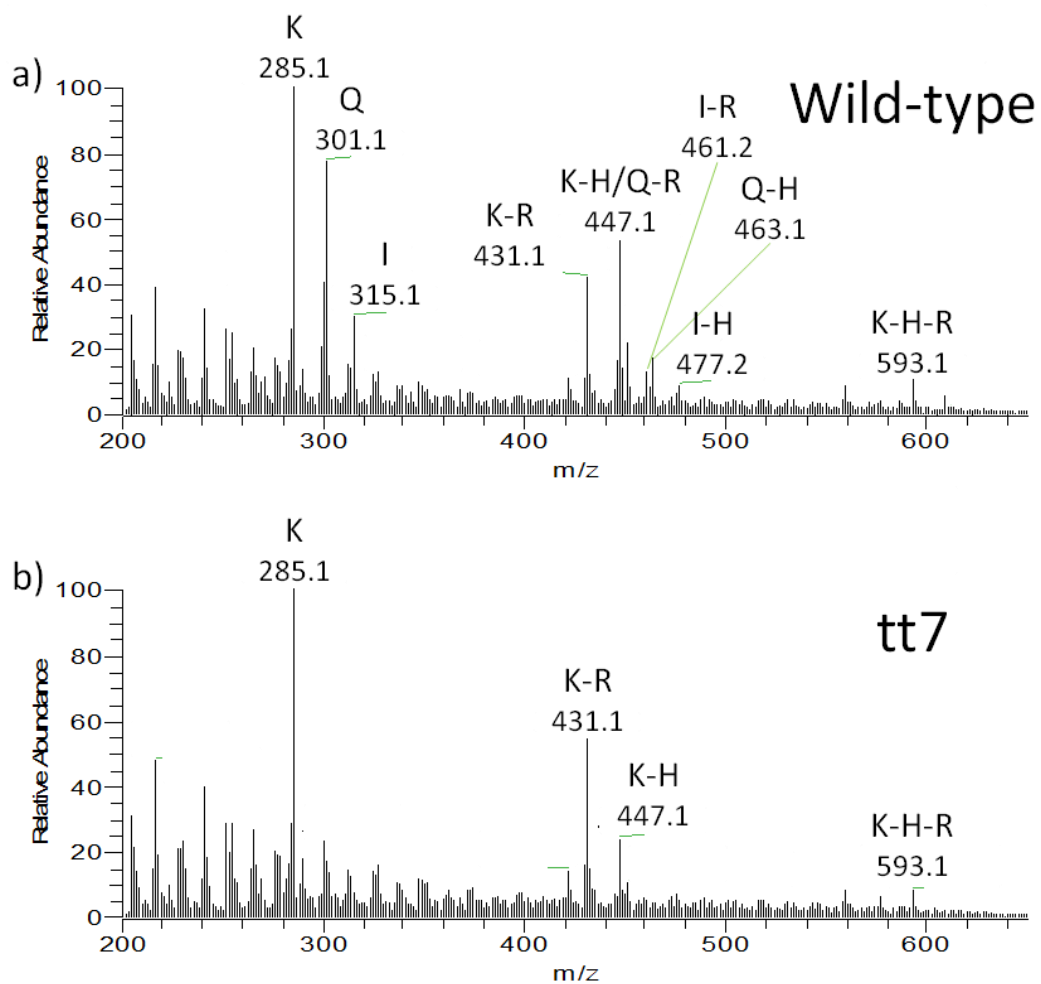
Figure S1. Mass spectra on carpels. Mass spectra taken from a single pixel in the middle of the carpels of Fig. 1. Peaks corresponding to kaempferol (K), quercetin (Q), and isorhamnetin (I) are labeled, as are their rhamnose (-R) and hexose (-H) glycosides.
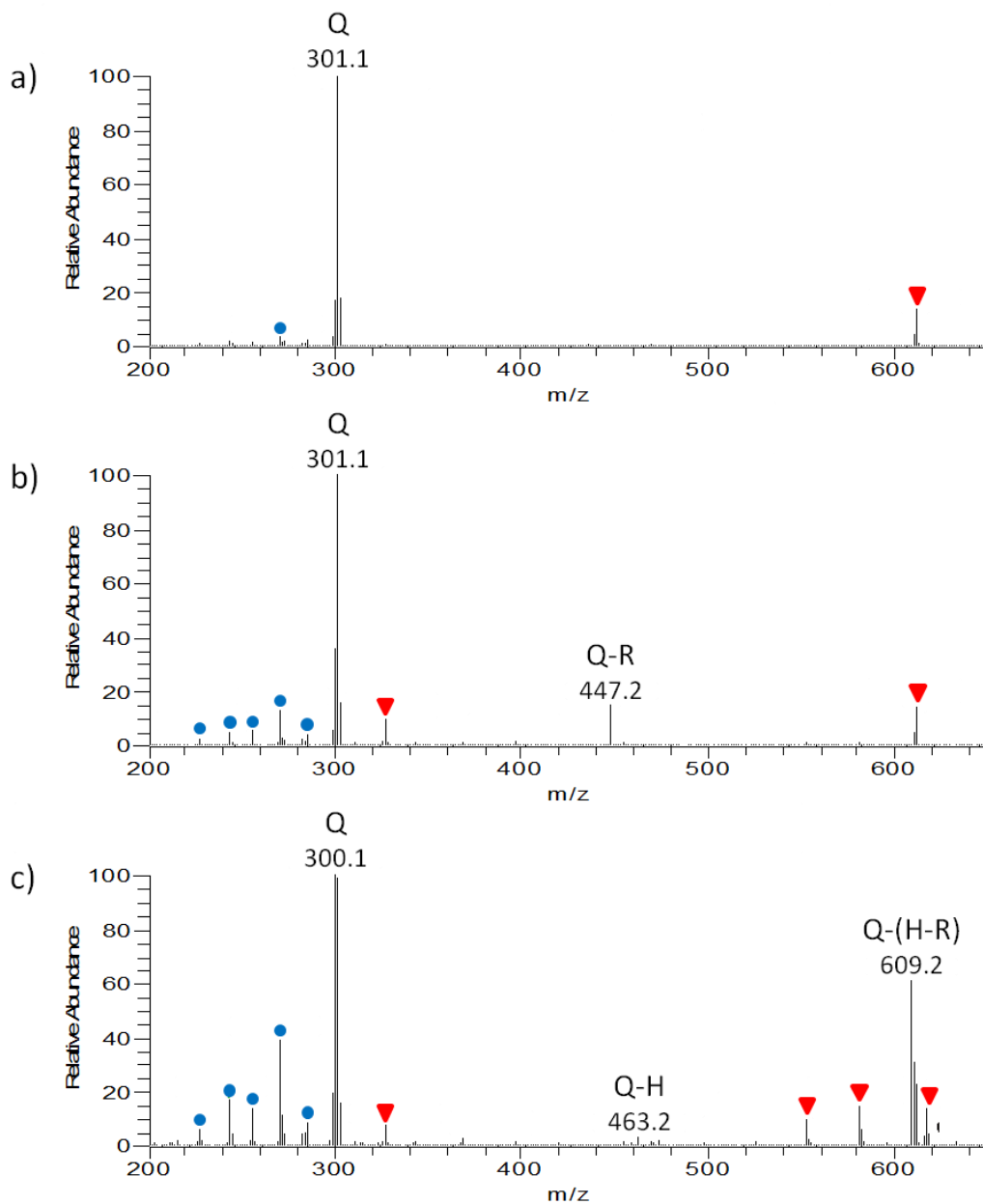
Figure S2. LDI-mass spectra of flavonoid standards without matrix. quercetin (a), quercetin rhamnoside (b), and rutin (quercetin-3-(glucoside-rhamnoside)) (c). Significant fragmentation to the aglycone is observed for the mono- and di-glycosides. Quercetin fragments (●) and contaminations (▼) are marked.
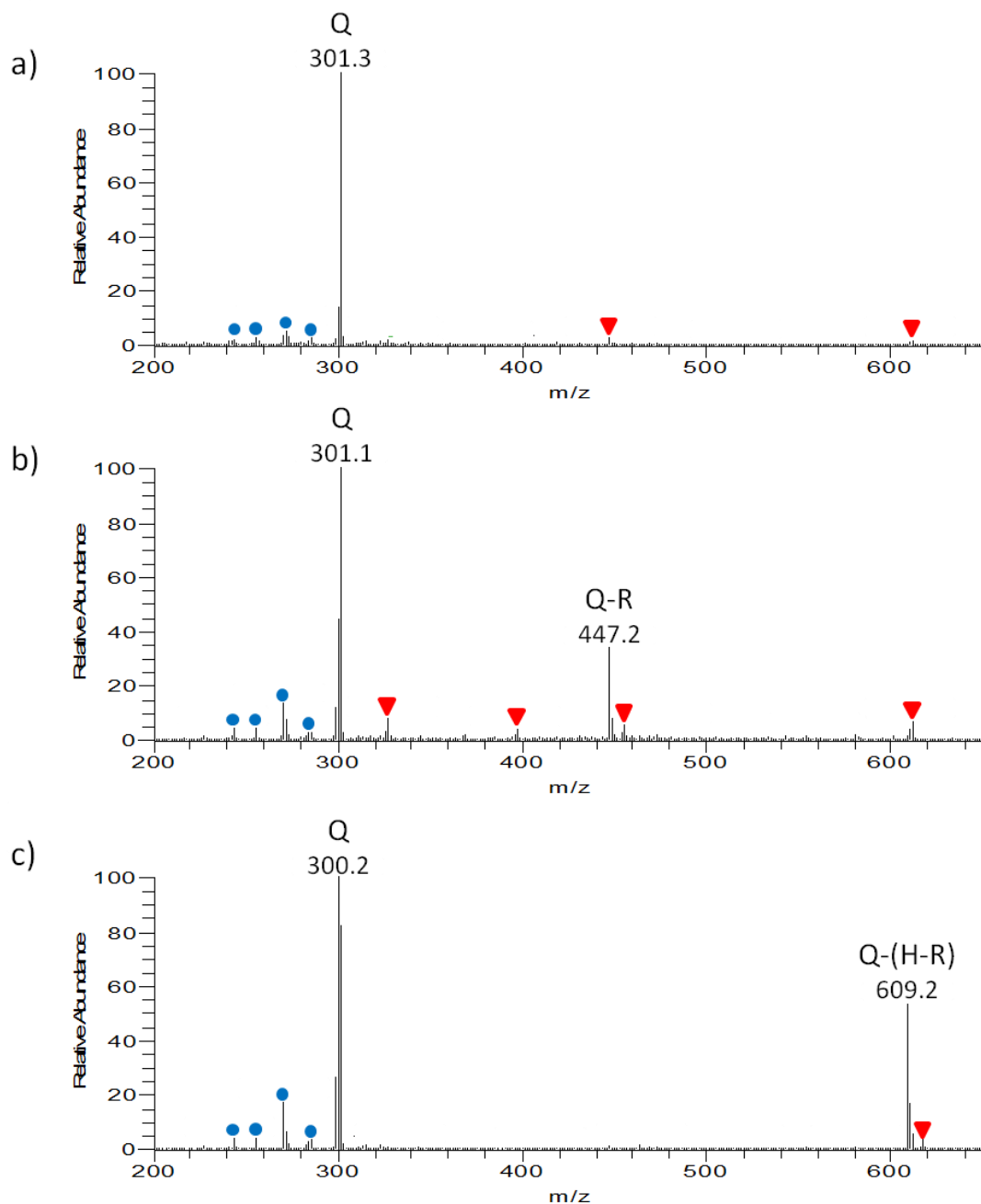
Figure S3. LDI-mass spectra of flavonoid standards with graphite matrix. quercetin (a), quercetin rhamnoside (b), and rutin (quercetin-3-(glucoside-rhamnoside)) (c). Significant fragmentation to the aglycone is observed for the mono- and di-glycosides. Quercetin fragments (●) and contaminations (▼) are marked.
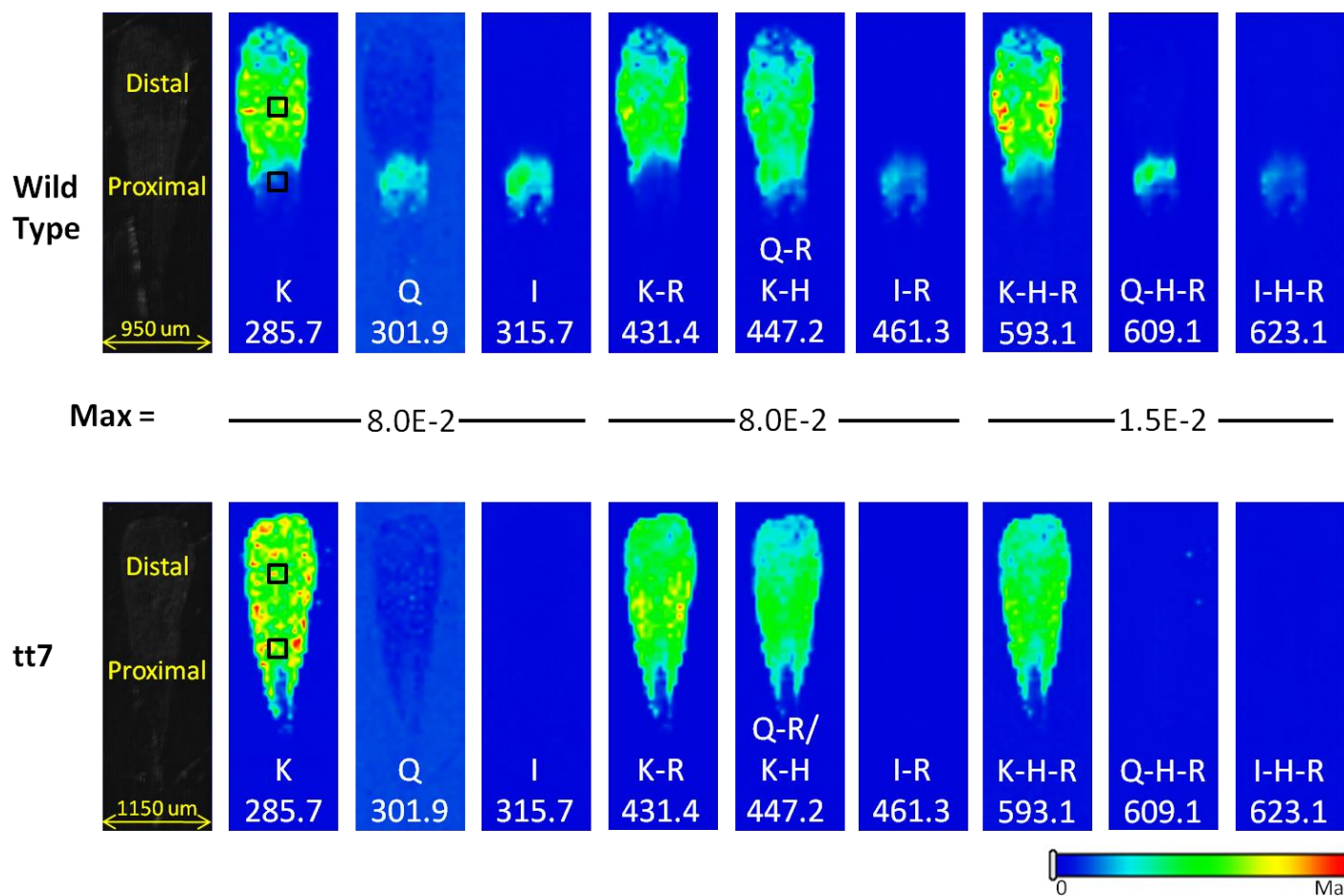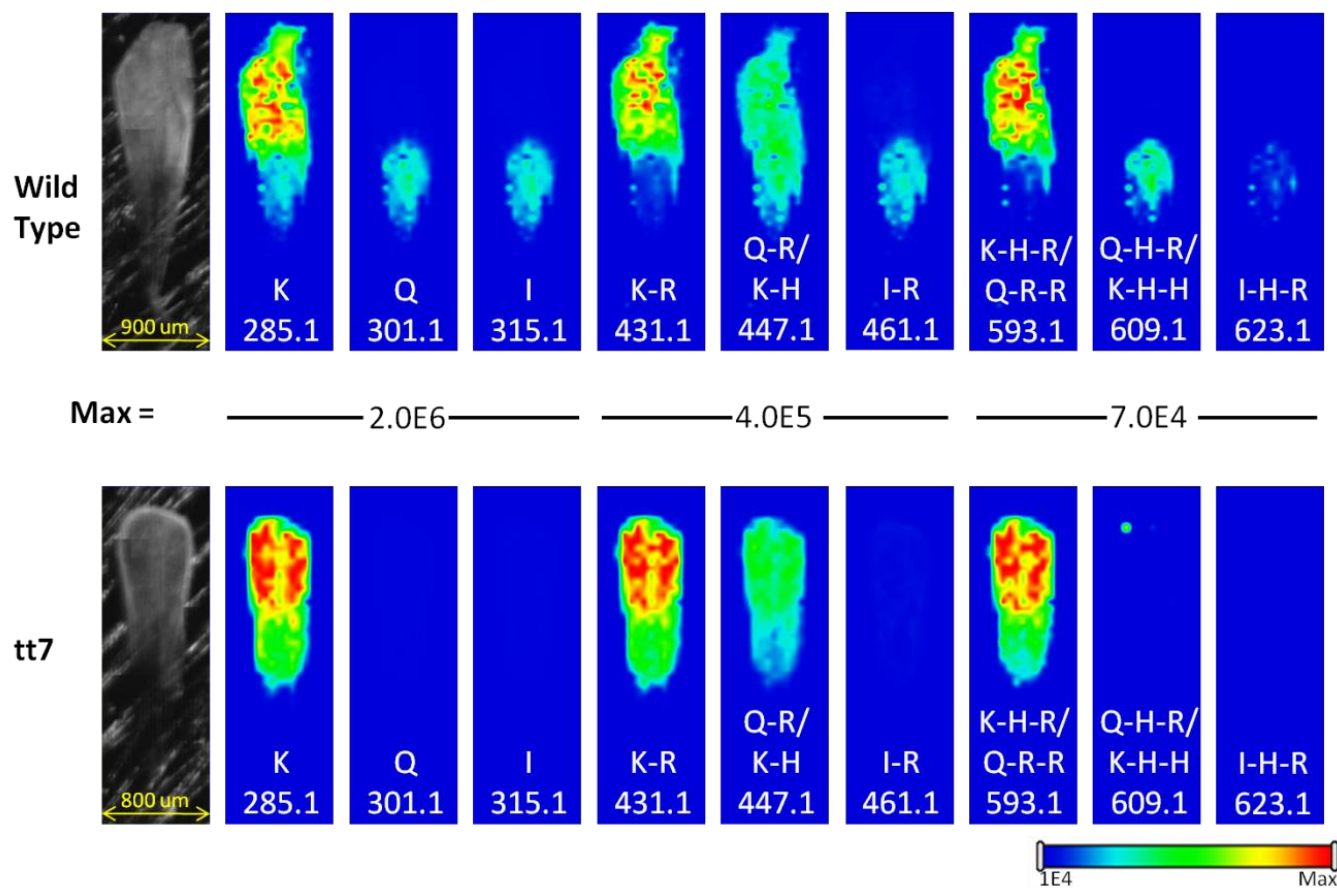
Figure S4. Flavonoid image on petals without matrix. Optical and MS images of wild-type (top series) and tt7 mutant (bottom series) *Arabidopsis thaliana* petals obtained without matrix showing distributions of kaempferol (K), quercetin (Q) and isorhamnetin (I), along with their rhamnose (R) and hexose (H) glycosides. All plotted *m/z* represent the deprotonated pseudo-molecules, [M-H]⁻. The irregular shape at the top corners of the wild-type images is a result of folding of the petal during sample drying. Apparent differences in intensities between the distal and proximal regions in the *tt7* petal are an artifact of lower overall ion yields from the proximal region and can be largely corrected by normalization to the total ion current (TIC). However, without matrix background, normalization with TIC introduces another artifact because of no signal outside the tissue, so they are presented without normalization.
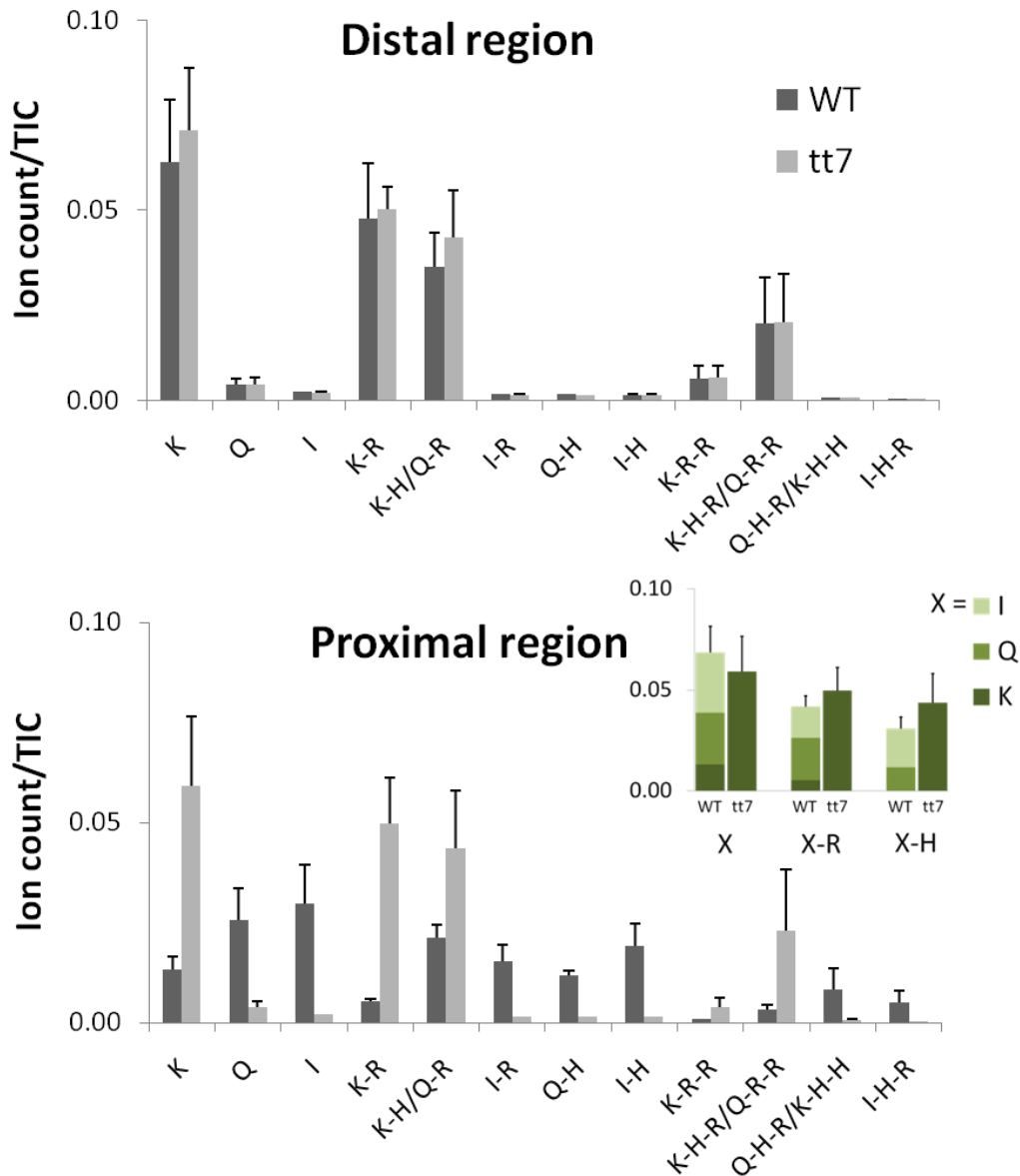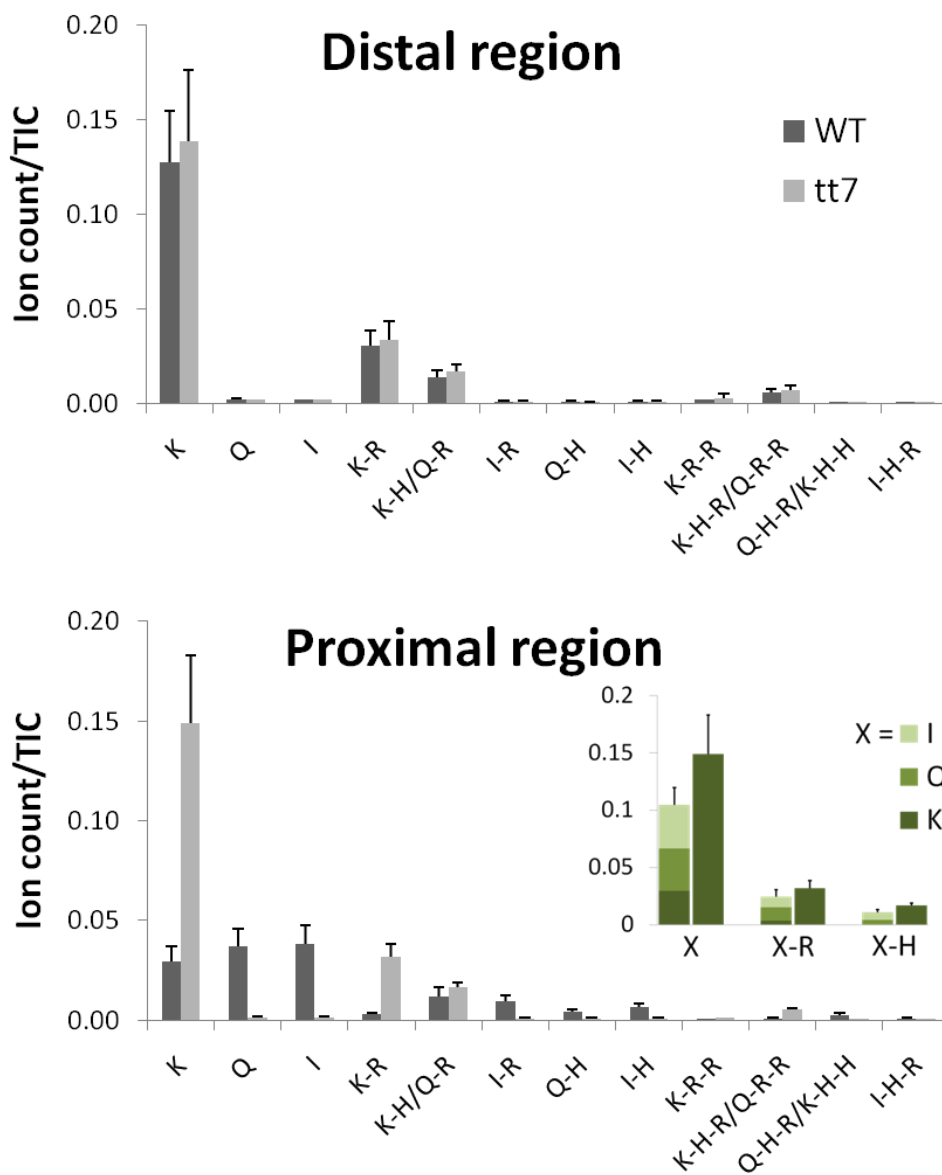
Figure S5. Semi-quantification of flavonoids in distal and proximal region of petals without matrix. Relative ion signals of flavonoids in two regions of wild-type (WT) and *tt7* mutant *Arabidopsis* petals. The values are obtained from 25 pixels in each region of MS images in four replicates. Error bars represent one standard deviation. All signals are normalized to TIC. Data was collected without the use of a matrix. Inset shows a comparison of summed kaempferol, quercetin, and isorhamnetin aglycone and glycoside signals from WT petals to kaempferol aglycone and glycoside signals from *tt7* petals. In the calculation of inset data, *m/z* 447 (kaempferol hexoside/quercetin rhamnoside) was assumed to be entirely due to quercetin rhamnoside in WT and entirely due to kaempferol hexoside in tt7.

CHAPTER 3

## MALDI-MS ANALYSIS AND IMAGING OF SMALL MOLECULE METABOLITES WITH 1,5-DIAMINONAPHTHALENE (DAN)

Andrew R. Korte and Young Jin Lee

Abstract

1,5-diaminonaphthalene (DAN) has previously been reported as an effective matrix for matrix-assisted laser desorption ionization-mass spectrometry of phospholipids. In the current work, we investigate the use of DAN as a matrix for small metabolite analysis in negative ion mode.   DAN was found to provide superior ionization to the compared matrices for MW < ~400 Da; however, 9-aminoacridine (9-AA) was found to be superior for a uridine diphosphate standard (MW 566 Da). DAN was also found to provide a more representative profile of a natural phospholipid mixture than 9-AA. Finally, DAN and 9-AA were applied for imaging of metabolites directly from corn leaf sections.

Introduction

The choice of matrix is critically important in matrix-assisted laser desorption ionization-mass spectrometry (MALDI-MS). Recent interest in metabolomic applications of MALDI-MS has resulted in the development of novel matrices and nanostructured substrate surfaces for the

analysis of small molecules (MW < ~1,000 Da). Substrate surfaces based on nanoporous

silicon[58] and nanopost arrays[59] have shown superior sensitivity for small molecule analyses;

however, their imaging application is limited to very thin tissue samples (<10 μm). Titanium

dioxide nanoparticles[60] and graphene oxide[61] are emerging new matrices and have been

successfully demonstrated for small molecule analysis. With regard to organic matrices, 9-

aminoacridine (9-AA)[62], 1,8-bis(dimethylamino)naphthalene (DMAN)[63], and N-(1-naphthyl)

ethylenediamine dinitrate[64] have been reported to be useful for small molecule analysis,

particularly for negative ion mode. Among these, the strong basicity of DMAN is suggested to

be useful for MALDI-MS analysis of weakly acidic biomolecules; however, the vacuum instability

of DMAN has become known to be a serious limitation, particularly for imaging applications.[65]

Another basic matrix, 1,5-diaminonaphthalene (DAN), is known for in-source decay top-

down sequencing of proteins and peptides in positive ion mode because of its hydrogen radical

transfer capability.[66, 67] It has also been used for in-source fragmentation of oligonucleotides

in negative ion mode.[68] Recently, Thomas and coworkers reported that DAN provides superior

ion signals for a wide range of lipids, in both positive and negative modes.[65] However, there

has been no report yet on the use of DAN for low-molecular weight (LMW) analytes (MW < 600

Da). The development of additional matrices for this mass range is highly desirable for the

study of plant metabolic biology, especially for negative ions. Many metabolites within this

mass range readily yield negative ions (e.g. primary metabolite small organic acids, phosphate

sugars, and nucleoside phosphates, among others). In the current study, we investigate the use

of DAN for small molecule analysis in negative ion mode and compare its performance to other

matrices.

A few LMW compounds representing several plant metabolite classes were used as test analytes in the current study: malic acid (MW 134), glutamic acid (MW 147), phosphoenolpyruvic acid (MW 168), ascorbic acid (MW 176), and uridine diphosphate glucose (MW 566). In addition to DAN, 9-AA, α-cyanohydroxycinnamic acid (CHCA), and 2,5-dihydroxybenzoic acid (DHB) were compared in the same experimental conditions. DAN and 9-AA were also compared for the negative mode analysis of an extract of soy phospholipids to evaluate their effectiveness in the analysis of medium molecular weight (MMW) compounds (MW between 600 and ~1,000 Da). Finally, DAN and 9-AA were applied for the chemical imaging of metabolites from corn leaf cross-sections.

Experimental

Chemicals

1,5-diaminonaphthalene (DAN, 97%), 2,5-dihyroxybenzoic acid (DHB, 98%), α-cyano-4-hydroycinnamic acid (CHCA, 99%), chloroform (CHROMASOLV® HPLC), malic acid (99+%), phosphoenolpyruvic acid monosodium salt hydrate (97+%), L-glutamic acid (99.5+%), ascorbic acid (98+%), and uridine 5'-diphosphoglucose (UDP-glucose; 98+%) were purchased from Sigma-Aldrich (St. Louis, MO, USA). Soy phospholipid extract (Soy PC 20%) was purchased from Avanti Polar Lipids (Alabaster, AL, USA). Methanol (Optima® LC-MS) was purchased from Thermo Fisher Scientific (Waltham, MA, USA). 9-aminoacridine hydrochloride (9-AA, 98%) was purchased from Sigma-Aldrich and the basic form was prepared by dissolving the hydrochloride salt in boiling water and adding excess sodium hydroxide to precipitate the free base. The

product was isolated by filtration and rinsed several times with cold water, then dried under

vacuum.

Analysis of standards

Solutions of matrices (DAN, 9-AA, CHCA, and DHB) were prepared at 10 mM in

methanol. For water-soluble standards, a solution containing malic acid, glutamic acid,

phosphoenolpyruvic acid, and ascorbic acid at 10 mM each and UDP-glucose at 2.5 mM was

prepared in water. For phospholipid standards, soy phospholipid extract was dissolved at 2

mg/mL in chloroform. Each matrix solution was mixed 9:1 (v:v) with the analyte solution. The

matrix-analyte mixture was then applied to a stainless steel MALDI target by spraying with a

custom-made oscillating capillary nebulizer (OCN)[20]. Compared to the dried-droplet method,

this produced a very homogeneous sample coating, eliminating the 'hot spot' issue of dried-

droplet preparation. 200 μL of each matrix-analyte mixture was sprayed at a rate of 50 μL/min

from a height of 9 mm with a nebulizing gas pressure of 40 psi. The spray device and slide were

kept static during the spraying process, and this resulted in a coated area approximately 1.5 cm

in diameter.

MALDI-MS analysis was performed on a linear ion trap-orbitrap hybrid mass

spectrometer (MALDI LTQ-Orbitrap Discovery; Thermo Scientific, San Jose, CA). The instrument

has been modified to use an external Nd:YAG laser (UVFQ; Elforlight, Ltd., Daventry, UK)

operating at a repetition rate of 60 Hz. Spectra were collected using the orbitrap analyzer with

a scan range of m/z 50 to 600 for LMW standards and m/z 500 to 1200 for phospholipid extract.

Each spectrum was collected using 10 laser shots, and one spectrum was collected from each

raster point. Data were acquired for a set of standard samples in triplicate in randomized sample order.

Laser energy was individually optimized for each matrix by rastering over an area of the sprayed sample and increasing the energy stepwise over the course of the scan. For each matrix, the laser pump diode energy was increased from 79% to 90% in increments of 0.5% and each energy setting was maintained for 1 minute. Based on measurements of the laser output energy, this range corresponds to approximately 0.2-18 µJ per pulse. Considering the estimated laser spot diameter of 50 µm, this yields laser fluences ranging from ~12 to ~900 mJ/cm^2. It is important to note that pulse energies were measured at the laser aperture, and some energy loss is inevitable at each of the beam steering and focusing elements. Therefore, the actual fluences at the sample surface are expected to be slightly lower.

After acquisition, time traces for the $[M-H]^-$ species of each analyte were extracted and exported to Microsoft Excel. Signal levels for each analyte were averaged at each laser energy step and the signal level was plotted as a function of laser energy. These plots, shown in Supplemental Figure S1, were used to select the optimal laser energy for each matrix as described in Results and Discussion. The averaged spectrum at the optimal laser energy for each matrix was used for comparison of matrices.

Maize leaf cross-sectional imaging

B73 inbred maize (*Zea mays*) seedlings were cultivated in soil in a greenhouse and harvested 14 days after germination. A transverse section of the 3rd leaf approximately 15 cm from the stalk was cut, placed into a 10% w/v gelatin solution in a mold and floated on liquid

nitrogen until the gelatin was nearly frozen solid. The embedded tissue was then transferred to a cryostat (Leica CM1850, Leica Microsystems, Buffalo Grove, IL, USA) at -20 °C and allowed to equilibrate at that temperature. 10 μm transverse tissue sections were collected using Cryo-Jane® adhesive tape (Leica Microsystems) to preserve tissue morphology. Tissue sections were left affixed to the tape windows, instead of thaw-mounting directly to glass or metal slides, to avoid any delocalization of soluble metabolites. Each tape window, with the tissue still affixed, was then attached to a glass slides for easier transport and storage, transported on dry ice, and stored at -80 °C. Prior to analysis, an aluminum block (approx. 18 cm x 6 cm x 0.65 cm) was precooled to -80 °C. Slides holding tape and tissue sections were laid on this block and placed into a vacuum chamber, then dried at a pressure of ~50 mtorr for 90 minutes. Use of adhesive tape in cryosectioning, maintaining sample sections at -80 °C and gradual drying/warming under vacuum provides tissue samples that are intact and completely dried for analysis and minimizes delocalization of water-soluble metabolites as a result of atmospheric condensation or sample thawing.

DAN and 9-AA were applied by sublimation using a procedure similar to that described by Hankin *et al*.[69] By inserting a beam expander into the laser path[70], the spot size at the sample surface was reduced to 20 μm, as estimated from ablation spots on the matrix-coated embedding material outside the analyzed tissue region. TunePlus and Xcalibur software (Thermo Scientific) were used to define the experimental parameters. Imaging data were acquired with a raster step size of 25 μm, 20 shots per scan, and a scan window of *m/z* 100-1000. For imaging experiments, slightly higher laser energy was used due to energy loss at the beam expander. Laser energies were set at 83.5% and 85.0% for DAN and 9-AA, respectively.

ImageQuest (Thermo Scientific) was used to generate MS images with a *m/z* window of ± 0.005. Tentative assignments were made based on accurate mass values.

Results and Discussion

To avoid the 'hot spot' problem commonly seen with MALDI sample spotting, standard analysis was performed by spraying a mixture of standards and matrix using an oscillating capillary nebulizer device. A portion of the sprayed area was then scanned while the laser pulse energy was periodically increased to find the optimal laser energy for each matrix. As expected, metabolite standard signal levels were found to be heavily dependent upon laser fluence. Supplemental Figure S1 shows the intensity of each of the standard compounds and the predominant matrix ion ($[M-H]^-$ for each case) with varying laser energy. In the case of DAN, all ion signals increase to a peak intensity in the 81-83% energy range (90-270 mJ/cm^2 fluence range), then decline at higher energies. With 9-AA, CHCA, and DHB, signals for malic, glutamic, and ascorbic acids increase across the range of laser fluences investigated. UDP-glucose and phosphoenolpyruvic acid, however, which contain labile bonds, exhibit a similar behavior regardless of matrix: both signals peak at lower laser fluences, and decline significantly beyond that, as the excess energy leads to in-source decay of the $[M-H]^-$ species. Additionally, excess laser energy gives rise to increased matrix background signals. Therefore, as a compromise among these three factors (signal intensity for non-labile compounds, signal intensity for labile compounds, and reduction of matrix signals), the peak of the UDP-glucose signal was used to determine the 'optimal' laser fluence for each matrix, and this fluence was used to compare

signal levels between matrices. These optimal values correspond to calculated fluences of ~90 mJ/cm^2 for DAN and CHCA, ~130 mJ/cm^2 for 9-AA, and ~270 mJ/cm^2 for DHB.

A comparison of spectra obtained from each matrix-metabolite standard mixture at the optimal laser energy is presented in Figure 1. Significant suppression of the matrix background signals is seen for both DAN and 9-AA, relative to the matrix blank spectra (Supplemental Figures S2a, S2b). All analytes are detected as the [M−H]$^-$ species at some level with all four matrices (malic acid, *m/z* 133.014; glutamic acid, *m/z* 146.046; phosphoenolpyruvic acid, *m/z* 166.975; ascorbic acid, *m/z* 175.025; UDP-glucose, *m/z* 565.047), though with significant differences in signal intensity. Additional peaks detected at >5% relative abundance and identified based on accurate mass measurements are listed in Supplemental Table 1. DAN and 9-AA both show appreciable signal for the [M−H$_2$O−H]$^-$ fragments of malic acid and phosphoenolpyruvic acid. DAN also shows signal for adducts of DAN and ascorbic acid (*m/z* 315.098, [DAN + ascorbic acid – H$_2$O – H]$^-$ and *m/z* 331.093, [DAN + ascorbic acid – 3H]$^-$). The 9-AA spectrum contains several UDP-glucose fragments and phosphate-like signals that are suspected to arise from UDP-glucose, in line with previous observations that MALDI-MS using 9-AA as matrix leads to significant fragmentation of phosphorylated nucleotides.[71] The CHCA spectrum is dominated by matrix-derived signals. The DHB spectrum contains matrix-derived peaks and a peak corresponding to a malic acid-DHB-borate cluster, similar to the borate complexes observed by Penn *et al*.[72]

For quantitative comparison of MALDI efficiency, [M−H]$^-$ ion signals of each analyte in Figure 1 are compared based on their absolute values, as shown in Figure 2. Each signal is normalized to the highest value among the four matrices, and represents the average of three

non-consecutive acquisitions. DAN was found to provide significantly higher signal levels for malic, glutamic, phosphoenolpyruvic, and ascorbic acids (11x, 30x, 3x, and 4x higher than the next highest signal for the other tested matrices, respectively). However, 9-AA shows 2.5 times higher intensity for UDP-glucose than DAN, suggesting significant selectivity for different metabolite classes.

A comparison of spectra obtained from soy phospholipid extract using DAN and 9-AA is shown in Figure 3. A laser optimization procedure similar to that used for small metabolites was performed for the phospholipid mixture. Phospholipid signals were found to plateau at intermediate laser energies (82.5% for DAN, 83.5% for 9-AA), with little difference in spectral profile with increasing energy from these values (data not shown). Therefore, the beginning of this signal plateau was chosen for comparison. The manufacturer-provided phospholipid content of the mixture is as follows: 24.0% phosphatidylcholine (PC), 18.6% phosphatidylethanolamine (PE), 11.5% phosphatidylinositol (PI), 4.3% phosphatidic acid (PA), 4.6% Lyso-PC, 37.0 unknown. Due to the quaternary amine functional group, PC is not detected in negative mode. DAN and 9-AA provide similar signal levels for PI species. DAN, however, provides significantly higher signal for PE and N-acylphosphatidylethanolamines (NAPE). The spectra obtained using DAN as matrix provide a phospholipid profile closer to the specified composition, while 9-AA seems to preferentially ionize PI species while suppressing signal for other phospholipids. For example, the ratio of summed ion count for PE: PI: PA is 100: 82: 8.6 for DAN and 100: 803: 33 for 9-AA, whereas that provided by the manufacturer is 100: 37: 40. Phospholipids identified from the soy PL mixture are listed in Supplemental Table S2.

Encouraged by the promising results of small molecule analysis by DAN and 9-AA, we applied both for the chemical imaging of cross-sections of maize seedling leaves. Figure 4 shows the chemical images of various small molecules from these leaf sections using DAN and 9-AA on adjacent sections. Based on accurate mass measurements, these signals were assigned to a wide range of metabolite classes, including amino acids such as asparagine and glutamic acid (4a, 4c), small organic acids such as malic and ascorbic acids (4b, 4d), flavonoid and flavonoid glycosides such as kaempferol and maysin (4e, 4g), benzoxazinoid defense compounds such as 2-Hydroxy-7-methoxy-(2H)-1,4-benzoxazin-3(4H)-one[73] (HMBOA-glucose, 4f), and sulfolipids such as sulfoquinovosyl diacylglycerol (34:3) (4h).

A number of distinct distributions are observed for different metabolites, and several of these distributions correlate to tissue structural features. Asparagine (4a) is seen in localized clusters near the midrib section of the leaf. Malic acid (4b) and glutamic acid (4c) are detected more or less evenly throughout the interior leaf tissues. Ascorbic acid (4d) is detected both in interior and epidermal tissues, consistent with its multitude of metabolic roles in a wide range of cell types.[74] Flavonoids and flavonoid glycosides (4e, g) are observed within the epidermal cell layers on the leaf exterior, in agreement with previous reports and their role in UV protection and plant defense.[75, 76] Interestingly, the flavonoid C-glycoside maysin (4g) is readily detected in the upper epidermis and largely absent in the lower epidermis. HMBOA-glucose (4f) is detected in clusters in the mesophyll between the peripheral vascular bundles, rather than within the vascular bundles themselves. SQDG (34:3) (4h) is detected in a series of rings along the length of the leaf, closely following the pattern of photosynthetic cells surrounding the vascular bundles. The vascular bundles are clearly visible as the ring centers,

where no SQDG is detected. This distribution agrees with the known presence of SQDG in the membranes of photosynthetically-active cells.[77] For the reader's reference, an optical microscope image showing a portion of a maize leaf section and a schematic showing the structural features of the analyzed sections is provided in Supplemental Figure S3.

As expected from the standard analysis, metabolite signal from tissue using DAN is generally higher than 9-AA, especially at low mass below m/z ~ 400, whereas 9-AA is slightly better for some compounds in high mass range above m/z ~ 400. While many of the metabolite distributions (e.g. flavonoids and SQDG) can be explained from known functions or previously observed localizations, the biological implications of some (e.g. HMBOA-glucose) are not readily apparent and will require further investigation; nonetheless, these results demonstrate the ability of both matrices to ionize metabolites with a wide range of functionalities from tissue.

Conclusions

We have successfully demonstrated the application of DAN as a MALDI matrix for small molecule metabolites in both profiling and imaging. DAN was compared to three common MALDI matrices: 9-AA, CHCA, and DHB. For the investigated compounds, DAN compares favorably or significantly exceeds the performance of the other tested matrices. Specifically, DAN shows superior ion signals for MW < ~400 Da in both selected standards and some plant metabolites on cross-sectional leaf tissue. For MMW molecules (600- ~1,000 Da), 9-AA shows better performance in some compounds; however, DAN was found to provide a more

representative characterization of phospholipid content for a plant-derived extract. We suggest that DAN, while previously used for imaging and analysis of lipids, is also useful for small metabolite analysis in negative mode, and that its utility for both low-mass analytes and larger lipids makes it appealing as a 'universal' matrix for metabolite imaging in the negative mode.

Acknowledgment
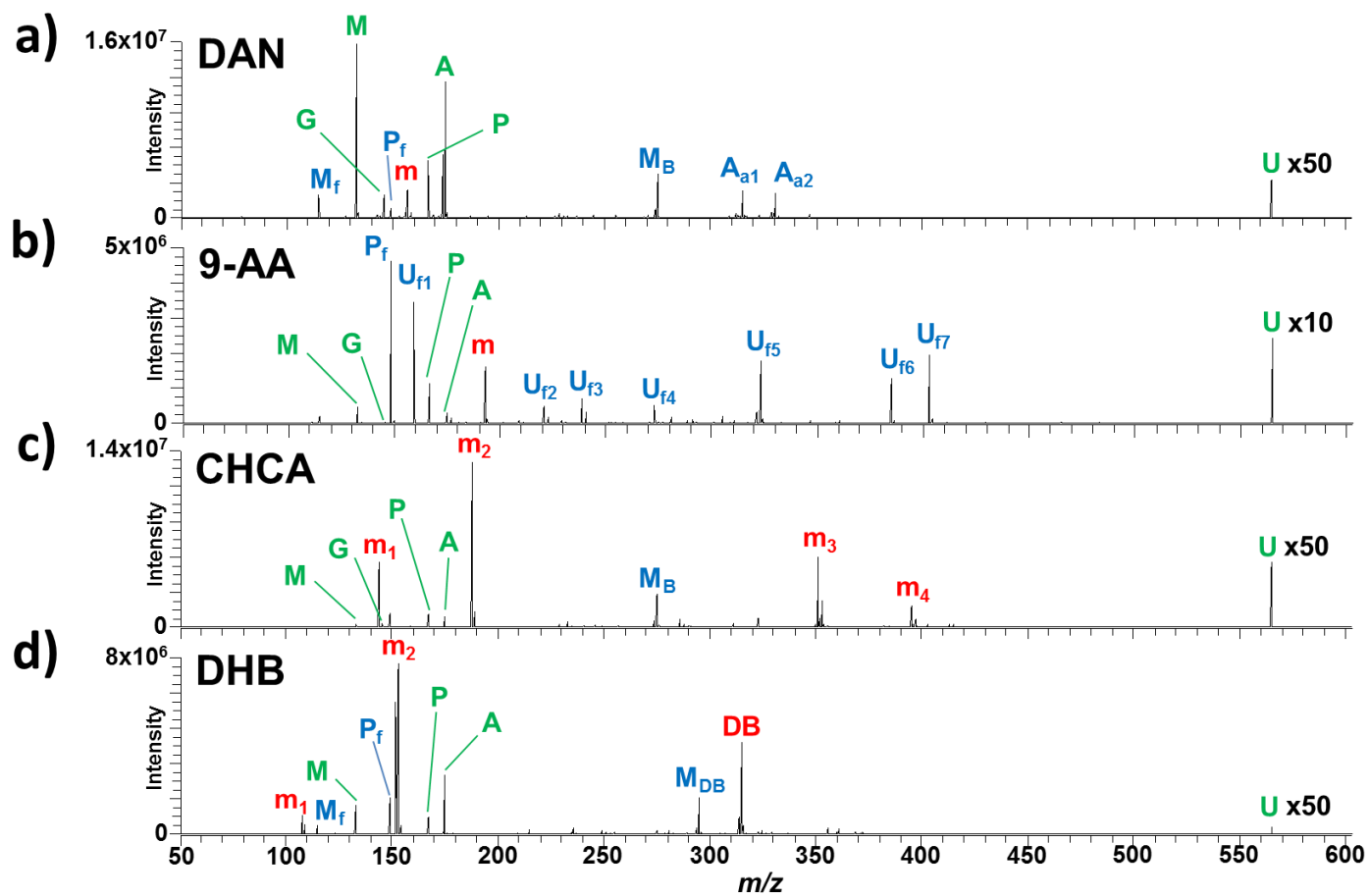
Figure 1. MALDI-MS spectra of a metabolite standard mixture using several different matrices (*a*, DAN; *b*, 9-AA; *c*, CHCA; *d*, DHB). Spectra represent approximately 64 averaged scans at the optimal laser energy for UDP-glucose signal. Label of peaks are: M, malic acid (*m/z* 133.014); G, glutamic acid (*m/z* 146.046); P, phosphoenolpyruvic acid (*m/z* 166.975); A, ascorbic acid (*m/z* 175.025); U, UDP-glucose (*m/z* 565.047); M_f, P_f and U_{fi}, fragments of M, P and U, respectively; A_{ai}, adducts of A and matrix; m or m_i, matrix peaks; M_B. a malic acid-borate complex; M_{DB}, a malic acid-DHB-borate complex; DB, a DHB-borate complex. A list of peak assignments is provided in Supplementary Table S1.
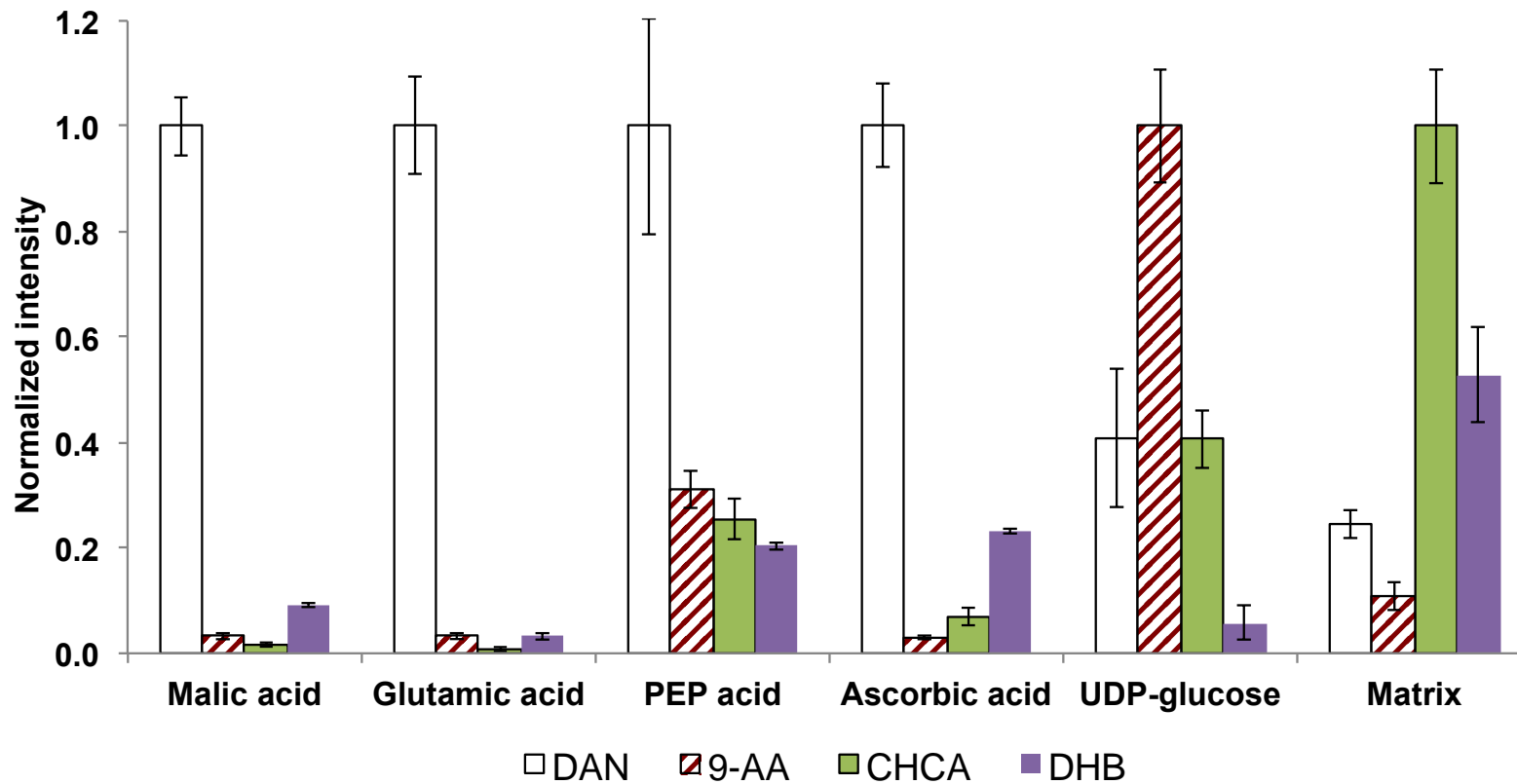
Figure 2. Comparison of metabolite ion signals and predominant matrix signal ([M−H]⁻) for each matrix at optimal laser energy. Values represent the average of three replicates and are shown normalized to the highest intensity for each metabolite. Error bars represent one standard deviation.
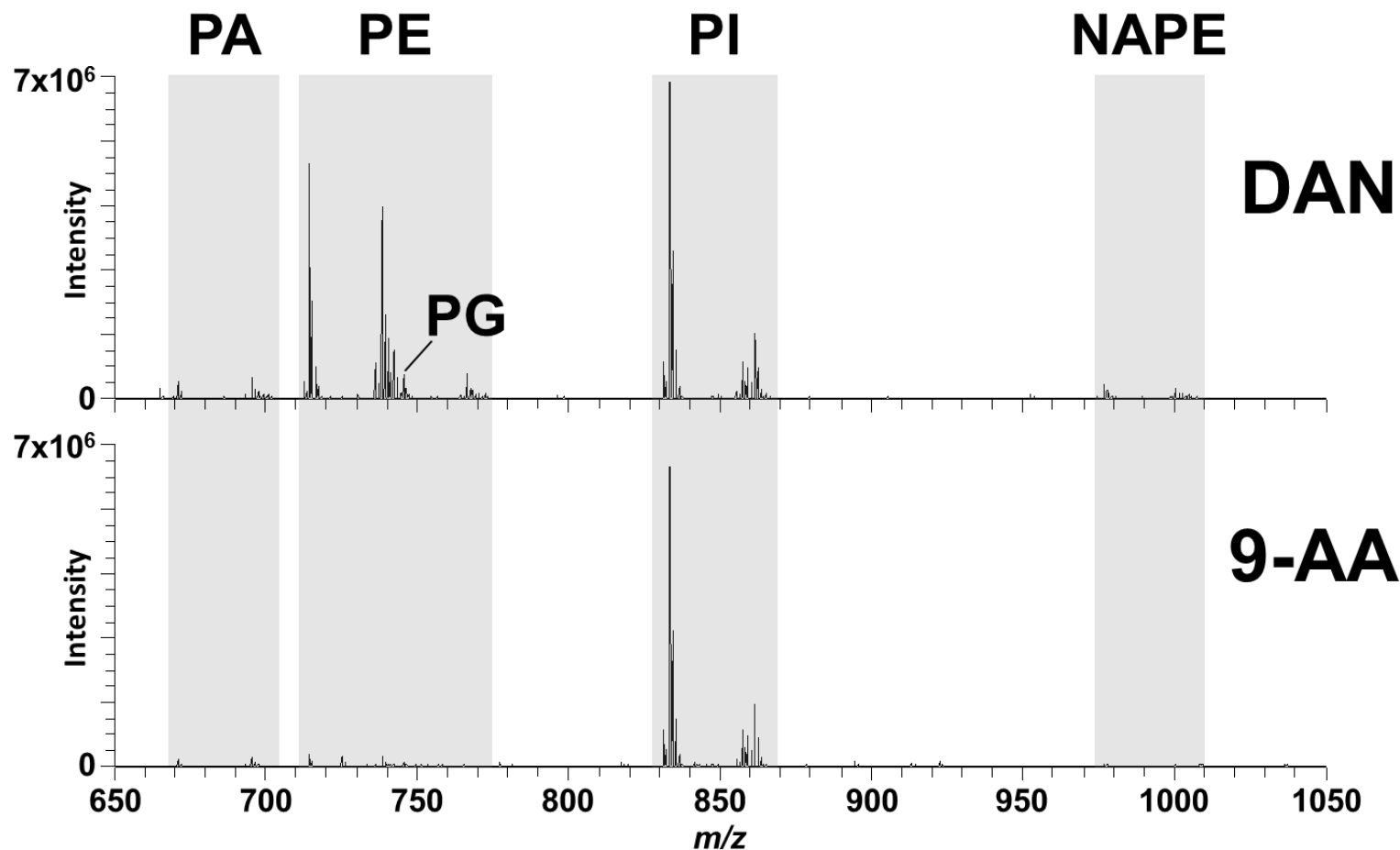
Figure 3. Spectra obtained from soy phospholipid extract using DAN (*top*) and 9-AA (*bottom*) as matrix. Spectral regions that are dominated by a particular phospholipid class are highlighted and labeled with the class: PA, phosphatidic acid; PE, phosphatidylethanolamine; PG, phosphatidylglycerol; PI, phosphatidylinositol; NAPE, N-acylphosphatidylethanolamine. A list of peak assignments is presented in Supplementary Table S2.

DAN

9-AA
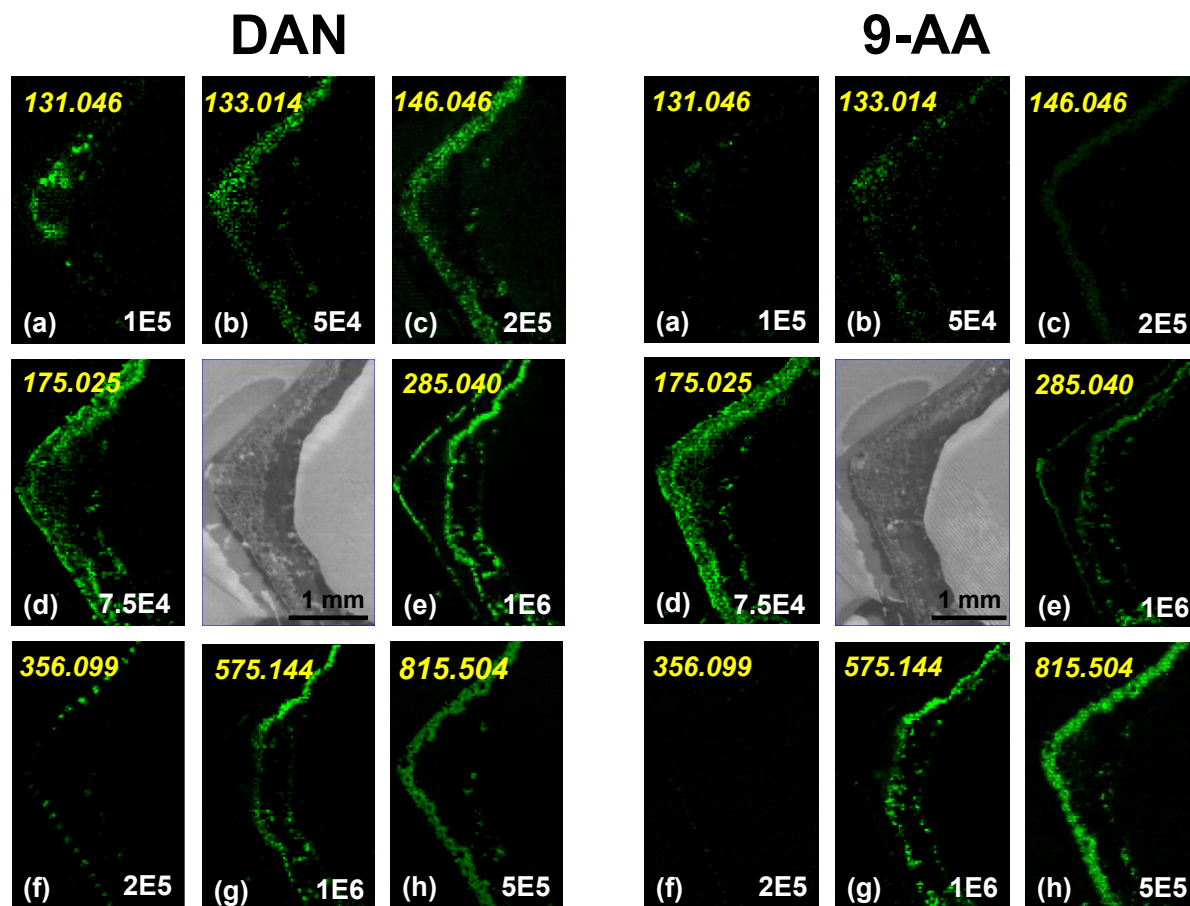
Figure 4. Chemical images of corn leaf cross-section with DAN and 9-AA as matrices. Images were generated using a mass window of ± 0.005 Da. Brighter color indicates higher intensity. Scales range from zero to a maximum intensity indicated by the value at the bottom right of each image. Tentative assignments made based on accurate mass values are as follows, all as $[M-H]^-$ ions: (**a**) m/z 131.046, asparagine; (**b**) m/z 133.014, malic acid; (**c**) m/z 146.046, glutamic acid; (**d**) m/z 175.025, ascorbic acid; (**e**) m/z 285.040, $C_{15}H_{10}O_6$ flavonoid, e.g. kaempferol; (**f**) m/z 356.099, HMBOA-glucose; (**g**) m/z 575.144, $C_{27}H_{28}O_{14}$ flavonoid glycoside, e.g. maysin; (**h**) m/z 815.504, SQDG (34:3).

Supplemental Tables and Figures

Table S1. Assignment of major peaks in Figure 1. Assignment of m/z 315.031 has been reported by **Penn *et al.*** (*Anal. Chem.* 1997**, 69**, 2471) and was also confirmed by MS/MS.

	m/z	Label	Formula	Assignment	Error (ppm)
Analytes	133.014	M	$C_4H_5O_5$	Malic acid	+1.2
	115.004	M_f	$C_4H_3O_4$	M - H_2O	+1.1
	275.021	M_B	$C_8H_8O_{10}B$	2M - 4H + B	-1.2
	146.046	G	$C_5H_8NO_4$	Glutamic acid	+0.3
	166.975	P	$C_3H_4O_6P$	Phosphenolpyruvic acid	-0.0
	148.965	P_f	$C_3H_2O_5P$	P - H_2O	-1.1
	175.025	A	$C_6H_7O_6$	Ascorbic acid	-0.8
	565.047	U	$C_{15}H_{23}O_{17}N_2P_2$	UDP-glucose	-2.9
	158.925	U_{f1}	HP_2O_6		+0.5
	220.847	U_{f2}	CuP_2O_6		-2.5
	238.891	U_{f3}	$H_2P_3O_9$	Trimetaphosphate	-2.9
	272.956	U_{f4}	$C_5H_7O_9P_2$	UDP-glu fragment 1	-3.5
	323.028	U_{f5}	$C_9H_{12}O_9N_2P$	UDP-glu fragment 2	-2.8
	384.983	U_{f6}	$C_9H_{11}O_{11}N_2P_2$	UDP-glu fragment 3	-3.2
	402.994	U_{f7}	$C_9H_{13}O_{12}N_2P_2$	UDP-glu fragment 4	-2.9
DAN	157.077	m	$C_{10}H_9N_2$	DAN	+0.4
	315.098	A_{a1}	$C_{16}H_{15}O_5N_2$	DAN + A - H_2O	-1.2
	331.093	A_{a2}	$C_{16}H_{15}O_6N_2$	DAN + A - 2H	-1.5
9-AA	193.077	m	$C_{13}H_9N_2$	9-AA	-1.3
CHCA	144.046	m_1	C_9H_6ON	CHCA - CO_2	+0.6
	188.035	m_2	$C_{10}H_6O_3N$	CHCA	-1.0
	351.020	m_3	$C_{18}H_{12}O_2N_2Cu$	2CHCA - 2CO_2 + Cu	-1.4
	395.009	m_4	$C_{19}H_{12}O_4N_2Cu$	2CHCA - CO_2 + Cu	-1.9
DHB	108.022	m_1	$C_6H_4O_2$	DHB - H_2O - CO	+1.8
	153.019	m_2	$C_7H_5O_4$	DHB	-0.1
	295.026	M_{DB}	$C_{11}H_8O_9B$	DHB - 4H + M + B	-3.2
	315.031	DB	$C_{14}H_8O_8B$	2DHB - 4H + B	-4.2

Table S2. Identified phospholipid peaks from standard soy phospholipid mixture.

m/z	ID	Formula	Error (ppm)	Supporting MS/MS ions	DAN	9-AA
					>1% Rel. Abund.	
671.466	PA (34:2)	$C_{37}H_{68}O_8P$	-0.0	255, 279	+	+
693.450	PA (36:5)	$C_{39}H_{66}O_8P$	+1.0	277, 279	+	−
695.465	PA (36:4)	$C_{39}H_{68}O_8P$	-0.6	279	+	+
697.482	PA (36:3)	$C_{39}H_{70}O_8P$	+0.3	279, 281	+	+
699.497	PA (36:2)	$C_{39}H_{72}O_8P$	+1.9	279, 281, 283	+	−
714.507	PE (34:2)	$C_{39}H_{73}O_8NP$	-1.1	255, 279	+	+
716.520	PE (34:1)	$C_{39}H_{75}O_8NP$	-4.5	255, 281	+	−
736.491	PE (36:5)	$C_{41}H_{71}O_8NP$	-2.0	277, 279	+	−
738.506	PE (36:4)	$C_{41}H_{73}O_8NP$	-2.3	279	+	+
740.521	PE (36:3)	$C_{41}H_{75}O_8NP$	-3.3	279, 281	+	+
742.537	PE (36:2)	$C_{41}H_{77}O_8NP$	-2.5	279, 281, 283	+	−
744.550	PE (36:1)	$C_{41}H_{79}O_8NP$	-6.8	281, 283	+	−
764.522	PE (38:5)	$C_{43}H_{75}O_8NP$	-2.8	277, 279	+	−
766.537	PE (38:4)	$C_{43}H_{77}O_8NP$	-3.1	279	+	−
768.553	PE (38:3)	$C_{43}H_{79}O_8NP$	-2.6	279, 281	+	−
770.568	PE (38:2)	$C_{43}H_{81}O_8NP$	-2.9	279, 311	+	−
730.502	O-PE (34:2)	$C_{39}H_{73}O_9NP$	-0.2	255, 271, 279, 295	+	−
745.500	PG (34:2)	$C_{40}H_{74}O_{10}P$	-2.9	255, 279	+	+
747.515	PG (34:1)	$C_{40}H_{76}O_{10}P$	-4.1	255, 281	+	−
769.500	PG (36:4)	$C_{42}H_{74}O_{10}P$	-3.9	279, 415	+	−
831.499	PI (34:3)	$C_{43}H_{76}O_{13}P$	-5.1	255, 277	+	+
833.514	PI (34:2)	$C_{43}H_{78}O_{13}P$	-5.4	255, 279	+	+
835.523	PI (34:1)	$C_{43}H_{80}O_{13}P$	-13.4	255, 281	+	+
855.498	PI (36:5)	$C_{45}H_{76}O_{13}P$	-6.2	277, 279	+	+
857.513	PI (36:4)	$C_{45}H_{78}O_{13}P$	-6.2	279	+	+
859.529	PI (36:3)	$C_{45}H_{80}O_{13}P$	-6.6	277, 279, 281, 283	+	+
861.544	PI (36:2)	$C_{45}H_{82}O_{13}P$	-7.5	279, 281, 283	+	+
863.553	PI (36:1)	$C_{45}H_{84}O_{13}P$	-15.5	281, 283	+	+
849.508	O-PI (34:2)	$C_{43}H_{79}O_{14}P$	-5.9	255, 271, 279, 295	+	−
817.510	SQDG (34:2)	$C_{43}H_{77}O_{12}S$	-5.2	537, 561	−	+
841.509	SQDG (36:4)	$C_{45}H_{77}O_{12}S$	-6.4	561	−	+
952.729	NAPE (50:2)	$C_{55}H_{103}O_9NP$	-9.4	279, 672, 690, 696, 714	+	−
976.728	NAPE (52:4)	$C_{57}H_{103}O_9NP$	-10.2	279, 696, 714, 720, 738	+	−
978.740	NAPE (52:3)	$C_{57}H_{105}O_9NP$	-13.1	279, 281, 698, 714, 716	+	−
1000.727	NAPE (54:6)	$C_{59}H_{103}O_9NP$	-9.8	279, 720, 738	+	−
1002.740	NAPE (54:5)	$C_{59}H_{105}O_9NP$	-11.7	279, 281, 722, 738, 740	+	−
1004.757	NAPE (54:4)	$C_{59}H_{107}O_9NP$	-10.9	279, 281, 724, 742	+	−
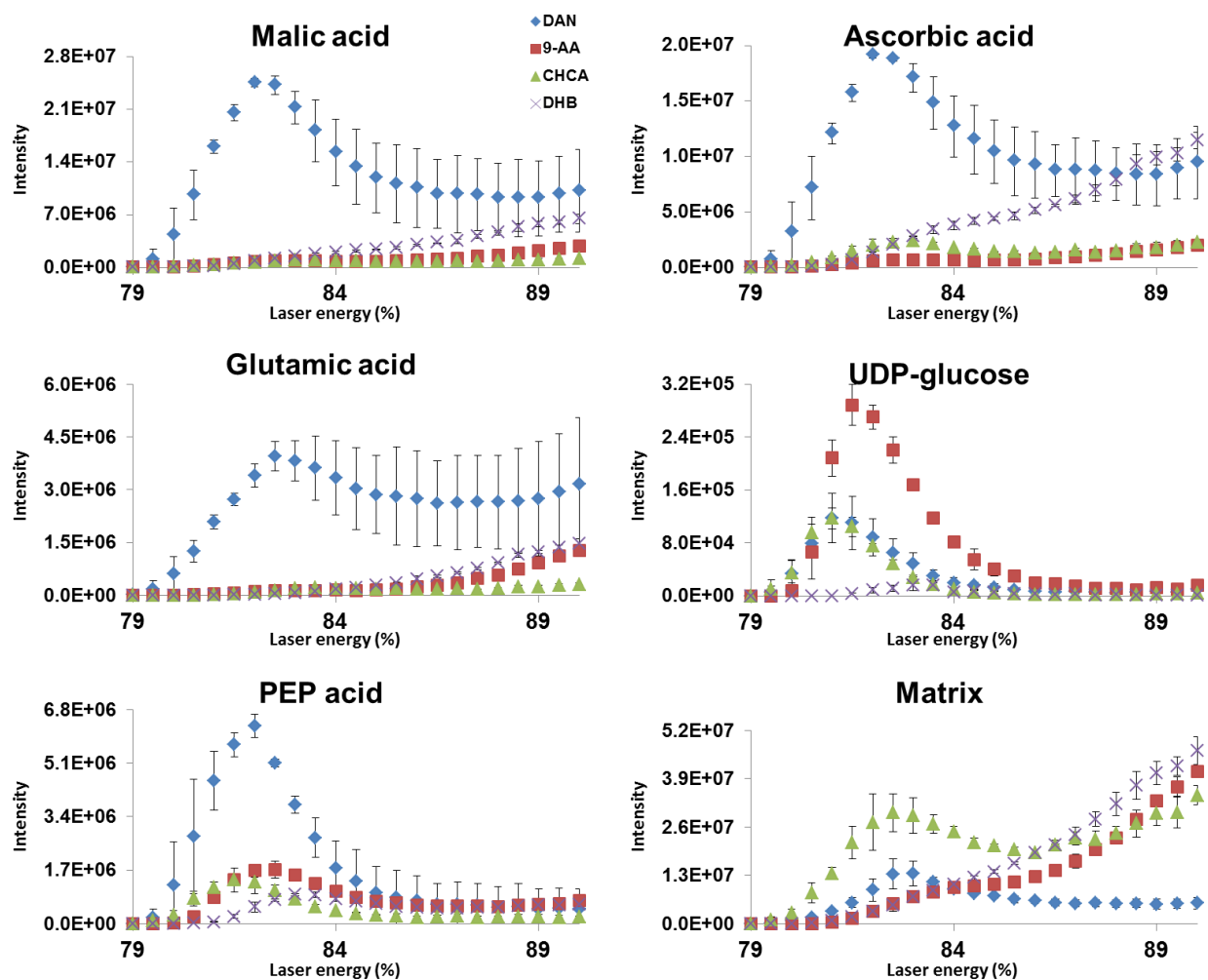
Figure S1. Intensity of [M−H]⁻ signal for several metabolites in a standard mixture, as a function of laser energy. Each data point represents the average of 3 nonconsecutive replicates, each consisting of ~64 averaged spectra at each energy. Error bars represent ± 1 standard deviation.
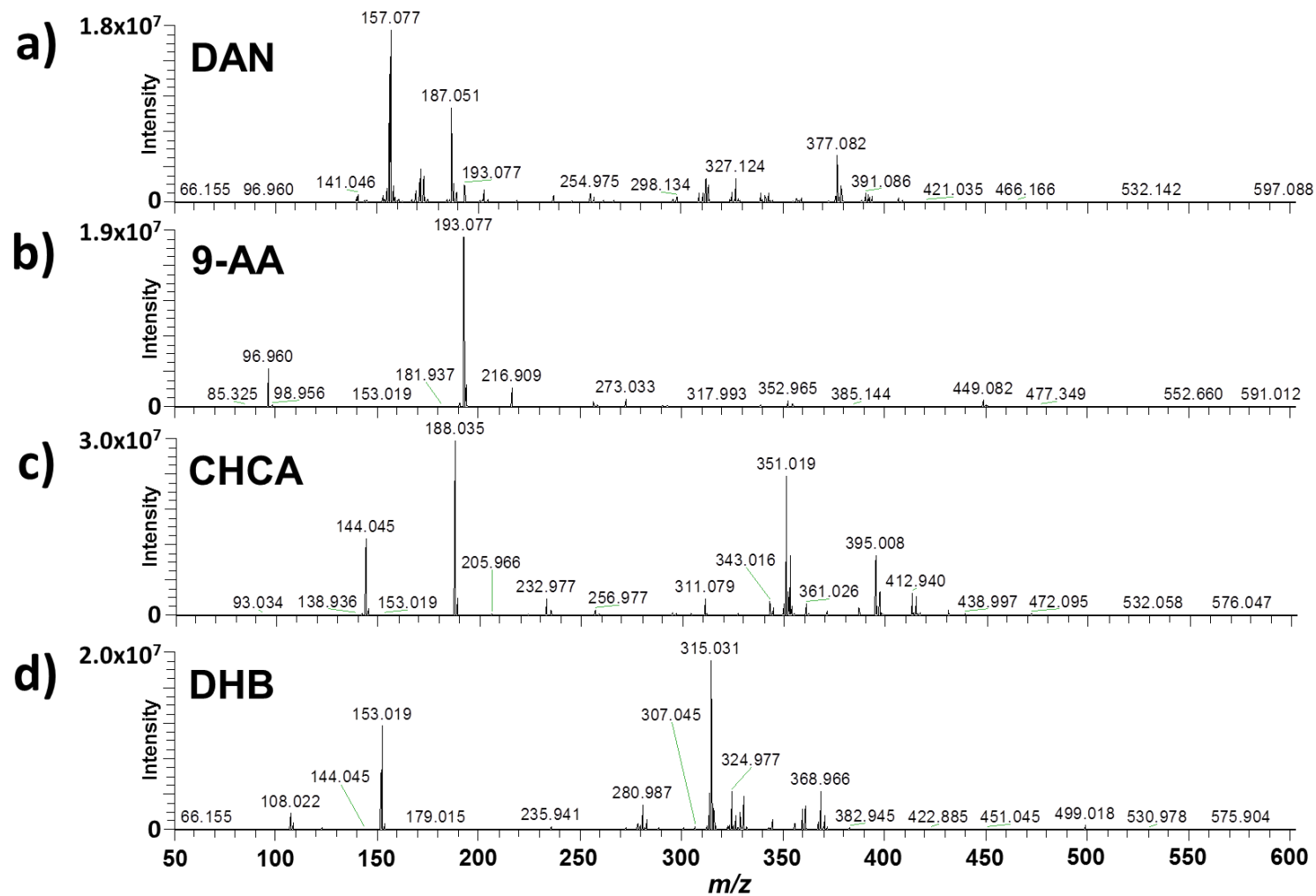
Figure S2. Blank MALDI-MS spectra of the four investigated matrices. Spectra represent approximately 64 averaged scans at the optimal laser energy for UDP-glucose signal. Intensity scales are different for each matrix.
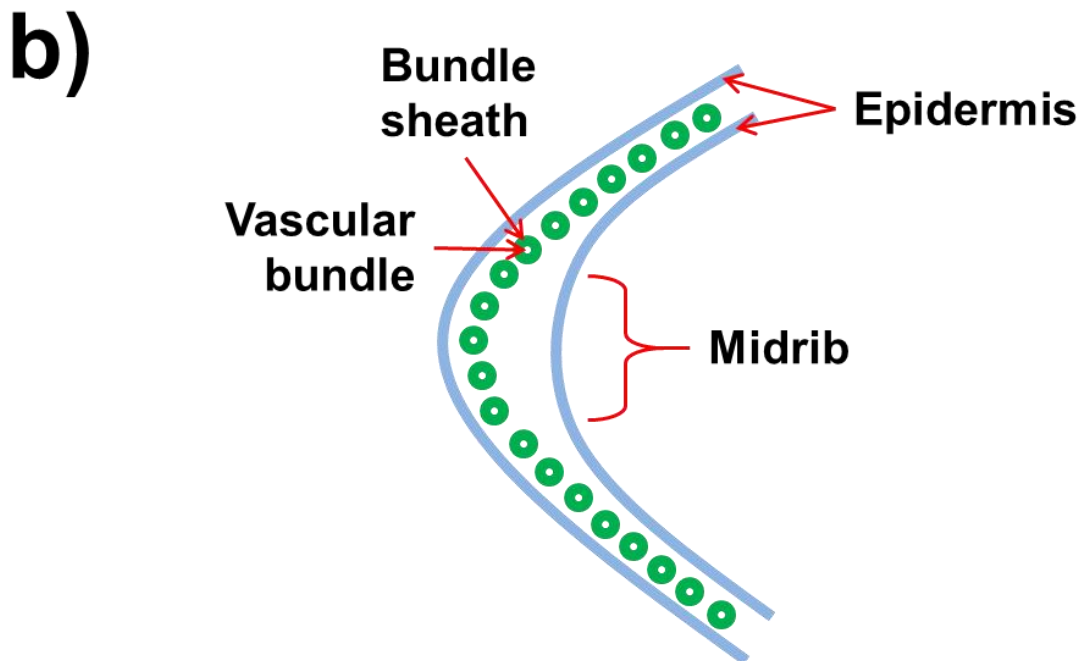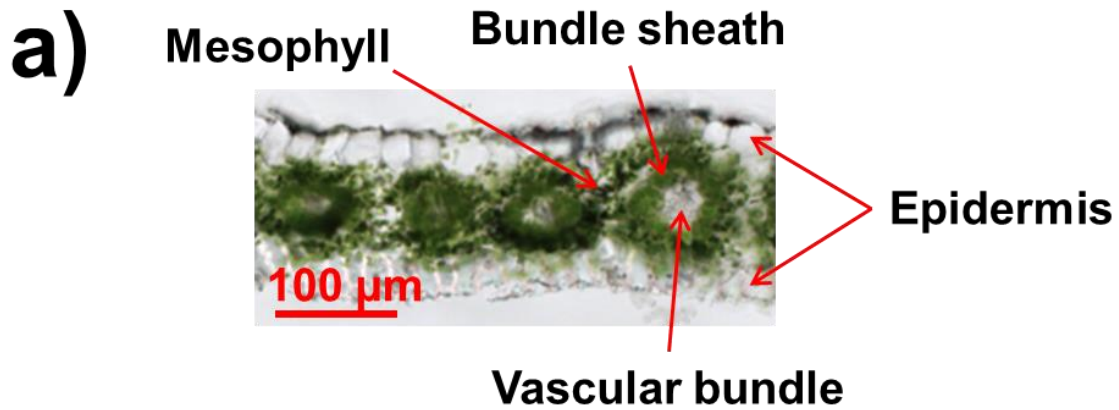
Figure S3. (*a*) Microscope image showing both epidermal layers, vascular bundles, bundle sheaths, and mesophyll within a transverse maize leaf section. (*b*) Schematic representation of the region of tissue imaged in Figure 4, showing the structures discernable from metabolite MS images.

CHAPTER 4

MULTIPLEX MASS SPECTROMETRIC IMAGING WITH POLARITY SWITCHING FOR CONCURRENT ACQUISITION OF POSITIVE AND NEGATIVE ION IMAGES

Andrew R. Korte and Young Jin Lee

Abstract

We have recently developed a multiplex mass spectrometry imaging (MSI) method which incorporates high mass resolution imaging and MS/MS and MS^3 imaging of several compounds in a single data acquisition utilizing a hybrid linear ion trap-orbitrap mass spectrometer (Perdian and Lee, *Anal. Chem.* **82**, 9393-9400, 2010). Here we extend this capability to obtain positive and negative ion MS and MS/MS spectra in a single MS imaging experiment through polarity switching within spiral steps of each raster step. This methodology was demonstrated for the analysis of various lipid class compounds in a section of mouse brain. This allows for simultaneous imaging of compounds that are readily ionized in positive mode (e.g., phosphatidylcholines and sphingomyelins) and those that are readily ionized in negative mode (e.g., sulfatides, phosphatidylinositols and phosphatidylserines). MS/MS imaging was also performed for a few compounds in both positive and negative ion mode within the same experimental set-up. Insufficient stabilization time for the orbitrap high voltage leads to slight

deviations in observed masses, but these deviations are systematic and were easily corrected with a two-point calibration to background ions.

Introduction

Matrix-assisted laser desorption/ionization mass spectrometry imaging (MALDI-MSI) is a rapidly developing and increasingly widespread tool for mapping metabolites and other biomolecules in tissue[78-80]. The development of high-resolution mass spectrometers capable of highly accurate mass measurements has allowed for the analysis of complex tissue samples and the assignment of molecular formulas directly from imaging experiments[81, 82]. MS/MS imaging has also been performed for structural analysis of detected analytes, as well as discrimination of isomers with different on-tissue distributions[22, 23, 83]. We have recently developed a multiplex MS imaging methodology to incorporate high mass resolution orbitrap scans with faster but lower mass resolution ion trap scans in a single imaging experiment. This method allows for the reduction of data acquisition time while achieving MS imaging in both high mass resolution and high spatial resolution. Tandem MS scans can also be included to provide structural information and to reinforce analyte identifications made from accurate mass[23].

Lipids are one commonly studied class of compounds in MSI[84]. The high abundance of lipids in many tissues, established procedures for sample preparation, and minimal delocalization in typical preparation techniques make them good targets for the development and demonstration of MSI techniques. Several recent reviews are available describing lipid

analysis and imaging by different ionization techniques, including matrix-assisted laser desorption/ionization (MALDI)[9], desorption electrospray ionization (DESI)[85], and secondary ion mass spectrometry (SIMS)[86, 87]. Lipid classes investigated by MSI include sterols, fatty acids, phosphatidylcholines (PCs), phosphatidylinositols (PIs), phosphatidylserines (PSs), sphingomyelins (SMs), and sulfatides (STs). With the exception of sterols, these lipids consist of a polar headgroup region and a non-polar hydrocarbon tail region. Differences in headgroup composition lead to significant differences in ionization yield between classes. Generally, those lipids that are detected in high abundance as positive ions are poorly detected or not detected at all as negative ions, and vice-versa[9]. Therefore, more comprehensive lipid data can be obtained by detecting in both positive and negative ionization modes than in a single polarity alone.

One method for acquiring both positive and negative ion mode images in MALDI-MSI is to image two separate tissue samples (e.g. sequential tissue sections), one in positive mode and one in negative mode. This allows for the selection of the best matrix for each polarity. In experiments using two tissue sections, however, comparison of features on positive and negative images requires overlapping the two images by correlating structural features and is not always simple or precise. Depending on the sample and preparation methods, there may be variations in sample composition between adjacent sections. Additionally, acquiring opposite polarity images from separate sections requires the preparation of twice as many samples. For these reasons, it is beneficial to obtain both ion mode images on a single tissue. Thomas and coworkers demonstrated that certain matrixes can be optimized for efficient profiling of lipids for both positive and negative ion mode[65]. Using 1,5-diaminonapthalene as a

matrix, they successfully obtained both positive and negative MS images on a single tissue section by collecting consecutive positive and negative images with a slight position offset. The same method can be also applied by TOF-SIMS for lipid imaging in both polarities on a single section[88]. TOF-SIMS is very attractive for certain applications[88-90] because of its extremely high spatial resolution (down to nanometer size), no need of optimizing matrix for both polarities, and fast data acquisition time; however, MSI of high molecular weight lipids (m/z > 700) is limited due to its low sensitivity.

An alternative way of acquiring opposite polarity MS images on a single tissue would be through repeated polarity switching in a single experiment. It has been recently demonstrated that polarity switching could be used to detect multiple lipid classes in a shotgun lipidomics experiment with electrospray ionization[91]. However, there has been no such experiment in MS imaging on a single tissue. Here we extend our multiplex MS imaging methodology to include polarity switching for imaging of a wide range of lipid classes in a single acquisition. This greatly expands the flexibility of multiplex MS imaging and allows accurate mass imaging of both positive and negative ions along with MS/MS imaging of a few targeted compounds in both polarities.

Experimental

Materials and sample preparation

Coronal sections of mouse brain (striatum, catalog no. MF-201-03) were purchased from Zyagen (San Diego, CA). According to the provider's description, brains were obtained from

CD1 mice, flash frozen, and sectioned in OCT at 7-10 µm thickness. 2,5-dihydroxybenzoic acid (DHB) was purchased from Thermo Fisher (Waltham, MA, USA). Vacuum-sealed tissue sections were allowed to come to room temperature before opening. The tissue was subjected to DHB sublimation without any pretreatment using a procedure described previously[69].

MSI data acquisition

Data was acquired on a linear ion trap-orbitrap mass spectrometer with a MALDI source (MALDI LTQ-Orbitrap Discovery; Thermo Scientific, San Jose, CA) modified to use an external Nd:YAG laser (UVFQ; Elforlight Ltd., Daventry, UK). The laser pump current was set to 80% demand (~1 µJ pulse energy) and the repetition rate was 60 Hz. The laser spot size was estimated to be ~20 µm by observation of burn marks on a thin film of α-cyanohydroxycinnamic acid. Spectra were collected from 20 shots per scan and one scan per spiral step.

The Thermo TunePlus software was used to define the raster pattern: 9 spiral steps per raster step, 25 µm spiral step size, and 100 µm raster step size. MS and MS/MS scans were defined in the Thermo Xcalibur software. A software patch received from the manufacturer was used to reduce the delay time for polarity switching from seven seconds to five seconds. Nine scan events were defined, the same as the number of spiral steps, such that one spectrum was collected from each spiral step. Orbitrap scans were acquired from m/z 150-1000 and CID MS/MS scans were acquired in the linear ion trap with normalized collision energies of 40-60 (arbitrary units) and 1.8 Da isolation widths. m/z of 739.47, 772.53, 782.57, and 826.57 were selected for MS/MS in positive ion mode and 834.52, 885.54, and 906.63 were selected for MS/MS in negative ion mode.

Data analysis

After data acquisition, mass spectra were post-calibrated using the Recalibrate Offline tool (Thermo Fisher Scientific). Positive and negative orbitrap spectra were treated independently. All spectra in a given polarity were averaged, omitting the first 90 minutes of acquisition time. This ensures that masses used for calibration are stable after the initial mass accuracy deviation caused by polarity switching (discussed below). From these averaged spectra, a 'one for all' external recalibration was applied to each individual spectrum. Two background peaks were chosen as calibrant peaks for each polarity. In positive mode the peaks used were m/z 215.1543 (protonated 1,8-bis(dimethylamino)naphthalene (DMAN), a persistent instrumental contaminant from a previous experiment with DMAN as a matrix) and m/z 332.3312 ($C_{23}H_{42}N^+$, an ammonium ion from the tissue embedding medium). Negative mode spectra were calibrated using two matrix peaks, m/z 329.0279 and m/z 681.0450, corresponding to $[2DHB-2H+Na]^-$ and $[4DHB-4H+3Na]^-$, respectively.

ImageQuest software (Thermo) was used to generate MS images. Mass tolerances used for ion image production were ± 0.01 Da for Orbitrap scans and ± 0.5 Da for MS/MS scans. MS images were normalized against total ion count, and MS/MS images were generated without normalization. QualBrowser (Thermo) was used to generate averaged mass spectra.

Results and Discussion

As explained in the experimental section, polarity switching between positive and negative ion mode was adapted by modifying the multiplex MS imaging method previously

developed [6]. In short, each traditional 'raster step' is now broken down to nine spiral steps of smaller MALDI plate movement. The spiral step function is intended to enable spectral averaging within the raster step, but we are utilizing this functionality to acquire multiple data sets within each raster step. Figure 1 illustrates the MALDI plate spiral movement utilized in the current study for multiplex MS imaging with polarity switching. Each raster step is composed of nine spiral steps. Orbitrap scans are acquired in spiral steps **1** (positive) and **6** (negative). MS/MS scans are collected in steps **2-5** (positive) and **7-9** (negative). The polarity is automatically switched from positive to negative between step **5** and **6**, and from negative to positive between step **9** and step **1** of the next raster step. It should be noted that we are incorporating not only high-resolution MS spectra in both polarities but also multiple MS/MS spectra in positive and negative ion modes. Hence, our experimental design corresponds to nine separate MS imaging experiments performed on a single tissue. This represents the first acquisition of MS and MS/MS images in both polarities on a single tissue. Compared to a simple consecutive MS imaging experiment in two polarities [14], the inclusion of multiple MS/MS scans here allows for much more chemical information to be extracted from a single tissue sample.

Figure 2 shows the phospholipid *m/z* range of averaged positive and negative mode spectra for the entire tissue surface after post-calibration with known background peaks. Peaks were assigned based on accurate mass data and comparison to known lipid compounds in mouse brain [9]. Comparison of the two spectra shows completely different spectral patterns, as expected. In positive ion mode, most lipid peaks are assigned to PC and SM species in the form of $[M+H]^+$, $[M+Na]^+$, and $[M+K]^+$. Several fragment peaks are also observed, especially -

N(CH$_3$)$_3$ loss from PC and/or SM, [M+H/K/Na-59]$^+$. Lipid species assigned in negative mode include [M-H]$^-$ species from PS, ST, PG, and PI. Observation of these lipid compounds is consistent with previous findings [14] and suggests both positive and negative ion spectra are necessary to reveal the distribution of various lipid compounds through MS imaging. Mass errors in the recalibrated averaged spectra are below 3ppm for both positive ions and negative ions.

Figure 3 shows images for selected positive and negative ions. Distinct localizations are observed for a number of lipids across a range of classes, including cholesterol, PC, SM, PI, ST, and PS. The distributions of several ions correlate with anatomical structures. As an example, PI (18:0/20:4) is seen in higher abundance in gray matter tissue, while cholesterol is seen in higher abundance in white matter. These distributions are similar to those seen in SIMS imaging performed on similar mouse brain tissue sections by Sjovall et al. [20]. It should be noted that the analysis was performed without tissue washing to remove endogenous salts, and may result in slight differences in apparent distributions of some lipid signals [21]. MS/MS spectra support the assignments of peaks observed in the orbitrap spectra (Figure S1). Figure 3 shows MS/MS images for several structurally informative transitions, including neutral loss (NL) of 183 (phosphocholine headgroup) from PC (32:0), NL of 284 (18:0 fatty acid) from PC (36:1) + K, NL of 304 (20:4 fatty acid) from PI (18:0/20:4), and NL of 338 (C$_{23}$H$_{46}$O fragment of the h24:0 chain). Such fragmentation patterns can be helpful in conjunction with accurate mass data to identify unknowns and to distinguish potentially interfering lipids from different classes.

This experiment incorporated MS/MS scans at fixed *m/z* at seven of the nine spiral steps included in the method. This allows for the generation of images for specific CID fragmentation

patterns (Figure 3). The method can be easily modified to provide different information. MS/MS scans can be replaced by MS^n scans if further structural discrimination is necessary or ion trap MS scans for improved spatial resolution [6]. More importantly, we can perform MS/MS analysis of unknown compounds on-the-fly. This could be accomplished by utilizing the data-dependent scan function of Xcalibur, which selects a few of the most intense ions for MS/MS based on the initial FT scan. Combining this technique with the dynamic exclusion function, one could acquire thousands of MS/MS spectra in a single MS imaging experiment [6]. Namely, as MS imaging is being performed in high resolution MS, MS/MS spectra of thousands of the most intense ions at various locations can be acquired in-tandem for structural analysis later on. While data-dependent MS/MS is commonly adapted to identify peptides using MALDI-tandem mass spectrometry [22], its application to MS imaging is unique in our multiplex-MSI approach [6] and cannot be achieved by a simple back-to-back experiment.

One initial concern with the current approach is that switching the polarity of the orbitrap high voltage may result in the loss of mass resolving power and/or mass accuracy. However, we found there is virtually no change in mass resolving power and the deviation in measured mass is easily correctable by recalibrating after acquisition. In ESI-orbitrap, Schuhmann et al. found that mass accuracy is initially degraded with successive polarity switching but stabilizes over time, taking about 30 minute to come down below 2ppm [18]. The degraded mass error is attributed to the temporarily unstable operation of electronics [18]. We found the same behavior with polarity switching in MALDI-orbitrap. The mass values, however, are stabilized with somewhat shifted mass errors and consistent even after several hours. The amount of mass shift was not consistent depending on the type of experiment, i.e. negative to

positive ion mode and vice versa, or the number of MS/MS included. It was as little as a few ppm and as high as 30 ppm, but in any case it is always stabilized in about 30 minutes in the given experimental condition.

Figure 4 plots the observed mass errors of several ions across the tissue, before and after recalibration. Rastering was performed in the x-direction, so this plot represents mass deviations over the entire scan time, with ~30 to 100 polarity switches between each point, depending upon the raster direction. Recalibration was performed for the entire spectra, with positive and negative ions separately, as described in detail in the Experimental section. After recalibration, average root mean square errors for the plotted ions are 1.6 ppm for positive ions and 1.5 ppm for negative ions. The mass errors following this simple, two-point recalibration are comparable to the instrument's performance without polarity switching.

The greatest limitation in the current multiplex imaging with polarity switching method is the increase in data acquisition time. The total data acquisition time for a 5 x 8 mm^2 rat brain tissue with 100 μm raster steps and nine 25 μm spiral steps is 7.6 hours without polarity switching (i.e., spiral steps **6-9** also in positive ion mode); with polarity switching, the same acquisition takes about 23.9 hours using the original data acquisition software. The additional 16.3 hours are the result of a software-imposed delay of ~7 seconds for each polarity switch. Some delay time is necessary to turn-off the high voltage on orbitrap and turn it back on in the opposite polarity. The physical limit of this time delay is about three seconds in the current design (private communication with the manufacturer). A software patch was generously provided by Thermo Fisher Scientific to reduce the delay time to ~5 seconds. The data presented in this work was obtained with the new software patch and we were able to reduce

the dead time to 10.8 hours, with the total data acquisition time of 18.4 hours. This is a slightly excessive data acquisition time compared to typical imaging experiments, but it is still within the manageable time frame and we could routinely run the polarity switching experiment without any problem.

An ultimate solution to this issue would be the use of dual high voltage supplies. The two high voltage supplies can be maintained at stable voltages in opposite polarities. Polarity switching is then accomplished by simply switching the high voltage supply from one to the other in <0.25sec. This approach has already been adapted in a commercial ESI-orbitrap mass spectrometer (Orbitrap Exactive Plus), which allows acquisition of a set of orbitrap spectra in both positive and negative ion mode in less than one second without compromising mass accuracy [23]. Incorporation of this dual supply system would eliminate the need for a delay between polarity switching and acquisition, and significantly shorten the time required for the described experiment.

Conclusions

A multiplex MALDI-MSI method was adapted to allow for collection of positive and negative ion mass spectrometry images from a single tissue section in a single experiment. Complementary lipid classes were observed in positive and negative mode, and MS/MS data acquisition was incorporated in both polarities. Orbitrap mass values were reproducible across the whole imaging experiment, even after over 10,000 polarity changes, with systematic mass shifts for positive and negative ions. A simple two-point post-calibration to background ion

signals yielded RMS mass errors that averaged <2 ppm, enabling accurate assignments of most lipid compounds. The current limitation is the long data collection time, as a result of the dead time for high voltage stabilization after each polarity switching. However, the data acquisition could still be performed within manageable time frame, ~15 hours, and we could routinely run these experiments without any problem.

The proposed approach has pros and cons compared to acquiring separate MS images for positive and negative ions in a back-to-back experiment. If one simply wants precursor MS data in the two polarities, two separate experiments might be easier and could be done in a shorter time. However, the proposed multiplex MS imaging can easily incorporate MS/MS or MS^3 scans in both polarities into a single experimental scheme. For example, the application demonstrated in this work corresponds to nine separate MS imaging experiments, which is not trivial to be performed in a back-to-back experiment on a single tissue because the experimental set-up would need to be made very carefully to avoid any possible overlapping between each imaging acquisition. Additionally, manual intervention between positive and negative data acquisition is essential to allow complete stabilization, typically requiring two hours, after the polarity switching. In contrast, multiplex MS imaging is rather straightforward to set up and once started runs without further intervention. Furthermore, incorporation of data-dependent MS/MS acquisition during MS imaging is not plausible in a back-to-back experiment. The primary drawback is the longer acquisition time due to the delay between each switching. Considering the facts discussed above, we expect multiplex MS imaging with polarity switching could be quite useful in many applications.
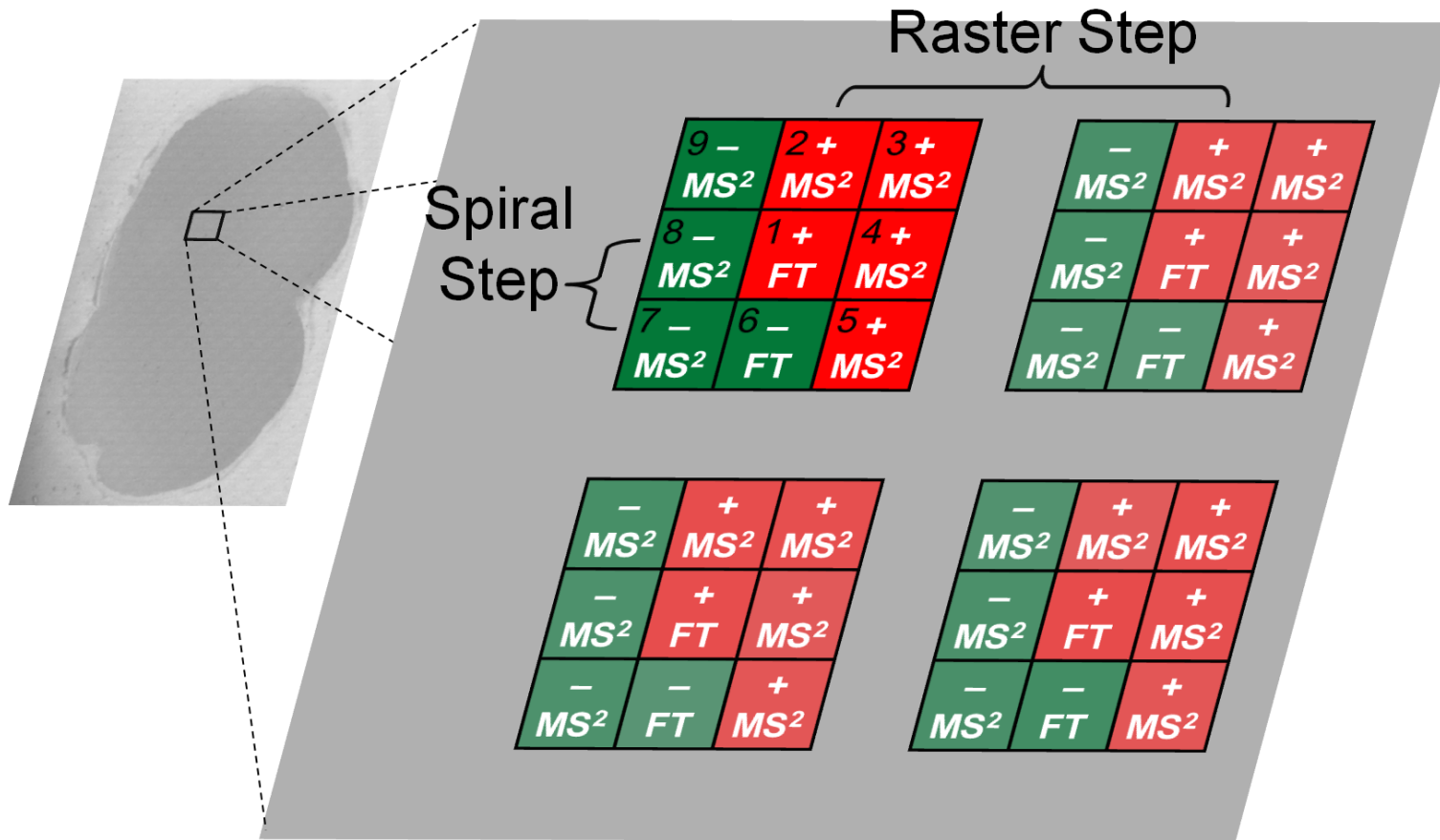
Acknowledgments

Figure 1. Illustration of spiral movement of MALDI plate and spectral acquisition method at each spiral step. The numbers indicate the order of spiral movement. A spiral step size of 25 µm (e.g. 1→2) and a raster step size of 100 µm (e.g. 1→1) were used in this experiment. FT indicates Orbitrap data acquisition. MS² indicates ion trap MS/MS scans. MS/MS spectra were obtained for four positive ions and three negative ions using the linear ion trap.
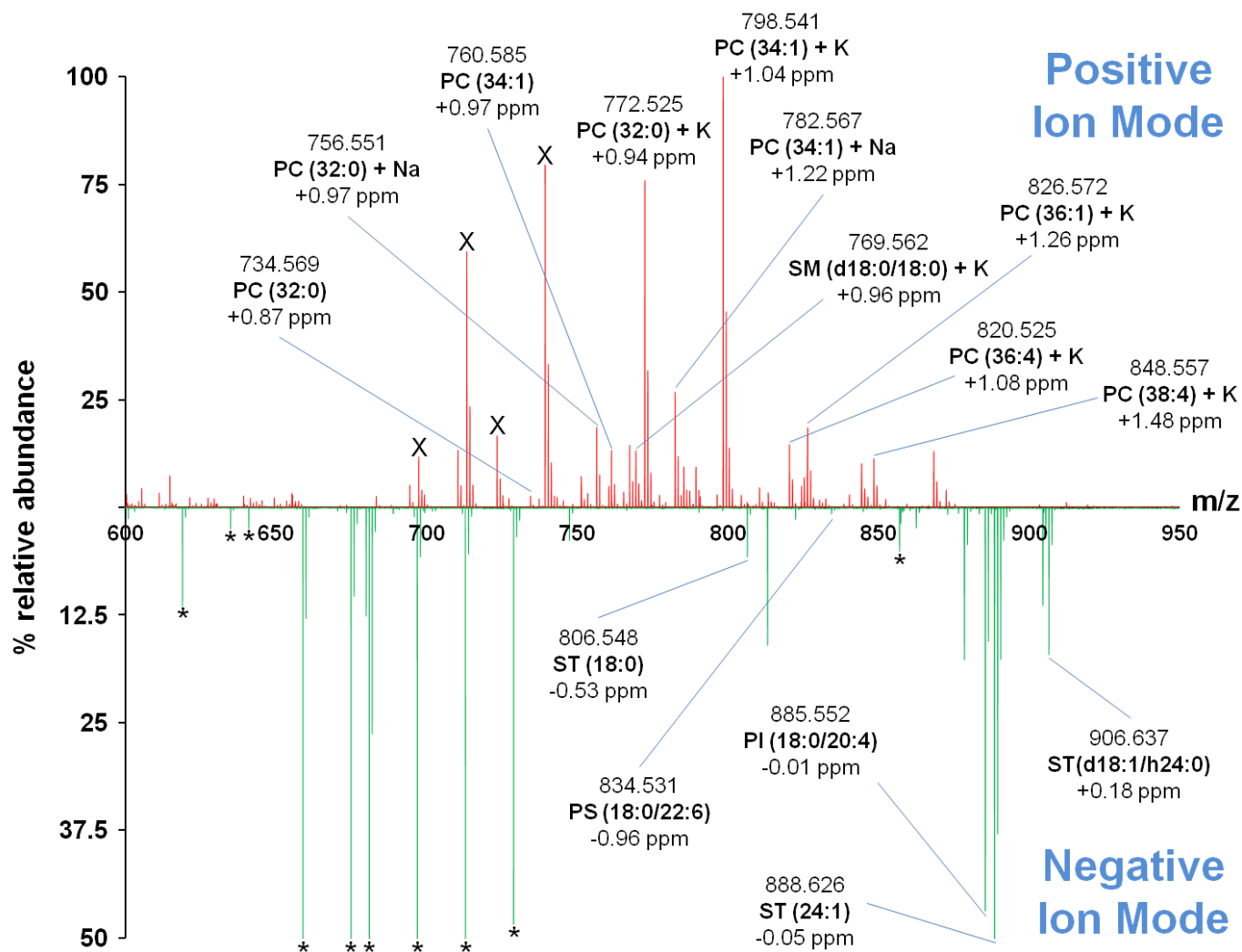
Figure 2. Phospholipid *m/z* range of averaged positive (above axis) and negative (below axis) spectra obtained from coronal mouse brain section showing assignments for selected lipid ions and deviations from calculated values. Spectra were recalibrated against background ions after acquisition. X indicates fragments such as the loss of $N(CH_3)_3$ and * represents matrix ion peaks.
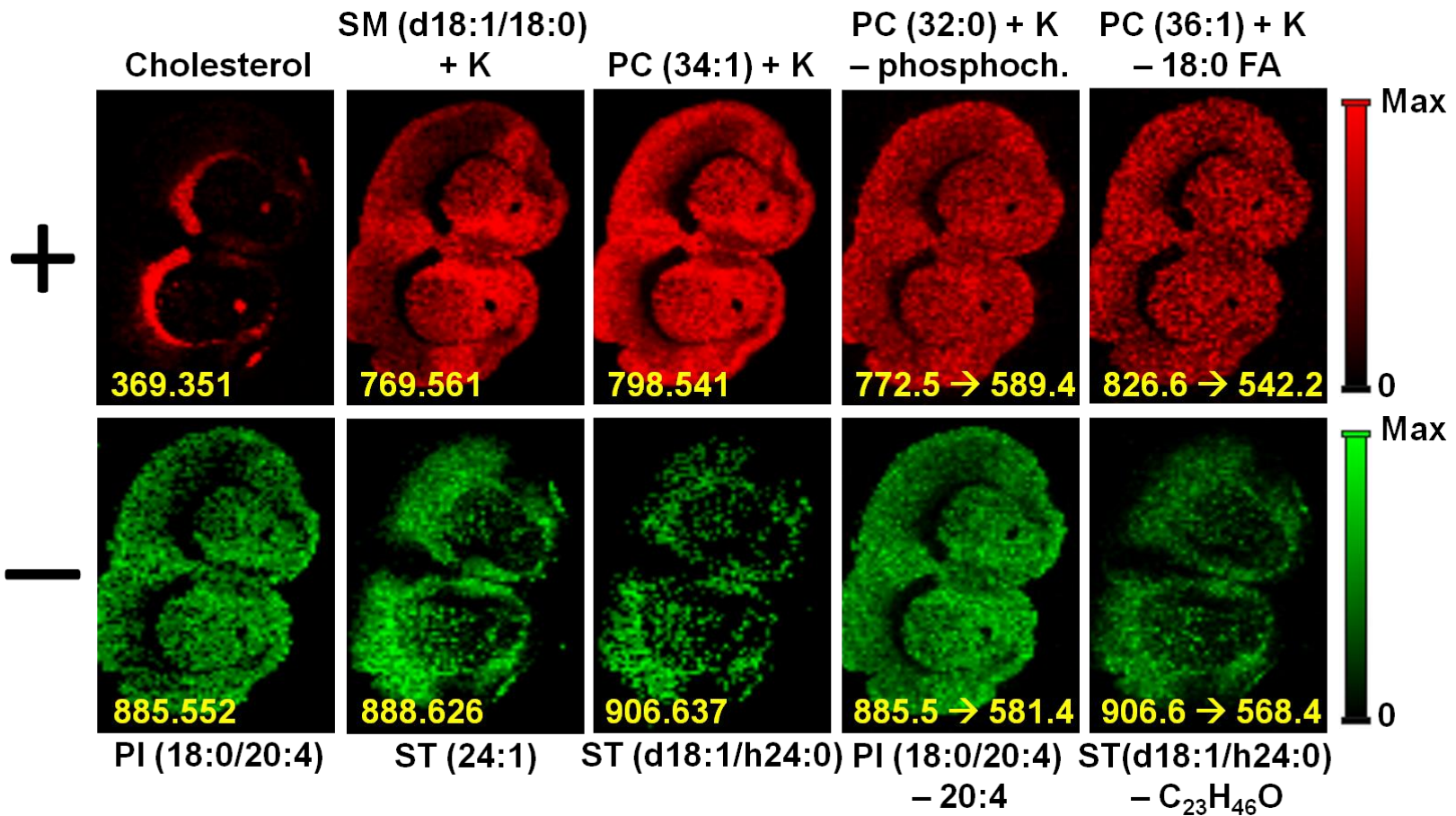
Figure 3. MS and MS/MS images for selected lipid ions. Red images are generated from positive ions, green images from negative ions. MS images are normalized to total ion count and MS/MS images are produced without any normalization.
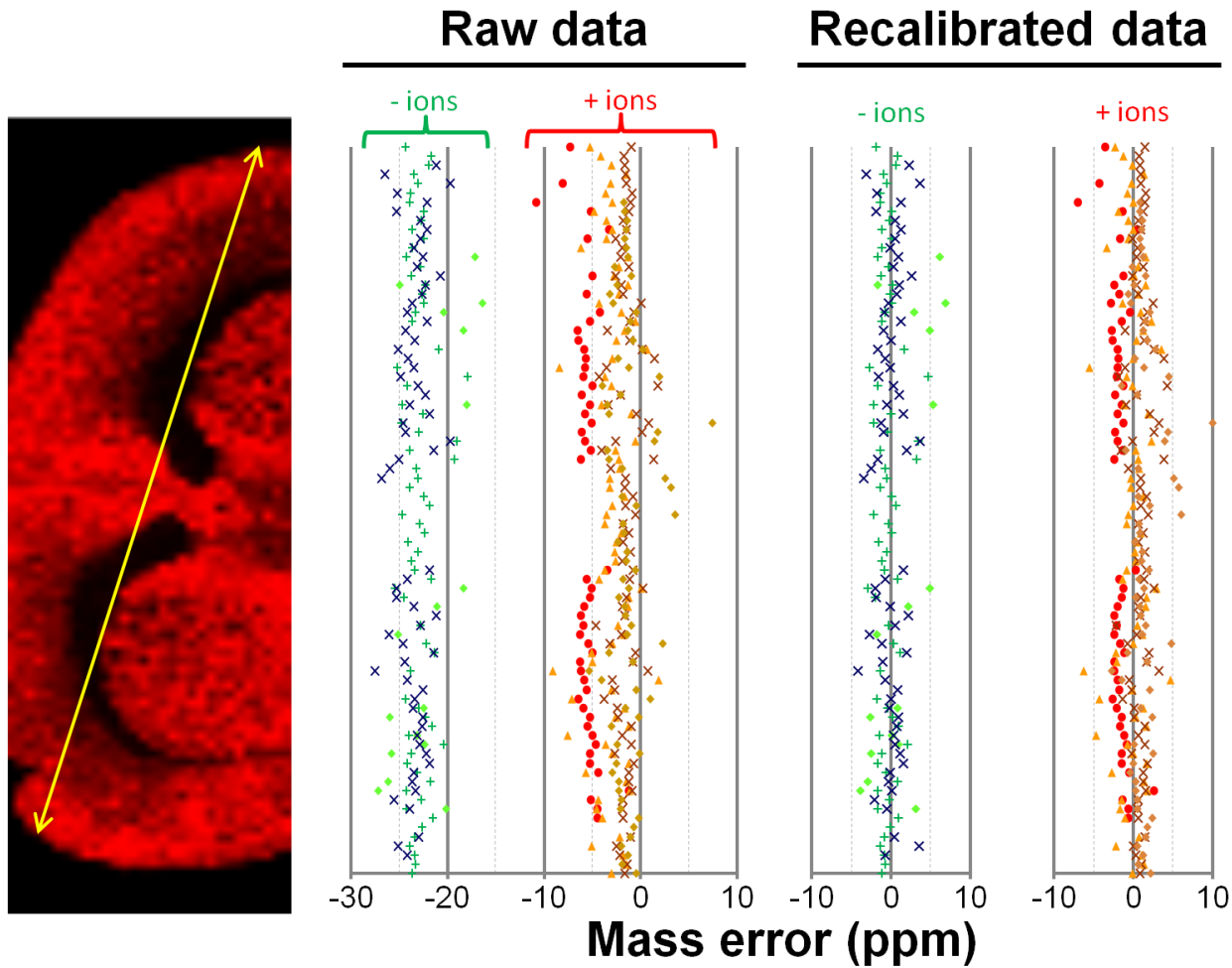
Figure 4. Mass errors of selected compounds across the tissue along the arrow shown on the left, before and after a two-point mass recalibration. Orange-red symbols indicate positive ions: (●) m/z 369.351, [Cholesterol − H_2O + H]$^+$; (▲) m/z 577.519, [34:1 diacylglycerol fragment + H]$^+$; (◆) m/z 772.525, [PC (32:0) + Na]$^+$; (×) m/z 798.541, [PC (34:1) + K]$^+$. Green-blue symbols indicate negative ions: (+) m/z 465.044, [3DHB − H_2O − 2H + Na]$^-$; (◆) m/z 806.548, [ST (18:0) − H]$^-$; (×) m/z 885.552, [ST (24:1) − H]$^-$.
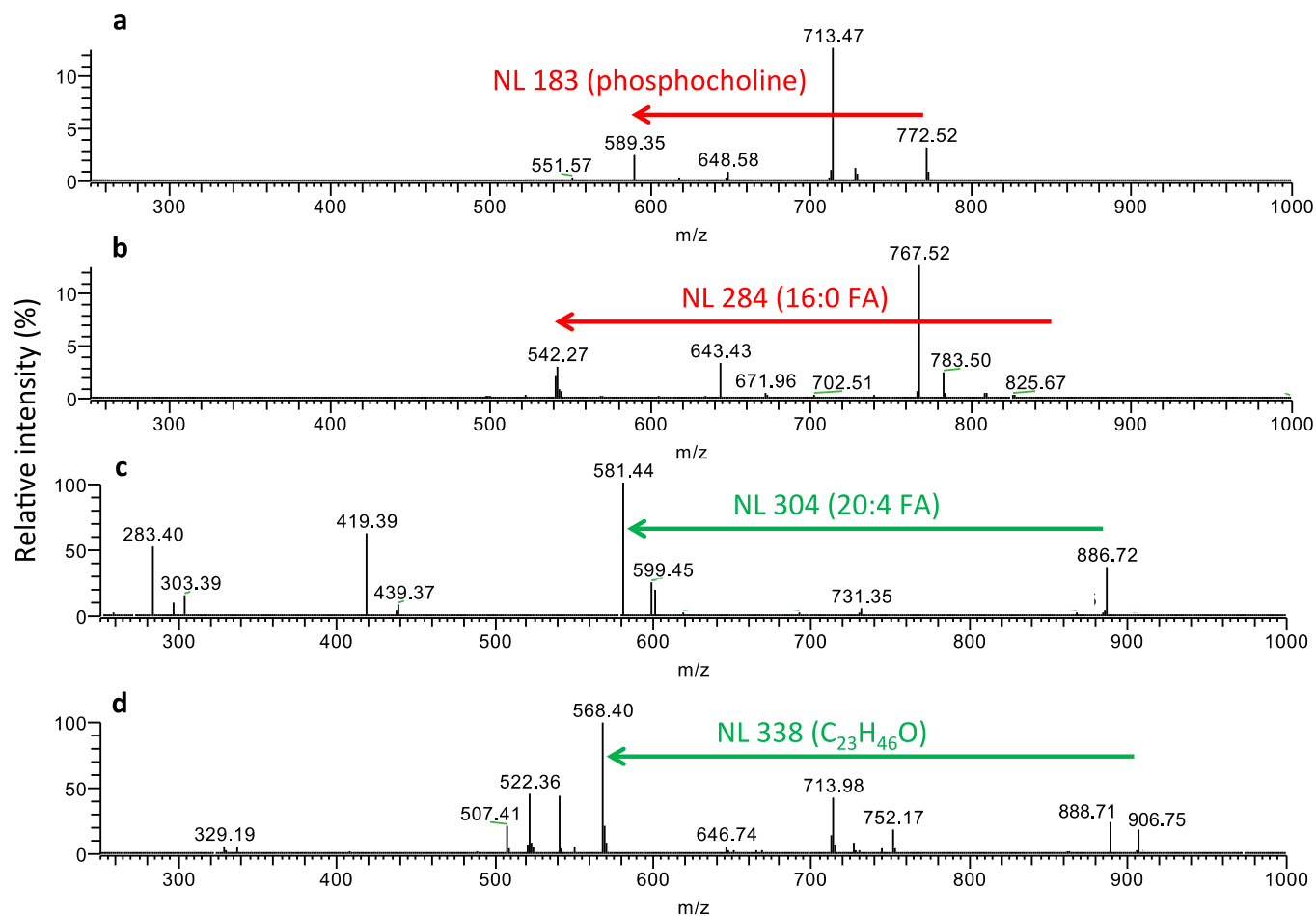
Figure S1. MS/MS spectra used to generate MS/MS images in Figure 3. MS/MS of [PC (32:0) + K]$^+$ (a), MS/MS of [PC (36:1) + K]$^+$ (b), MS/MS of [PI (18:0/20:4) – H]$^-$ (c) and MS/MS of [ST (d18:1/h24:0) – H]$^-$ (d). Transitions used to generate images are labeled.

CHAPTER 5

SINGLE-CELL MALDI-MS IMAGING OF CORN LEAF METABOLITES BY MODIFICATION OF MALDI-LTQ-ORBITRAP DISCOVERY OPTICS

Abstract

A significant limiting factor in the achievable spatial resolution of MALDI-MS imaging is the size of the laser spot at the sample surface. Here we present modifications to the beam-delivery optics of a commercial MALDI-LTQ-Orbitrap instrument that incorporates an external Nd:YAG laser, beam-shaping optics, and an aspheric focusing lens to reduce the laser spot size from ~50 μm for the commercial configuration to ~5 μm. This system is then applied for MALDI-MS imaging of cross-sections of corn leaves. Compounds including primary metabolites, amino acids, glycerolipids, and defense compounds are localized with a resolution well below the size of a single cell for the studied tissue type. Differences in tissue type (e.g. epidermis, mesophyll, and bundle sheath) are apparent in metabolite ion images and correlate well with optical images and known tissue functions.

Introduction

A number of factors influence the achievable spatial resolution in MALDI-MSI. These include tissue preparation (avoiding damage to the tissue or delocalization of endogenous compounds), matrix application (obtaining a homogenous layer of matrix), laser spot size (the area from which compounds can be desorbed and ionized in a single spectrum), and sensitivity

(sufficient detection of compounds of interest even at the reduced sampling volumes of high-resolution imaging).

Tissue preparation considerations can largely be addressed by flash-freezing, cryosectioning, and lyophilizing samples after harvesting[28]. Sublimation-vapor deposition, originally developed for MALDI-MSI by Hankin et al., has become a common method of deposition for organic matrices, and yields a homogenous matrix coating with small crystal sizes[69]. By definition, high-spatial resolution imaging requires sampling of a smaller region of tissue for each individual pixel. This reduced sampling volume means fewer ions are generated per pixel, and leads to decreased sensitivity at higher spatial resolutions. As demonstrated by Knochenmuss, however, the loss of sensitivity is not as drastic as predicted strictly by sampling volume. Smaller spot sizes provide greater ion yields per unit area at constant fluence[92]. Additionally, sensitivity concerns can be minimized by the use of efficient transmission of ions to the mass analyzer. In this regard, commercial ion sources are often superior to custom-built sources, making modification of a commercial source an appealing prospect for improving spatial resolution.

As a result of these advancements, laser spot size is typically the limiting factor for MALDI-MSI spatial resolution. Early MALDI-MSI experiments were performed at moderate spatial resolutions of 50-100 µm, and for many applications this resolution is sufficient. More recently, however, systems capable of higher spatial resolution have been developed. A generation of commercial MALDI-MSI-capable instruments has been introduced that is routinely capable of a 10 µm spot size[93]. Spengler's group has recently developed an atmospheric pressure MALDI source capable of imaging resolutions as high as 3.0 µm[94]. Most

recently, Zavalin et al. modified a commercial MALDI-MS instrument to improve spatial resolution from the manufacturer-specified 20 μm to 5 μm[95]. In this work, we adapt these changes for incorporation into another MALDI platform, resulting in an improvement in spot size from ~50 μm for the commercial configuration to ~5 μm for the modified configuration.

Demonstration of single-cell plant MALDI-MSI of metabolites requires a test system with a clear cell-to-cell variation in metabolism. Corn engages in a relatively rare photosynthetic process known as C_4 carbon fixation, which localizes certain photosynthesis-related enzymes (and thus metabolites) to specific cell types[96]. Proteomics studies have also found significant differences in protein expression between the two cell types, suggesting additional metabolite distribution differences might be observable[97]. Therefore, to illustrate the high-spatial resolution capabilities of the modified instrument, 5 μm imaging of corn leaf cross-sections was performed.

Experimental

Materials

1,5-diaminonaphthalene (DAN, 97%) and 2,5-dihydroxybenzoic acid (DHB, 98%) were purchased from Sigma-Aldrich (St. Louis, MO). A 355 nm frequency-tripled Nd:YAG laser (model UVFQ) was purchased from Elforlight, Ltd. (Daventry, UK). Optical components including cage rods, support plates, optical element mounts, laser line mirrors (NB1-K08), dichroic mirror (HBSY13), quartz window (WG41050), aspheric singlet (A220TM-A,) spherical singlet (LA1509-A)

and UV achromatic doublet (ACA254-100-UV) were purchased from Thorlabs (Newton, NJ). A

high-energy 25 μm pinhole (HEA-25C-R) was purchased from Lenox Laser, Inc (Glen Arm, MD).

Optical modification

Note: A description of the commercial MALDI source design is available in this reference[98].

The diffraction-limited spot size for a focused laser beam is defined by Equation 1[95]:

(Equation 1)
$$D_s = M^2 \cdot \frac{4}{\pi} \cdot \lambda \cdot \frac{f}{D_b}$$

D_s = Diffraction-limited spot size
M^2 = Beam quality factor (perfect Gaussian shape = 1)
λ = Wavelength
f = Focal length
D_b = Input beam diameter

The minimum spot size can therefore be achieved by minimizing M^2 (optimizing beam shape),

minimizing f (placing the focal lens as close to the sample as possible), and maximizing D_b

(expanding the beam before the focal lens). In the MALDI source used for this instrument,

placement of ion optics requires the use of a long-focal length lens for final focusing.

Therefore, this work focuses primarily on improving beam shape and expanding the beam prior

to focusing by the installation of a spatial filter/beam expander in the optical path. The final

focusing lens, originally a spherical singlet, was replaced with a UV-optimized aspheric doublet

to minimize the effect of optical aberrations, which can limit the practically-achievable spot

size.

A schematic and photograph showing the modified optical system are available in

Figures 1a and 1b, respectively. In this configuration, the stock nitrogen laser of the MALDI

source is bypassed and the external Nd:YAG laser is used for desorption. The optical path is as follows, with the elements labeled in Figures 1a and 1b:

(1-3)   Beam-stirring mirrors to lift the beam and direct it to the instrument aperture

(4)   Aspheric lens to focus through pinhole (f = 11.0 mm)

(5)   25 µm high-damage threshold pinhole

(6)   Spherical collimating lens (f = 100 mm)

(7)   CCD camera for optical observation of tissue samples

(8)   Dichroic mirror to reflect 355 nm laser while passing visible light to CCD camera

(9)   Quartz window to provide isolation between atmosphere and in-source vacuum

(10)   Aspheric doublet lens to focus beam to sample surface (f = 100 mm)

(11)   Ion optics to transmit generated ions into mass analyzer

Elements 4-6 together compromise a combination beam expander/spatial filter. The position of the spatial filter focusing lens (4) and pinhole (5) were adjusted to optimize throughput and beam shape, then fixed in place. The position of the collimating lens (6) was adjusted to produce a well-collimated output from the spatial filter assembly and also fixed. To find the optimal position for the final focusing lens, a microscope slide was coated with DHB and a line of ablation spots at low laser energy (79.0% of pump diode current) was laid down. The instrument was vented and opened, the lens position was adjusted 150 µm, the system was pumped down again, and a new set of ablation spots was laid. The spot sizes were then measured using an optical microscope and the lens was returned to the position yielding the smallest ablation spots.

Plant growth and sample preparation

Corn seeds (*Zea* mays, inbred B73) seeds were planted in soil and grown under controlled conditions in a greenhouse. 14 days after planting, a healthy plant was selected and the third true leaf was pulled from the stalk in daylight (1:00pm). A portion of the leaf ~2 cm long was cut from the midpoint of the leaf.

Embedding and sectioning were conducted using the procedure described in Chapter 3. Briefly, samples were embedded in gelatin, rapidly frozen, cryosectioned to 10 μm thickness, then gradually warmed and dried under vacuum. Matrix (DAN) was applied by sublimation (~50 mtorr, 140 °C, 3.5 min heating time). A tissue section adjacent to the one used for MALDI-MSI was used to collect optical microscope images.

Mass spectrometry analysis

MALDI-MSI was performed using a MALDI-LTQ-Orbitrap Discovery platform (Thermo Scientific, San Jose, CA). Tune and Xcalibur (Thermo Scientific) software were used to define imaging acquisition parameters. Images were acquired at a raster step size of 5 μm. The laser pump diode current was set to 80.5% of maximum, resulting in an output energy of ~1-1.5 μJ/pulse. Each spectrum was acquired with 10 laser shots, and a single spectrum was collected at each raster point. Spectra were acquired in negative mode using the Orbitrap analyzer at the 30,000 mass resolution setting with a scan range of *m/z* 100-1000. After acquisition, images were generated using ImageQuest software (Thermo Scientific). Images were created with a *m/z* width of ±0.005 and were normalized to the total ion count from each pixel.

After imaging, tandem MS spectra for selected compounds were acquired manually on a parallel section. 10 scans were averaged from a region of tissue where the ion of interest was found to be abundant in the imaging experiment. MS/MS spectra were acquired in the ion trap analyzer, and collision energies were individually optimized for each analyte.

Results and Discussion

Laser spot size measurement

The minimum achieved laser spot size, as estimated by the size of the ablation spot, was ~5.1 µm in diameter. An optical microscope image showing a series of ablation spots on a thin coating of DHB matrix is presented in Figure 2. As the laser energy distribution is Gaussian, the ablation spot size depends on the laser pulse energy. The slight increase in laser energy required for adequate MS signal during imaging experiments means the spot size at the actual sample surface is likely slightly larger than that measured on the DHB-coated slide. Therefore, the imaging experiment described here represents an oversampling approach, where the laser spot size is larger than the raster step size. It has been demonstrated that moderate oversampling can be an effective approach for high-resolution MALDI-MSI, provided the matrix material is completely ablated at each step[99]. The use of sublimation to apply a very thin matrix layer ensures this is the case, and both visual inspection and subsequent interrogation with the laser indicate the matrix is completely ablated at each pixel.

Corn leaf imaging

A collection of MALDI-MS images generated from a portion of a corn leaf cross-section is presented in Figure 3, along with an optical microscope image of the scanned region of tissue. An image showing the scanned region within the context of the entire leaf section is presented in Supplemental Figure 1. Assignments of signals are based upon accurate mass measurements (Supplemental Table 1) and signals for which useful MS/MS spectra were obtained are presented in Supplemental Figure 2. For reference of the structure of the corn leaf, it may be useful to refer to Figure S3 of Chapter 3.

Signals detected and showing distinct localizations on the corn leaf tissue are assigned to a wide range of metabolite classes, including amino acids (glutamic acid), cell wall components (caffeic acid, ferulic acid), defense compounds (HMBOA-glucose), sugars/phosphate sugars (sucrose, glucose-6-phosphate), flavonoids and flavonoid glycosides (Luteolin/kaempferol, maysin, and rutin) and glycerolipids (PG [34:2] and SQDG [34:3]). Of the metabolites observed in the sample in Chapter 3, only asparagine (m/z 131.046) and malic acid (m/z 133.014) were not detected in significant quantity. However, aspargine was observed primarily localized to the midrib region of the plant, which was not scanned in this experiment. The reason for the lack of detection of malic acid is unclear.

A number of distinct metabolite distributions are apparent in the MALDI-MS images. Many of the observed distributions, such as glutamic acid, ascorbic acid, HMBOA-glucose, maysin, and SQDG (34:3) are similar to those seen in Chapter 3. As before, flavonoids are observed within the epidermal tissue layers, SQDG is detected within the photosynthetic tissue

surrounding the vascular bundles, and HMBOA-glucose is detected in the mesophyll between the vascular bundles.

The signal at *m/z* 285.040, tentatively assigned in Chapter 3 as kaempferol based on accurate mass, was also further investigated by MS/MS. MS/MS spectra for this ion were collected from both epidermal surfaces, and the averaged spectrum for this ion was compared to the work performed by Fabre et al[100]. The presence of peaks corresponding to both kaempferol and luteolin suggests that the *m/z* 285.040 signal arises from a mixture of the two isomers. The two signals cannot be distinguished from MS scans alone, but future applications of tandem MS imaging, similar to that performed in Chapter 4 should allow for the differentiation of the two and determine whether they exhibit different distributions within the tissue.

The significantly higher spatial resolution afforded by the new optical setup allows for the distinction of much finer features from metabolite images. These features are most readily seen by overlaying MS images, as in Figure 4. In each image, the luteolin/kaempferol signal (*m/z* 285.040) is presented in green and clearly outlines the epidermal tissues on the top and bottom surface of the leaf. Figure 4b displays PG (34:2) in blue and sucrose in red, with PG (34:2) observed in the bundle sheath cells around the vascular bundles and sucrose detected largely within the vascular bundles themselves. A primary function of vascular tissues in plants is to transport sucrose[101], reinforcing the assignment of this signal.   Figure 4c displays PG (34:2) again in blue and HMBOA-glucose in red. HMBOA-glucose is notably detected within the interior mesophyll cells between the vascular bundles, but not within the bundle sheath or

vascular bundle or near the epidermal layer. The biological foundation and implications of this distribution are not immediately clear, but warrant further investigation.

Figure 4d presents the distributions of three flavonoid metabolites: rutin (blue), maysin (red), and luteolin/kaempferol (green). This overlay highlights the varied distributions seen for metabolites even within the same class of compounds. Maysin is again detected almost exclusively on the upper surface of the leaf, rutin is largely localized to the upper surface but is detected at high abundance near the bottom right of the imaged section, and luteolin/kaempferol is detected in roughly equal abundance in both leaf surfaces. The non-uniform distribution of some flavonoids between upper and lower epidermal layers is in agreement with that reported by Suzuki et al[102].

Figures 4e and 4f clearly demonstrate the high spatial resolution capabilities of the modified instrument. Figure 4e plots PG (34:2) in blue and SQDG (34:3) in red. PG (34:2) is detected in narrow (~30-40 μm) bands around the vascular bundles, while SQDG is detected throughout the interior regions of the leaf, excluding the vascular bundles. Both PG and SQDG are known to be a major component of thylakoid membranes[103], and the 34:2 and 34:3 forms, respectively, have been demonstrated to be highly abundant in corn leaf portions such as the ones sampled in this study[104, 105]. The apparent difference in PG abundance between mesophyll and bundle sheath cells is not readily explainable, but clearly demonstrates the mesophyll and bundle sheath cells can be differentiated based on metabolite content.

Figure 4f again presents the luteolin/kaempferol signal in green and an unidentified signal at *m/z* 587.503 in red. Although a confident assignment is not made for this signal, the high mass defect suggests it is a highly-saturated lipid-like compound. Combined with the

observed localization of the signal, directly outside the luteolin/kaempferol signal, this suggests that the ion may arise from a cuticular lipid compound. The close proximity but clear resolution of these two signals again demonstrates the utility of the high spatial resolution enabled by the developed system.

Conclusions

Here we have modified the beam delivery optics of a Thermo MALDI-LTQ-Orbitrap Discovery mass spectrometer to produce laser spot sizes as small as 5 μm. Preliminary experiments have shown that high resolution (5 μm) imaging of tissue sections is possible, and apparent single-cell metabolite content differences have been observed. Experiments are currently underway to image corn leaf cross-sections at different developmental stages and different harvest times (e.g. day vs. night). Ongoing and future experiments will also seek new matrices and sample preparation methods to improve sensitivity and allow imaging of additional metabolite classes, with a particular emphasis on examining the metabolic differences between mesophyll and bundle sheath cells that are associated with C4 photosynthesis. The high spatial resolution capabilities of this instrument will also be applied to the study of additional tissue types and processes, such as *Arabidopsis* seeds and germinating corn seeds.

Acknowledgment
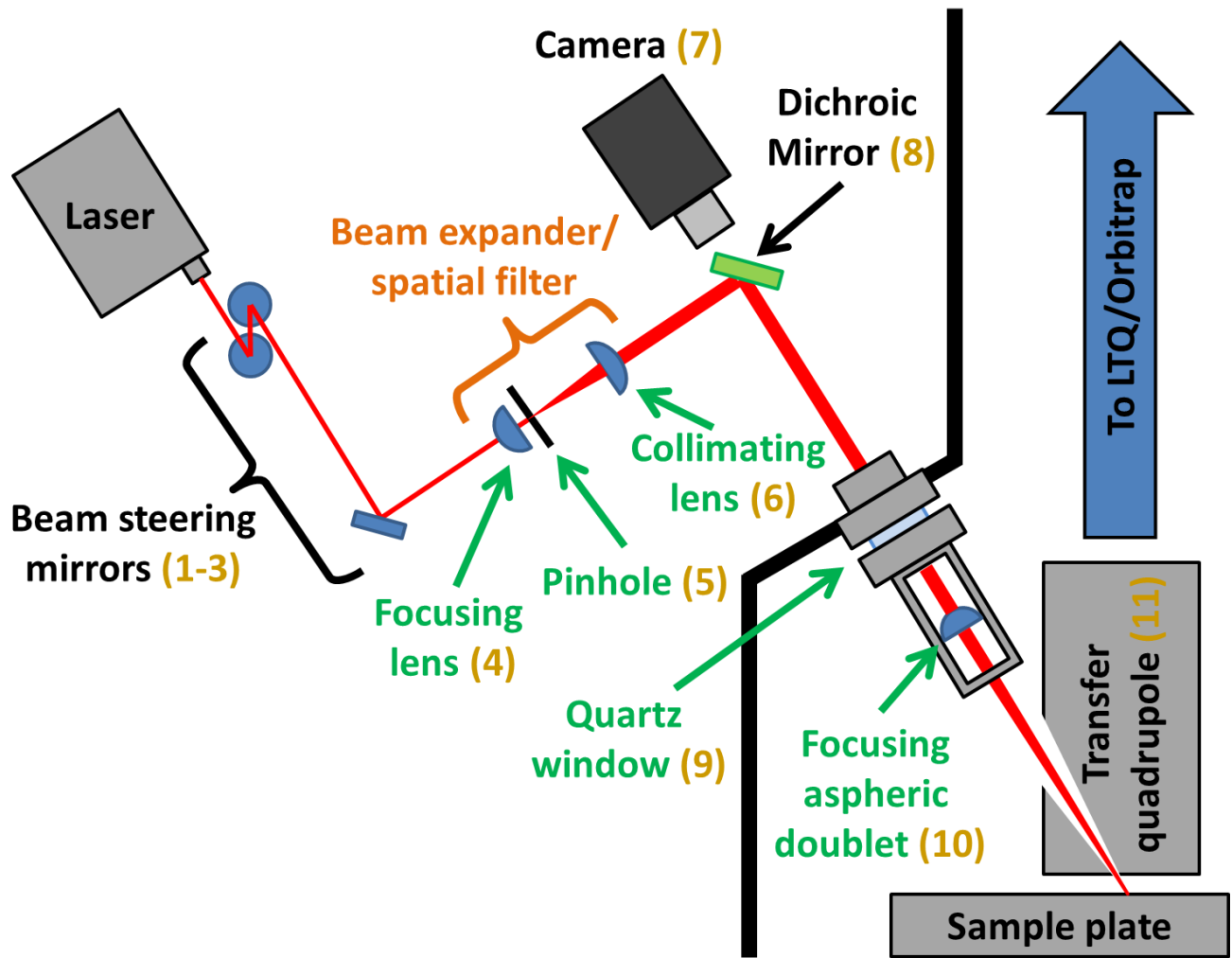
Figure 1a. Schematic of modified beam delivery optics.
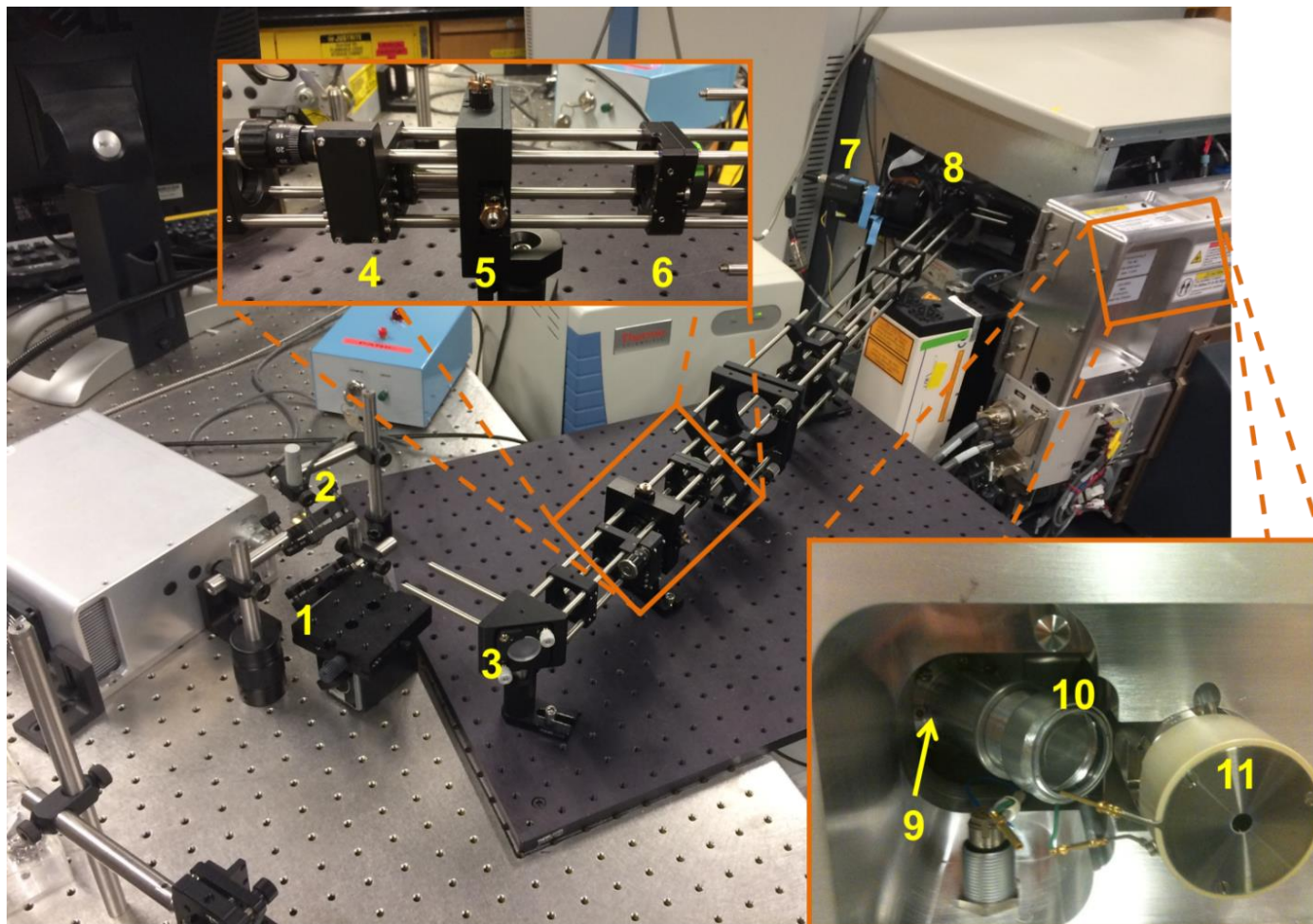
Figure 1b. Photographs of modified beam delivery optics.
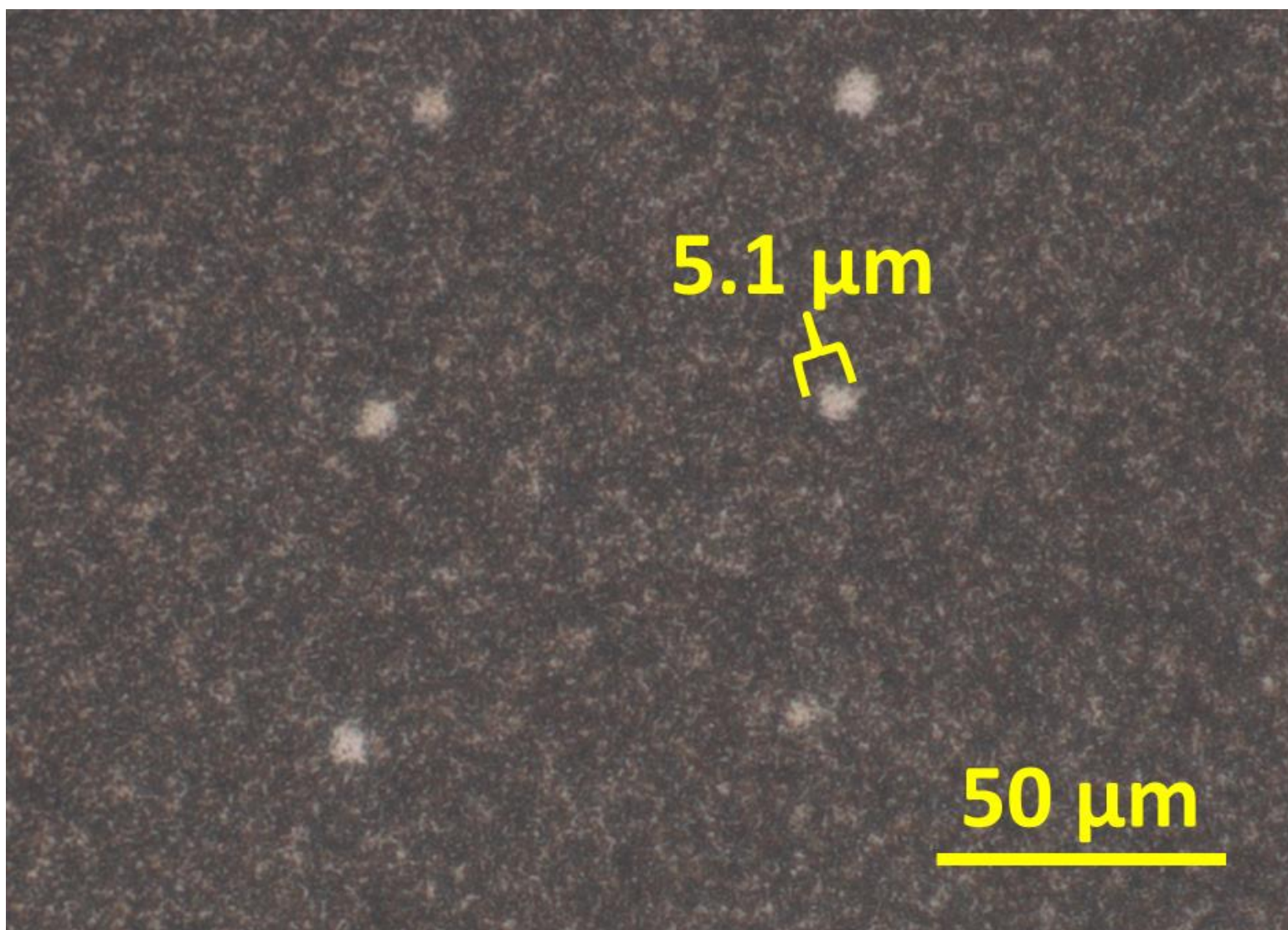
Figure 2. Optical micrograph of laser ablation spots on a thin film of 2,5-dihydroxybenzoic acid matrix. Spot diameter was measured using integrated microscope software.
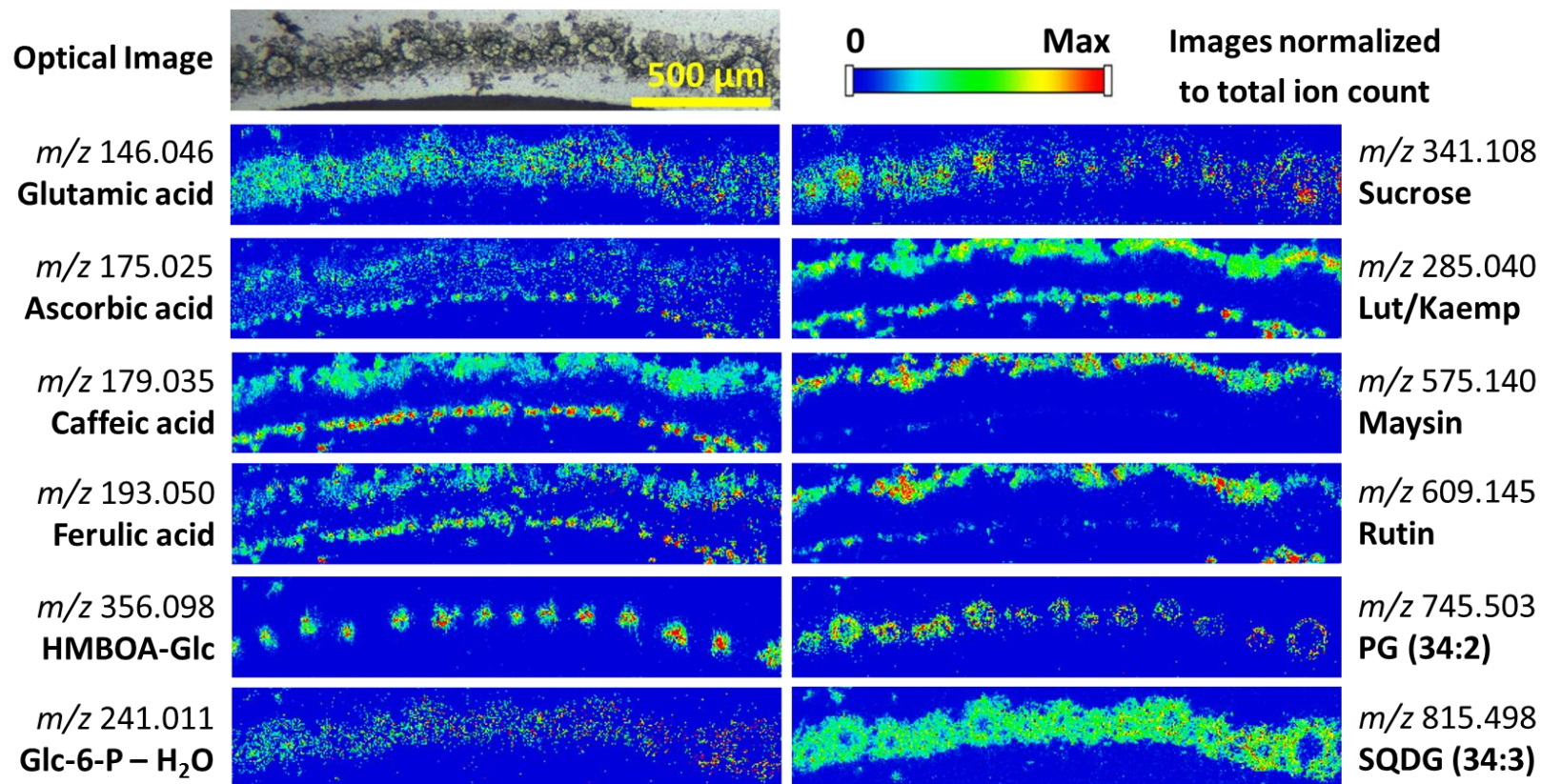
Figure 3. Optical (top left) and 5 μm raster step size MS images of various metabolites in corn leaf cross-section. Images are oriented such that the upward-facing (adaxial) surface of the leaf is at the top. HMBOA-Glc: 2-hydroxy-7-methoxy-1,4-benzoxazin-3-one; Glc-6-P: Glucose-6-phosphate; Lut/kaemp: isomeric flavonoids luteolin and kaempferol. PG: phosphatidylglycerol; SQDG: sulfoquinovosyl diacylglycerol. Signals are normalized to per-pixel TIC. Max values for generating images are as follows. Glutamic acid: 1×10^{-2}. Ascorbic acid: 8×10^{-3}. Caffeic acid: 3.5×10^{-2}. Ferulic acid: 8×10^{-3}. HMBOA-Glc: 3×10^{-2}. Glc-6-P – H2O: 4×10^{-3}. Sucrose: 6×10^{-3}. Lut/kaemp: 5×10^{-2}. Maysin: 5×10^{-2}. Rutin: 2×10^{-2}. PG (34:2): 5×10^{-3}. SQDG (34:3): 3×10^{-2}.
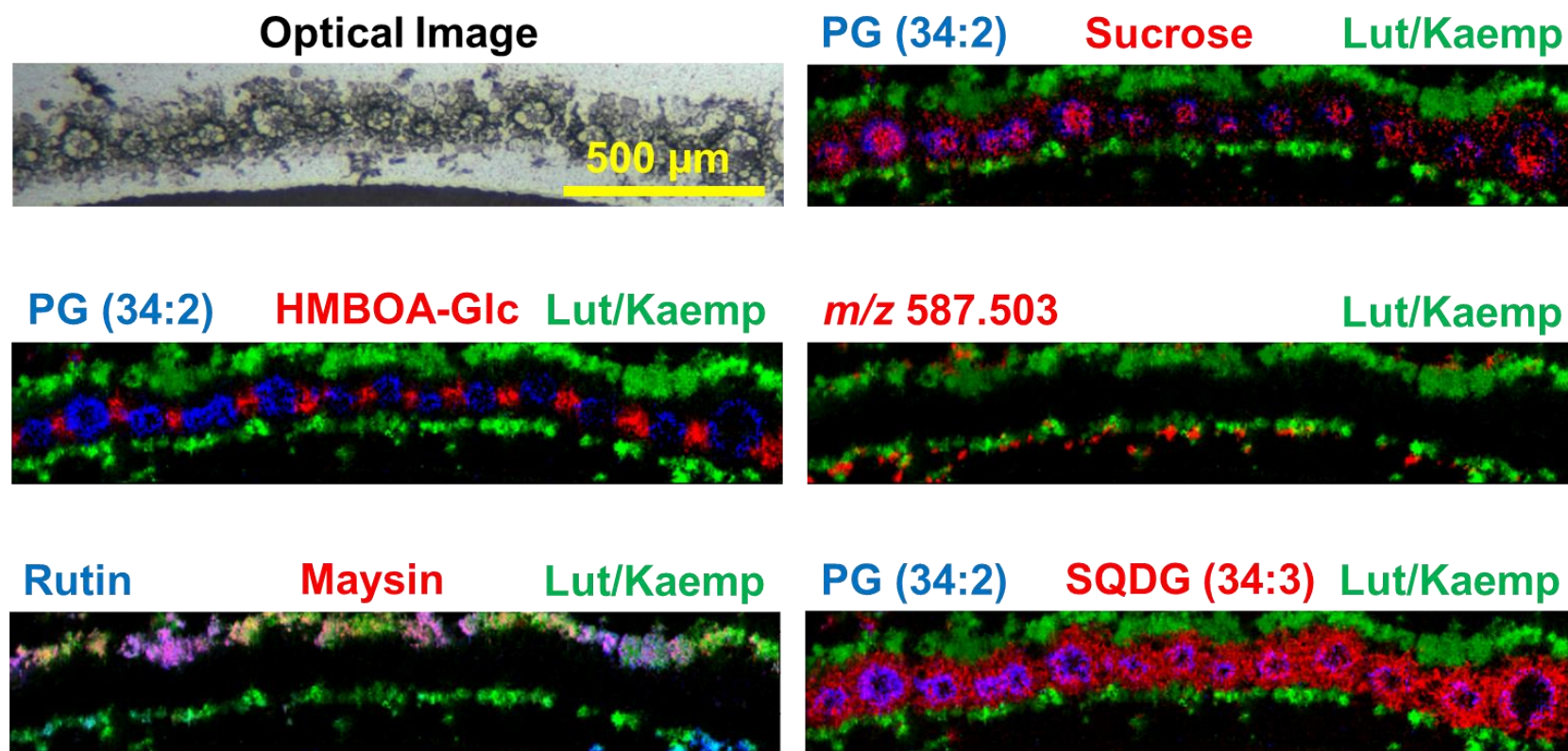
Figure 4. Optical image (a) and overlays of MALDI-MS images(b-f). All signals are normalized to per-pixel TIC. Max values were individually adjusted to provide contrast within images.

Supplemental Table and Figures

Supplemental Table 1. Detected *m/z*, assigned formula, and mass errors for signals used to generate images in Figure 3. Except glucose-6-phosphate, all formulas represent the [M−H]⁻ species.

m/z	Formula	ID	Error (ppm)
146.046	C5H8NO4	Glutamic acid	+0.3
175.025	C6H7O6	Ascorbic acid	-0.4
179.035	C9H7O4	Caffeic acid	-0.7
193.050	C10H9O4	Ferulic acid	-1.5
241.011	C6H10O8P	Glucose-6-phosphate – H2O	-2.8
285.040	C15H9O6	Luteolin/kaempferol	-2.5
341.108	C12H21O11	Sucrose	-2.4
356.098	C15H18NO9	HMBOA-glucose	-2.6
575.140	C27H27O14	Maysin	-0.9
609.145	C27H29O16	Rutin	-1.1
745.503	C40H74O10P	PG (34:2)	+0.3
815.498	C43H75O12S	SQDG (34:3)	+0.0
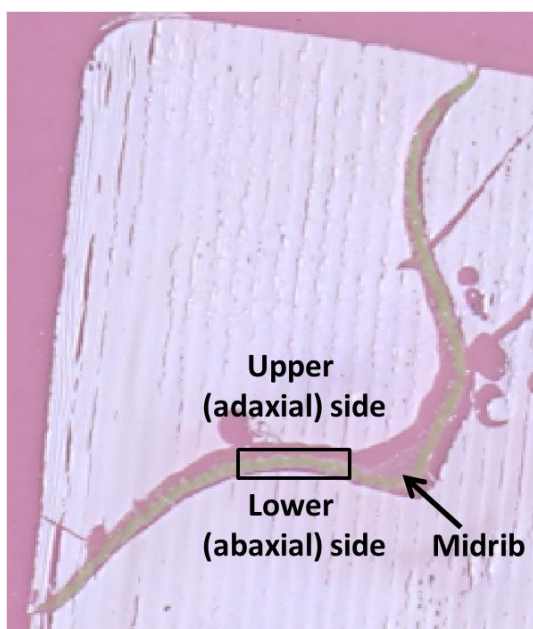
Supplemental Figure 1. Scanned optical image of embedded leaf cross-section. The region within the black box was scanned by MALDI-MSI.
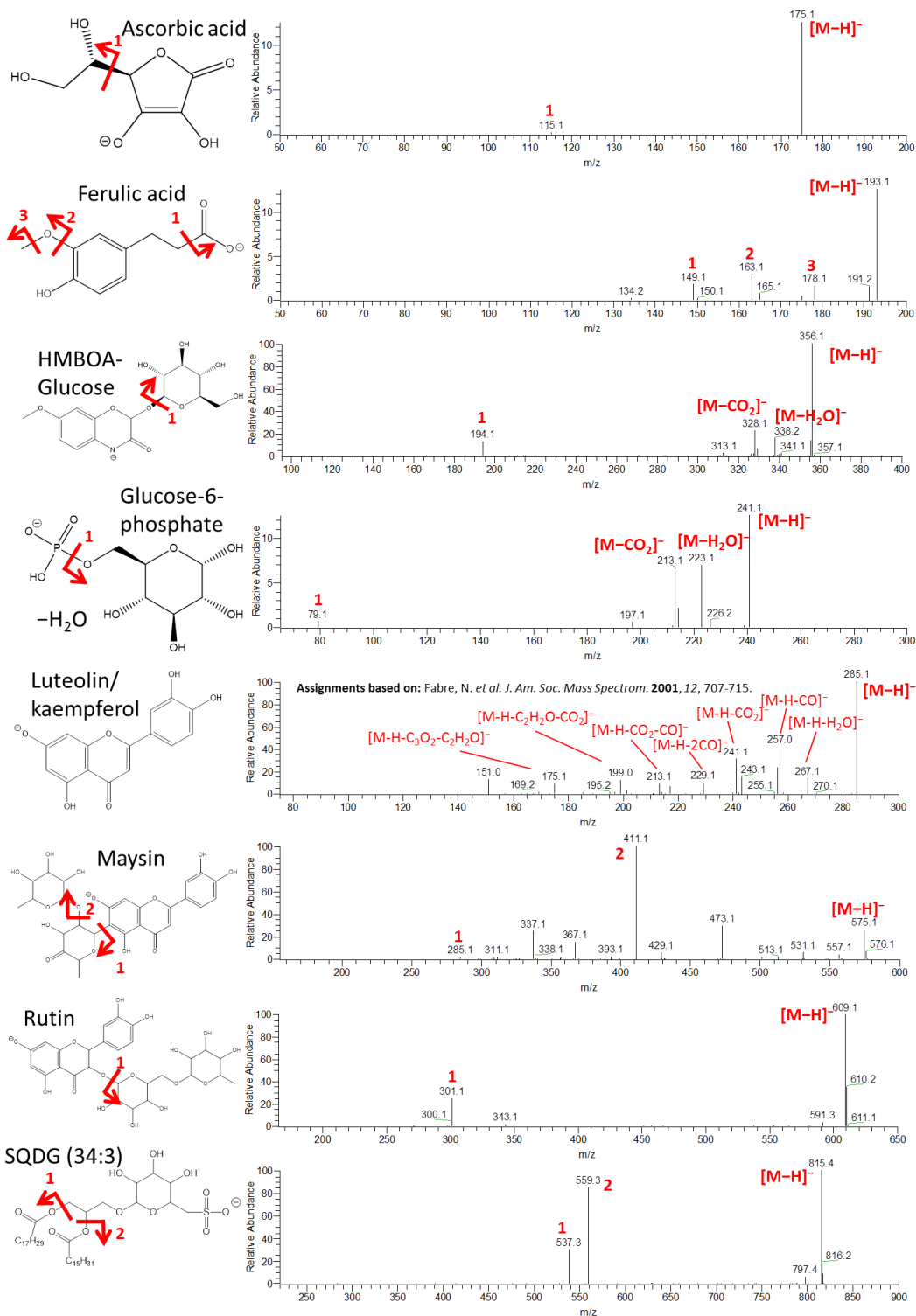
Supplemental Figure 2. MS/MS spectra for several ions images plotted in Figure 3.
Collision energies were individually optimized for each analyte. Assignments for
luteolin/kaempferol are based on Fabre et al[100]. The structure displayed for the *m/z* 285
signal is that for luteolin.

CHAPTER 6

SUMMARY AND OUTLOOK

Summary

The work outlined in this dissertation has sought to expand the utility of MALDI-MSI, especially in regards to its applications for the analysis of metabolites from plant tissues. MALDI-MSI was demonstrated as a tool for functional genomics via the mapping of flavonoid metabolites in wild-type and mutant *Arabidopsis* flowers. A matrix previously used only for lipid analysis (1,5-diaminonaphthalene) was demonstrated to be useful for analysis of small-molecule plant metabolites, both in standard mixtures and for tissue imaging. An instrumental methodology was demonstrated to significantly expand the amount of information that can be obtained from a single MALDI-MSI experiment, incorporating high-mass resolution and tandem MS scans in both polarities into a single acquisition. Finally, a commercial MALDI source has been modified to facilitate high-spatial resolution (~5 μm) imaging, allowing for the generation of metabolite images at a subcellular level as demonstrated on corn leaf cross-sections.

Outlook

In spite of the significant and accelerating progress made in the development of MALDI-MSI as a biological analysis technique, it remains in its infancy. Emerging technologies such as 3-dimensional MSI for the reconstruction of metabolite distributions in

intact tissue samples[106] and ambient sampling imaging (which offers the possibility of sampling intact, living tissues)[107] offer intriguing possibilities for future applications to exploration of plant metabolism.

In addition to new applications, the methodologies and instrument modification presented in this dissertation offers several opportunities for extension or refinement. Experiments of the type presented in Chapter 3, in which the efficiency of different matrices in ionizing different metabolite classes is compared, are highly desirable to improve the sensitivity of MALDI-MSI and expand the range of detectable compounds. Experiments of this type are currently underway on a much larger scale within our research group.

The polarity-switching technique presented in Chapter 4 is, as mentioned, complicated by the use of a single power supply. Further modification of this instrument platform to incorporate a second power supply would allow for much faster acquisition and remove the need for post-acquisition recalibration. Additionally, the incorporation of data-dependent MS/MS scans, mentioned briefly in the chapter, aids in the confident identification of imaged metabolites. Preliminary experiments (not discussed in this work) have shown the utility of this type of imaging experiment, and ongoing work in our laboratory is incorporating similar methods. While full optimization of the method would require modification of both acquisition software and instrument hardware, it offers the possibility of acquiring high-mass resolution MS scans and MS/MS or MS^n scans for many detected compounds, in a single experiment, while adding minimal time to the acquisition.

Further refinement of the optical setup described in Chapter 5 is possible and likely to be completed in the future. Specifically, the adjustment of the laser focus, currently

performed by manual translation of the collimating lens, will be made more reproducible and systematic by incorporation of a micrometer-driven lens mount, and a series of set-points will be defined corresponding to various spot sizes on various sample surfaces. The ideal solution to this issue, automated translation of the final focal lens without venting of the system, may eventually be attempted. This would eliminate the delay introduced by the pumping and bakeout time, but would also require significant modification of the ion source to incorporate an automated translation mount into the vacuum chamber.

The objective of this work has been to develop MALDI-MSI into a more useful technique for the analysis of plant metabolites. As demonstrated by the above examples, significant work remains to be done in the development of MALDI-MSI as a bioanalytical technique, even within the relatively narrow context of this dissertation. Nonetheless, the methods and instrumentation developed and the applications demonstrated herein represent advances that should prove useful in future efforts to answer important biological questions and develop a more complete understanding of plant metabolism.

APPENDIX

MULTIPLEX MALDI-MS IMAGING OF PLANT METABOLITES USING A HYBRID MS SYSTEM

Andrew R. Korte, Gargey B. Yagnik, Adam D. Feenstra, and Young Jin Lee

Abstract

Plant tissues present intriguing systems for study by mass spectrometry imaging, as they exhibit a complex metabolism and a high degree of spatial localization. This chapter presents a methodology for preparation of plant tissue sections for matrix-assisted laser desorption/ionization mass spectrometry imaging (MALDI-MSI) analysis and the use of a hybrid mass spectrometer for 'multiplex' imaging. The multiplex method described here provides a wide range of analytical information, including high-resolution, accurate mass imaging and tandem MS scans for structural information, all within a single experiment. While this procedure was developed for plant tissues, it can be readily adapted for analysis of other sample types.

1. Introduction

Matrix-assisted laser desorption/ionization-mass spectrometry imaging (MALDI-MSI) has been extensively utilized for analysis of animal and human tissues, but it is also a promising technique for analysis of plant metabolites[10, 30]. Plant metabolism is complex; the number of unique metabolites in the plant kingdom has been estimated as high as 200,000[26]. It is also highly localized, with many specialized structures and tissues and significant variation in metabolic profiles - even between, for example, the organs of a flower[27]. MALDI-MSI, with its ability to provide rich chemical information in high spatial resolution, is beginning to be applied to plant systems for metabolite analysis. Efforts so far include mapping of lipids in cottonseeds[108] and on plant surfaces[19, 109], sugars in wheat seeds[110], cellulosic carbohydrates in wood[22], and secondary metabolites in flower petals[23]. Plant applications for MS imaging using other ionization techniques have also been reported, such as laser ablation electrospray ionization[24] and desorption electrospray ionization[25].

The development of hybrid mass spectrometers, which incorporate more than one type of mass analyzer into a single instrument, has significantly expanded the capabilities of mass spectrometry for metabolomic analysis. Existing mass analyzers generally compromise one or more of the following: scan speed, mass resolution, and ability for tandem MS scans[10]. Combining two complementary mass analyzers into a single analytical platform helps to overcome some of these limitations. One example of this kind of instrumentation is a linear ion trap-orbitrap, which incorporates a linear ion trap for high scan rates and MS^n scans, and an orbitrap analyzer for high mass resolution and accurate

mass measurements. Using this instrumentation, we developed a 'multiplex' MS imaging technique to perform high mass resolution imaging, MS/MS and/or MS^n imaging, and data-dependent tandem MS scans on a single tissue section within a single experiment[23, 111]. This method yields a wealth of analytically-useful information, such as accurate mass measurements for assignment of molecular formulas, spatial discrimination of structural isomers, and structurally-informative MS/MS spectra. While our method has been developed for a linear ion trap-orbitrap mass spectrometer, the procedure could be adapted for other tandem MS-capable systems.

Here we describe a sample preparation method for MSI, developed to maintain high spatial localization of plant metabolites down to the single-cell (~10 μm) level. We also present an instrumental methodology for multiplex MS imaging, to obtain rich chemical information in a single imaging experiment. Figure 1 illustrates the overall procedure from tissue harvest to data analysis with each corresponding section number. The reader can refer to specific sections of their interest. Figure 2 illustrates an example of the protocol introduced in this chapter applied to a germinating corn seed.

2. Materials

2.1 Tissue cryosectioning

1. Cryomicrotome: A cryomicrotome consists of a microtome inside a cryostat, allowing for the cutting of thin sections of frozen tissue. Pre-cool the cryostat to the appropriate temperature, e.g. -20°C, and keep microscope slides and adhesive tape sections inside the cryostat.

2. High purity water: Nanopure or LC-MS grade water is recommended to minimize any mass spectrometry contamination.

3. Warm gelatin solution: Prepare a 10% w/v solution (e.g. 1 g in 10 mL) of 300 bloom gelatin in water by heating the water to ~75°C, then adding the gelatin and stirring manually until dissolved.

4. Cryomold: This should be large enough to contain tissue sample and gelatin embedding medium

5. Liquid nitrogen in a dewar. Pour into a Styrofoam box just before flash-freezing tissue or cryomold.

6. 70% ethanol solution, prepared from LC-MS grade ethanol and water

7. Cryo-Jane® adhesive tape sections (Leica Biosystems, Buffalo Grove, IL, USA; *see* **Note 1**)

8. Optimal Cutting Temperature (OCT) Compound

9. Glass microscope slides: These slides are to carry and store tissue sections.

10. Styrofoam cooler with dry ice

2.2 Direct attachment of intact tissues

1. Double-sided tape

2. Sample handling tools (e.g. forceps)

3. Tank of compressed nitrogen

2.3 Sample drying

1. Roll of adhesive tape (e.g. electrical tape): To attach the tissue sections to a heat sink.

2. Vacuum chamber or lyophilizer with vacuum system capable of mtorr pressures.

3. Heat sink (e.g. metal block; *see* **Note 2**): Pre-cool the heat sink in a -80°C freezer for several hours.

2.4 Matrix application by sublimation

1. Sublimation apparatus assembly: A sublimation apparatus with a flat condenser bottom, a cold trap (*see* **Note 3**), a pressure gauge, and a rotary vacuum pump (See the supplemental information of [112] for a detailed schematic of a comparable setup).

2. Glass microscope slide (optional): To attach the tissue slice to a smaller size sublimation device. Cut into half with glass scorer. Mounting Cryo-Jane tape windows with tissue sections to a glass slide makes handling and removing the sample easier.

3. Heating assembly: Temperature-controllable heating mantle and controller. The mantle should be pre-heated to the intended temperature.

4. Roll of adhesive tape

5. Crushed dry ice

6. Acetone (any grade)

7. Appropriate MALDI matrix (*see* **Note 4**)

2.5 Matrix application by oscillating capillary nebulizer

1. Matrix solution/suspension (*see* **Note 5**)

2. 500 µL syringe. Rinse the syringe with the same solvent used for matrix.

3. Syringe pump

4. Oscillating capillary nebulizer (OCN): A hand-held airbrush or other commercial nebulizer can also be used if the matrix homogeneity is not a concern. We use an OCN to ensure homogeneous matrix application (≤ ~10 µm). One can make such a device by simple modification of a commercial airbrush (Aztek A470; Testor, Rockford, IL) (Figure 2 and *see* **Note 6**). Rinse the capillary with the same solvent used for matrix.

5. Tank of compressed nitrogen

3. Methods

3.1 Tissue sectioning

This section is intended for imaging of internal metabolites with minimal analyte loss or re-distribution.

1. Harvest the tissue from the plant, and flash-freeze it as quickly as possible by submerging it into liquid nitrogen. Keep the frozen tissue in a cooler with dry ice while transporting it to the cryostat.

2. Place the frozen tissue into the pre-cooled cryostat for approximately 30 min to allow it to warm to the temperature of the cryostat.

3. Place the frozen tissue into the mold, making sure to orient the tissue so as to section in the desired plane. Pour the warm gelatin solution around the tissue to fill the mold.

4. Float the mold on liquid nitrogen until the gelatin is almost completely frozen to the center (~10-20 s), then transfer the mold into the cryostat (*see* **Note 7**). Once the gelatin is completely frozen (*see* **Note 8**), let it stay in the cryostat for an additional 30 min to ensure the tissue block has equilibrated to the temperature of the cryostat.

5. Remove the tissue block from the mold by cutting the sides of the mold with a razor blade and carefully peeling away the plastic of the cryomold.

6. Place a small amount (<0.5 mL) of OCT compound on the cryotome sample stage and immediately press the tissue block onto it. Allow the OCT to set and fix the tissue block to the stage (*see* **Note 9**).

7. Before installing the cryomicrotome blade, rinse it several times with 70% ethanol to remove any oil or other contaminants that may be transferred to the tissue during sectioning.

8. Run off several sections to provide a flat sample surface and reach the desired portion of the embedded tissue. Set the tissue thickness to the desired value (e.g. 10-20 μm).

9. Remove the protective strip from the Cryo-Jane tape and stick the tape window to the tissue surface (*see* **Note 10**). Using a roller or similar tool, carefully press the tape against the tissue section for uniform adhesion.

10. Slice the section using the cryomicrotome.

11. Keeping it deep inside the cryostat, collect the tape with attached section and inspect it for any potential damage during cutting. If the sample is damaged, discard it and repeat steps 9 and 10.

12. Place the tape window with section attached face-up on a chilled glass slide, and attach it by taping both ends to the slide. Ensure the tape window is flat against the slide (*see* **Note 11**). Avoid prolonged contact with either the tape or slide to prevent thawing of the sample.

13. Remove the slide, with the tape and section attached, from the cryostat and quickly transfer them into a covered cooler full of dry ice (*see* **Note 12**).

14. Repeat steps 9-13 until the desired number of sections has been collected.

15. Optionally, some sections may be taken using traditional thaw-mounting for imaging with optical microscopy, with possible fixation and/or staining.

16. Store tissue sections at -80°C until analysis.

3.2 Direct attachment to sample plate

This section is intended for imaging of surface metabolites.

1. Place a strip or several strips of double-sided tape on the MALDI sample plate. Immediately before harvesting samples, remove the tape backing.

2. Harvest the plant tissue and lay it on the double-sided tape with the surface to be imaged facing upward. Take care not to damage the tissue sample during handling.

3. Using a gentle stream of nitrogen, flatten any parts of the tissue that are not firmly attached to the double-sided tape.

4. Immediately start the sample drying step (section 3.3) to minimize metabolite turn over.

3.3 Sample drying

This procedure covers warming of cryosections and drying of tissue samples to quench metabolite turnover with minimal metabolite re-distribution before the subsequent matrix application and MS imaging procedures.

1. Place the glass slides with the Cryo-Jane tape and tissue sections onto the cooled heat sink and immediately place into a vacuum chamber. For directly-attached samples, the heat sink is not necessary and samples can simply be dried under vacuum at room temperature.

2. Evacuate the chamber. Monitor the samples to ensure no condensation occurs on the sample surface during the thaw-vacuum dry process (*see* **Note 13**).

3. After samples are dried and the heat sink is warmed sufficiently that water will not condense onto the sample when exposed to atmosphere (*see* **Note 2**), release the vacuum and remove the samples.

3.4 Matrix application by sublimation

This procedure allows for homogenous application of organic matrices, especially those that do not give homogeneous coatings by traditional methods. For instance, 2,5-dihydroxybenzoic acid, the most commonly used matrix for MS imaging, is well known to form microcrystals of hundred micron size when spotted or sprayed. The sublimation procedure is modified from one described by Hankin and coworkers [69].

1. Attach the glass slide with the Cryo-Jane tape and tissue section to the bottom of the sublimation condenser using adhesive tape. If a smaller size sublimation apparatus is used, the Cryo-Jane tape with the attached tissue section should be transferred from the original glass slide to an appropriately-sized glass slide first.

2. Evenly distribute ~300 mg of matrix over the bottom surface of the bottom flask of the sublimation apparatus and assemble the apparatus. The tissue section should be facing downward directly over the matrix on the bottom of the flask.

3. Evacuate the sublimation apparatus to <100 mtorr. Once vacuum is reached, add crushed dry ice and ~10-20 mL of acetone to the condenser reservoir to form a slurry and cool the tissue sample (*see* **Note 14**).

4. After 2-3 minutes of cooling, place the sublimation apparatus into the pre-heated mantle to initiate sublimation.

5. After the desired amount of matrix has been deposited, remove the sublimation apparatus from the heating mantle (*see* **Note 15**). Carefully half-fill the condenser reservoir with room-temperature water and wait 2-3 minutes for the sample to return to room temperature.

6. Disassemble the sublimation apparatus and pour the water from the condenser reservoir, taking care to avoid splashing water onto the sample.

7. Remove the glass slide and sample from the bottom of the condenser, then remove the Cryo-Jane tape from the glass slide and attach it to the MALDI sample plate using adhesive tape (*see* **Note 16**).

3.5 Matrix application by oscillating capillary nebulizer (OCN)

This procedure allows homogeneous application of inorganic matrices that cannot be sublimated.

1. Remove the Cryo-Jane tape with tissue sections from the glass slides and attach them to a MALDI sample plate using adhesive tape. Alternatively, the glass slide with tissue section can be directly used in some MALDI mass spectrometers (*see* **Note 1**).

2. Fill the syringe with the matrix solution/suspension.

3. Place a blank stainless steel plate 8-10 cm below the tip of the OCN. This will coat an area approximately 1-2 cm in diameter.

4. Adjust the nebulizing gas pressure to ~40 psi and start the gas flow.

5. Set the flow rate of the syringe pump at 50 µL/min.

6. Start the flow and monitor the blank stainless steel surface to ensure matrix is being applied and wetting is minimal. Depending on matrix solution composition, it may be necessary to stop occasionally for complete drying (e.g. 10 s for every 5 s of spraying). Adjust the interval of application, flow rate, and stop time if necessary.

7. Stop the matrix flow and place the tissue slide below the tip of the OCN, and repeat step 6 to apply the matrix to the tissue. For larger samples, the sample can be moved underneath the spray (*see* **Note 17**).

8. When a suitable amount of matrix is deposited (*see* **Note 5**), stop the syringe pump and remove the sample slide from below the OCN.

3.6 Multiplex MS imaging

Please refer to the instrument guideline or manual for the operational details of MS imaging. Here, we describe only the basic procedure with a focus on multiplex MS imaging. The procedure described here is intended for LTQ-Orbitrap instruments, but the idea can be generalized to other mass spectrometers.

1. Using either an optical scanner or in-source camera, acquire an optical image of the whole tissue for later reference and co-registration with the MS images.

2. Using the instrument software (Tune Plus), optimize instrumental parameters for the studied tissue. This may include laser energy per pulse, number of laser shots, ion optical tuning parameters, etc (*see* **Note 18**). Save the tune file that contains this information.

3. Decide the type of multiplex MS imaging experiment that will be performed. Figure 3 offers two examples that we have previously reported [23, 111]. The diagrams illustrate the spiral pattern on each raster step and the tables show the corresponding MS event for each spiral step, as defined in the method file (*See* **Note 19**). Polarity switching can also be integrated to acquire MS and MS/MS spectra in

both positive and negative ion mode, as we have previously demonstrated [113]. It is also possible to incorporate data-dependent MS/MS or MS^n scans, with peaks for tandem MS analysis being chosen 'on-the-fly' based on an MS spectrum for each raster pixel.

4. In the MALDI window of Tune Plus, select the tissue region to be imaged. Define the number of spiral steps, which should be the same as the number of MS scan events of the desired raster design; e.g. 4 and 9 for the raster design of A and B in Figure 3, respectively. Define the raster step size and spiral step size. Make sure the spiral step size is bigger than the laser spot size (*see* **Note 20**) and the raster step size is at least twice the spiral step size for design A and four times the spiral step size for design B (*see* **Note 21**). Save all this information as a MALDI Position file.

5. Set up a new instrument method using the Xcalibur software. Individually define parameters for each scan event, such as the mass analyzer and MS^n settings, to match your raster design. Additional information is needed including mass range, desired resolution, polarity, and MS/MS conditions (*see* **Notes 22 and 23**). Save the instrument method file.

6. In the Sequence Set-up window of Xcalibur, provide a data file name to be used, destination folder for data, instrument method, and MALDI position file name.

7. (Optional) If multiple runs will be performed, repeat steps 3-6. Step 3 can be skipped if the same multiplex imaging method will be used for the other imaging runs.

8. In the sequence window, select the samples to be analyzed and submit. Make sure the submitted samples show up in the acquisition queue. Plate movement and laser firing should be visible on the in-source camera, and acquisition of spectra should be seen in the Tune window or the real time view of Xcalibur.

4. Notes

1. MALDI-ion trap mass spectrometers (with or without Orbitrap) generally require a relatively low voltage to extract ions from the MALDI source (e.g. ± 20V) and accumulate a negligible surface charge during the MALDI process. In addition, subsequent ion trap or Orbitrap mass measurement is independent of initial kinetic energy and is not affected by minor electric field distortions on the MALDI plate surface. Accordingly, one can use non-conductive materials, including non-conductive adhesive tape and glass sample slides. For other instrumentation, especially time-of-flight (TOF) mass analyzers, this effect could be detrimental and one should use only conductive tape and plates.

2. The block should be large enough to keep attached tissues cold during the vacuum-drying process. We found an ~200 g (approx. 18 cm x 6 cm x 0.65cm) aluminum block is sufficient for 10-20 μm cryosections. Using this setup, the freeze-drying process takes ~90 min before samples are dried and sufficiently warmed to be removed from the vacuum.

3. The cold trap is submerged in a dry ice/acetone slurry and reduces contamination of the vacuum pump by matrix. It also minimizes backflow of vacuum pump oil to the sample.

4. The choice of matrix is critical in MALDI-MS imaging experiments, especially for small metabolite analysis. Because of the wide chemical functionality of various metabolites, the matrix should be carefully chosen based on the analytes of interest. Matrix choice is discussed in [10].

5. Matrix concentrations and volumes should be optimized depending on the matrix and application area. We use 0.6 mL for 20 ppm colloidal silver suspension and 0.3 mL for colloidal graphite aerosol spray (Alfa Aesar, Ward Hill, MA), after dilution with 2-propanol four times and eight times, respectively.

6. The design and performance of an OCN is described in detail in Chen et al [53]. A methodology for using an OCN for matrix application has also been published in this series [114]. We have created an OCN by modification of a commercial airbrush (Aztek A470; Testor, Rockford, IL). This modification is shown in Figure 4. The inner spraying tip and trigger mechanism has been replaced by plastic tubing (0.0625" i.d. x 0.02" o.d.) with a fused silica capillary running through it (100 μm i.d. x 360 μm o.d.). Nitrogen is supplied as a nebulizing gas through the airbrush gas interface and matrix solution is supplied through the capillary by a syringe pump. The capillary can be easily replaced when switching matrix solutions to avoid cross-contamination.

7. Letting the gelatin completely freeze on liquid nitrogen can cause the tissue block to crack. Transferring to the cryostat right before the block is completely frozen can minimize this.

8. The gelatin should be opaque when completely frozen.

9. OCT can cause significant interference and suppression of analyte signals during MS analysis. Care should be taken to minimize the amount of OCT used to fix the tissue block, and to avoid squeezing the OCT over the sides of the sample.

10. Typical tissue sectioning for optical imaging uses thaw mounting by directly attaching a frozen tissue slice to a room temperature glass slide. However, this may cause redistribution of water-soluble small molecules, which could be problematic for high-resolution MS imaging. We use adhesive Cryo-Jane tape followed by vacuum-drying to minimize this possibility.

11. We use the glass slides to make sections on the Cryo-Jane tape easier to transport and store, and as a heat sink to prevent thawing of the frozen tissue samples during transfer. Sample sections on Cryo-Jane tape thaw very quickly when exposed to ambient temperature.

12. Exposure of the samples to room temperature air should be minimized. This both reduces the chances of sample thawing and prevents large amounts of ice condensing on the slide and sample.

13. Loss of some volatile analytes is unavoidable during freeze drying, but these analytes are also likely to be lost in the vacuum or intermediate-vacuum of most MALDI-MS ion sources. We do not recommend going below ~50-100 mtorr, so as not to lose

partially volatile compounds that are amenable for analysis in an intermediate pressure MALDI source. Vacuum drying should be performed even for atmospheric pressure MALDI-MS to quench metabolic turnover before matrix application and MS data acquisition.

14. Only a minimal amount of dry ice/acetone is needed. Only the bottom surface of the condenser (in contact with the sample) needs to be cooled. Using larger quantities will increase the time needed to re-warm the sample after sublimation.

15. After sublimation, a thin, even layer of matrix should be observable. If the matrix layer is completely opaque, the deposited layer is likely too thick. Thomas et al. found ~50-200 μg/cm^2 to be the optimal matrix density for analyte detection [65].

16. Ensure the tape window with attached sample is flat against the MALDI plate. Variations in sample height will cause differences in laser fluence at the sample surface and possible signal deviation or spectral differences.

17. This method is best suited for spraying small tissue samples (<1 cm^2). For larger samples, the motion of the tissue under the OCN should be automated to ensure an even coating, and the sprayed matrix volume should be adjusted accordingly.

18. These parameters are specific to the tissue sample, instrument, and matrix used, and it is very helpful to test and tune them on a section of dummy tissue that was processed in parallel. As a guideline, we generally use a laser energy of 1-10 μJ per pulse at 60 Hz, 10 shots per scan, and no sweep shots.

19. The 'spiral step' function in Tune Plus is originally intended to average several spectra over a single pixel, incorporating several smaller steps into each raster step.

We define the number of spiral steps and number of MS scans such that each spiral step correlates to a given MS scan type.

20. Laser spot size can be estimated by rastering over a thin matrix layer prepared by spotting α-cyano-4-hydroxycinnamic acid in acetone on a MALDI plate, with the raster size at least twice the expected laser spot size.

21. This pattern requires additional space equal to the size of one spiral raster step between each raster pattern. This preserves the spacing between ion trap MS scans and provides twice the spatial resolution of other scans in the pattern for imaging. Note that home-made software is required for generating images from IT scans, as ImageQuest does not process individual spiral steps as separate pixels.

22. For high resolution analyzers, it is often desirable to collect data in a centroid or binned mode. Imaging of large tissues or at high spatial resolutions generates very large size data files (e.g. >1 GB) if full profile scans are collected.

23. For semi-targeted analysis, a list of parent m/z values can be used to acquire MS/MS or MS^n spectra for compounds known or suspected to be present in the tissue. Scans can also be acquired simply for the highest-intensity peaks. It is helpful to incorporate a dynamic exclusion function, which prevents repeated acquisition of spectra for the most abundant ions and maximizes the number of ions for which tandem MS scans are performed. However, we have observed that if no peaks are selected for MS/MS in a data-dependent scan, the software will skip the scan without skipping the position. This can lead to acquisition of multiple Orbitrap scans within a single spiral pattern. Although this is generally not detrimental to imaging

(multiple identical scans within a spiral pattern are simply averaged during image generation and this problem rarely occurs), it can increase data acquisition time.

Acknowledgments

Figures
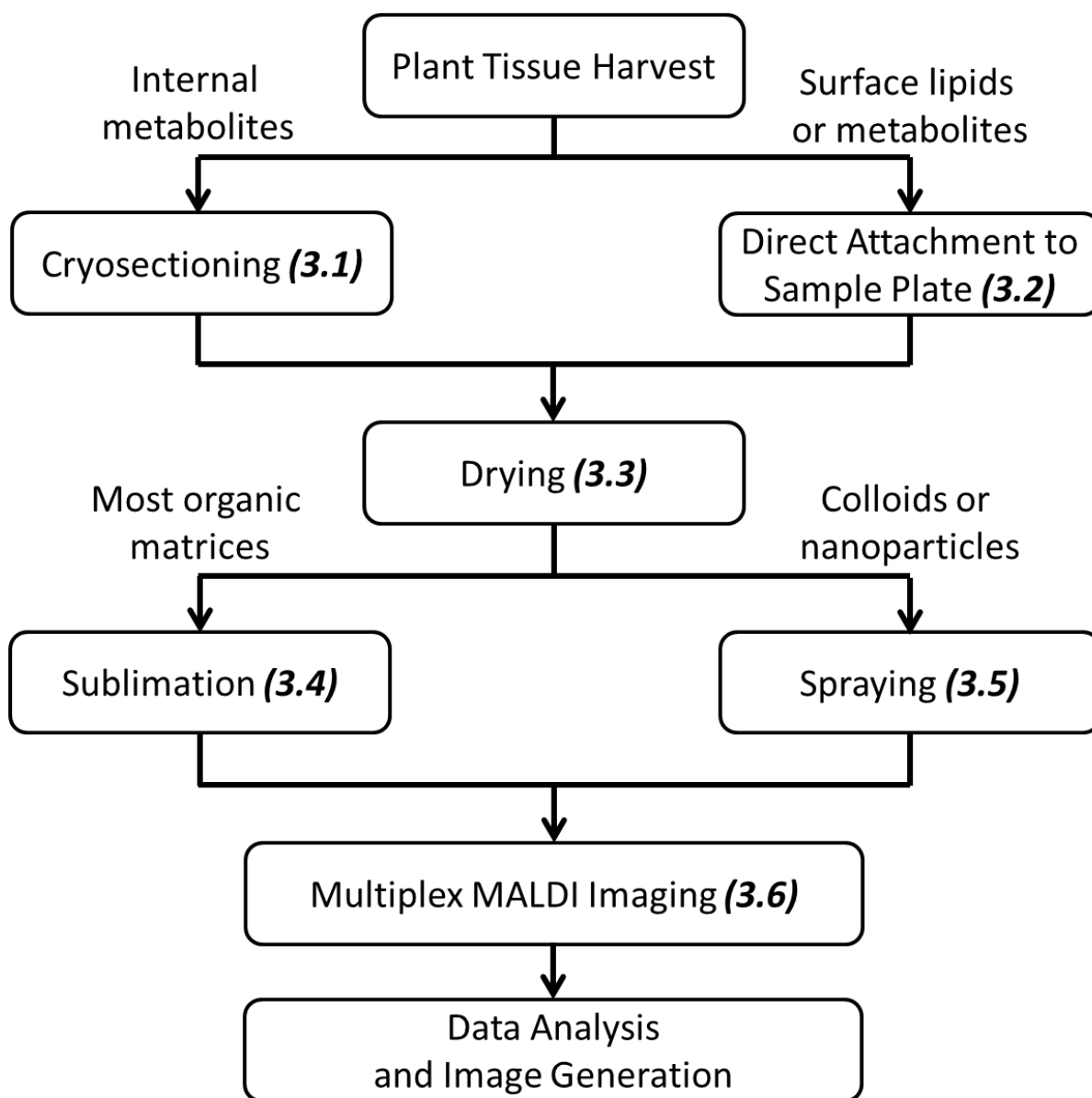
Fig. 1. Workflow for multiplex MALDI-MS imaging of plant metabolites. Procedures discussed in this work are labeled with the corresponding section number.
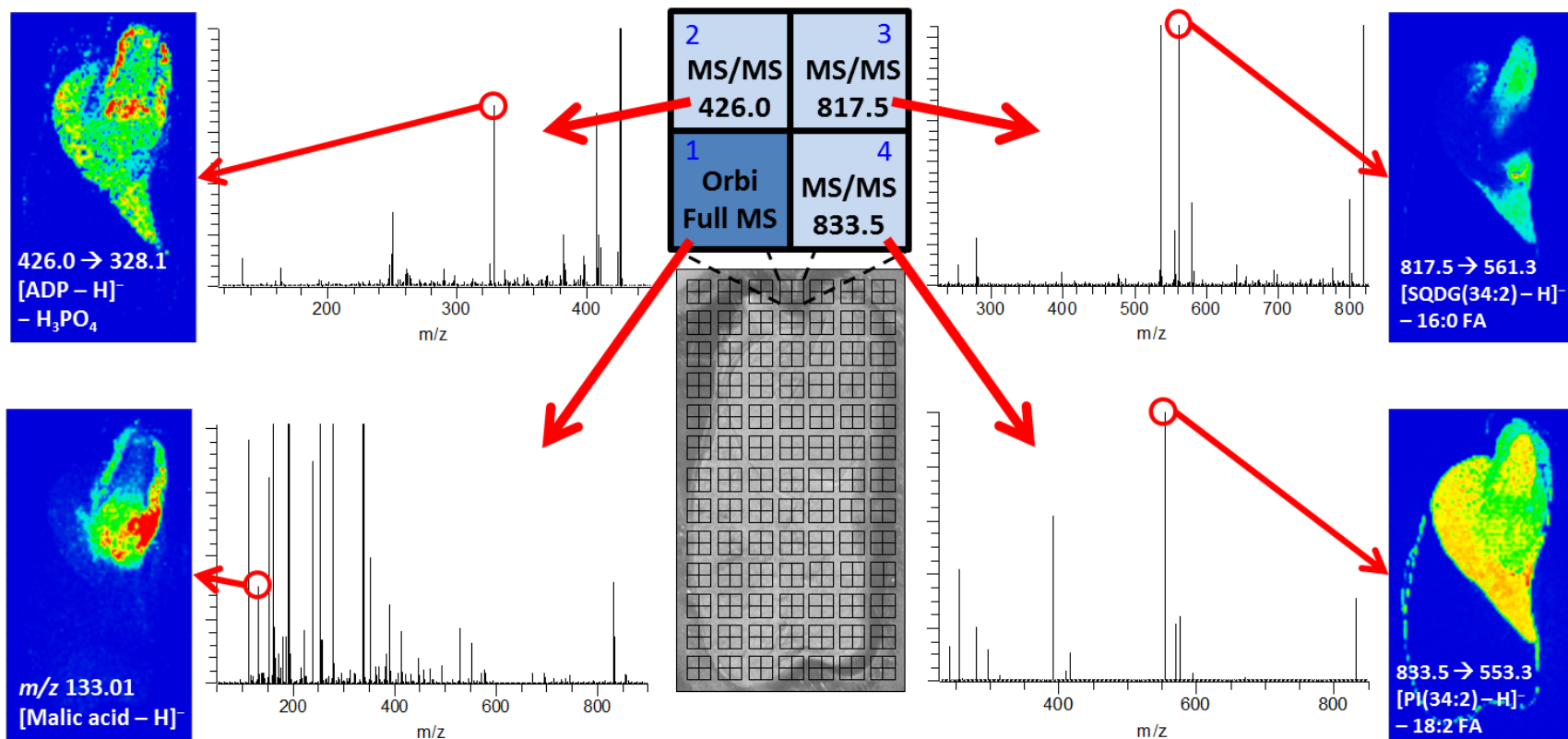
Fig. 2. Illustration of the protocol applied to a germinating corn seed. A corn seed was germinated in water for 3 days in a green house, cryosectioned (section 3.1), freeze-dried (section 3.3), and sublimated with 9-aminoacridine matrix (section 3.4), before a four step multiplex MS imaging experiment was performed (raster design A in Figure 3). ADP, SQDG, and PI represent adenosine diphosphate, sulfoquinovosyl diacylglycerol, and phosphatidylinositol, respectively. Peaks used to generate images are circled.

Raster Design

MS Scan Event

A)

| 2 IT MS² m₁ | 3 IT MS² m₂ |
| 1 FTMS | 4 IT MS² m₃ |

Raster A:
- Cell 2: IT MS² m₁
- Cell 3: IT MS² m₂
- Cell 1: FTMS
- Cell 4: IT MS² m₃

Scan event #	Analyzer	MSⁿ Setting
1	FTMS	–
2	ITMS	MS² of m_1
3	ITMS	MS² of m_2
4	ITMS	MS² of m_3

B)

Raster B:
- Cell 9: IT MS
- Cell 2: IT MS² m₁
- Cell 3: IT MS
- Cell 8: IT MS³ m₂>m₄
- Cell 1: FTMS
- Cell 4: IT MS² m₂
- Cell 7: IT MS
- Cell 6: IT MS³ m₁>m₃
- Cell 5: IT MS

Scan event #	Analyzer	MSⁿ Setting
1	FTMS	–
2	ITMS	MS² of m_1
3	ITMS	–
4	ITMS	MS² of m_2
5	ITMS	–
6	ITMS	MS² of m_1 MS³ of m_3
7	ITMS	–
8	ITMS	MS² of m_2 MS³ of m_4
9	ITMS	–

Fig. 3. Example spiral patterns for each raster step and corresponding MS or MS/MS events for two multiplex imaging experiments. Pattern **A** shows an experiment that acquires one high mass resolution orbitrap spectrum (step #1) and MS/MS spectra for three ions (steps #2-4) at each pixel. Pattern **B** shows an experiment that acquires one high mass resolution orbitrap spectrum (step #1), four moderate mass resolution but high scan speed ion trap MS spectrum (steps #3, 5, 7, and 9), MS/MS spectra for two ions (steps 2 and 4), and MS³ spectra for two fragments of those ions (steps 6 and 8). FT and IT denote orbitrap and ion trap mass analyzer, respectively.

Unmodified airbrush

Oscillating Capillary Nebulizer

Capillary tip

Matrix solution

N$_2$ gas

Fig. 4. Photograph showing modifications to an Aztek A470 airbrush (Testor, Rockford, IL) to create an oscillating capillary nebulizer. The trigger mechanism has been removed and a capillary has been run through the housing and out the spray tip. The capillary is run through plastic tubing (0.0625" o.d. x 0.02" i.d.) and nitrogen gas is supplied using the airbrush gas interface. Matrix solution is delivered through the capillary by means of a syringe pump.

REFERENCES

[1]   K. Dettmer, P. A. Aronov, B. D. Hammock, Mass spectrometry-based metabolomics. *Mass Spectrom. Rev.* **2007**, *26*, 51.

[2]   M. J. Kailemia, L. R. Ruhaak, C. B. Lebrilla, I. J. Amster, Oligosaccharide Analysis by Mass Spectrometry: A Review of Recent Developments. *Anal. Chem.* **2013**, *86*, 196.

[3]   S. J. Blanksby, T. W. Mitchell, Advances in Mass Spectrometry for Lipidomics. *Annual Review of Analytical Chemistry* **2010**, *3*, 433.

[4]   J. D. Chapman, D. R. Goodlett, C. D. Masselon, Multiplexed and data-independent tandem mass spectrometry for global proteome profiling. *Mass Spectrom. Rev.* **2013**, n/a.

[5]   I. Ojanpera, M. Kolmonen, A. Pelander, Current use of high-resolution mass spectrometry in drug screening relevant to clinical and forensic toxicology and doping control. *Analytical and bioanalytical chemistry* **2012**, *403*, 1203.

[6]   E. Dudley, L. Bond, Mass spectrometry analysis of nucleosides and nucleotides. *Mass Spectrom. Rev.* **2014**, *33*, 302.

[7]   E. R. Amstalden van Hove, D. F. Smith, R. M. Heeren, A concise review of mass spectrometry imaging. *J. Chromatogr. A* **2010**, *1217*, 3946.

[8]   E. H. Seeley, R. M. Caprioli, MALDI imaging mass spectrometry of human tissue: method challenges and clinical perspectives. *Trends Biotechnol.* **2011**, *29*, 136.

[9]   K. A. Berry, J. A. Hankin, R. M. Barkley, J. M. Spraggins, R. M. Caprioli, R. C. Murphy, MALDI imaging of lipid biochemistry in tissues by mass spectrometry. *Chem. Rev.* **2011**, *111*, 6491.

[10]   Y. J. Lee, D. C. Perdian, Z. Song, E. S. Yeung, B. J. Nikolau, Use of mass spectrometry for imaging metabolites in plants. *Plant J.* **2012**, *70*, 81.

[11]   D. Gode, D. A. Volmer, Lipid imaging by mass spectrometry - a review. *The Analyst* **2013**, *138*, 1289.

[12]   S. Nimesh, S. Mohottalage, R. Vincent, P. Kumarathasan, Current Status and Future Perspectives of Mass Spectrometry Imaging. *International Journal of Molecular Sciences* **2013**, *14*, 11277.

[13]   T. W. Jaskolla, M. Karas, Compelling evidence for Lucky Survivor and gas phase protonation: the unified MALDI analyte protonation mechanism. *J. Am. Soc. Mass. Spectrom.* **2011**, *22*, 976.

[14]   N. Bjarnholt, B. Li, J. D'Alvise, C. Janfelt, Mass spectrometry imaging of plant metabolites - principles and possibilities. *Natural Product Reports* **2014**, *31*, 818.

[15]   S. L. Luxembourg, T. H. Mize, L. A. McDonnell, R. M. A. Heeren, High-Spatial Resolution Mass Spectrometric Imaging of Peptide and Protein Distributions on a Surface. *Anal. Chem.* **2004**, *76*, 5339.

[16]   R. M. Caprioli, T. B. Farmer, J. Gile, Molecular Imaging of Biological Samples: Localization of Peptides and Proteins Using MALDI-TOF MS. *Anal. Chem.* **1997**, *69*, 4751.

[17]   F. Hillenkamp, J. Peter-Katalinic, *MALDI MS: A Practical Guide to Instrumentation, Methods and Applications*, Wiley, **2013**, pp. 139.

[18]   P. J. Horn, A. R. Korte, P. B. Neogi, E. Love, J. Fuchs, K. Strupat, L. Borisjuk, V. Shulaev, Y.-J. Lee, K. D. Chapman, Spatial Mapping of Lipids at Cellular Resolution in Embryos of Cotton. *The Plant Cell Online* **2012**, *24*, 622.

[19]   S. Cha, Z. Song, B. J. Nikolau, E. S. Yeung, Direct profiling and imaging of epicuticular waxes on Arabidopsis thaliana by laser desorption/ionization mass spectrometry using silver colloid as a matrix. *Anal. Chem.* **2009**, *81*, 2991.

[20]   J. H. Jun, Z. Song, Z. Liu, B. J. Nikolau, E. S. Yeung, Y. J. Lee, High-spatial and high-mass resolution imaging of surface metabolites of Arabidopsis thaliana by laser desorption-ionization mass spectrometry using colloidal silver. *Anal. Chem.* **2010**, *82*, 3255.

[21]   M. Burrell, C. Earnshaw, M. Clench, Imaging Matrix Assisted Laser Desorption Ionization Mass Spectrometry: a technique to map plant metabolites within tissues at high spatial resolution. *J. Exp. Bot.* **2007**, *58*, 757.

[22]   K. A. Lunsford, G. F. Peter, R. A. Yost, Direct Matrix-Assisted Laser Desorption/Ionization Mass Spectrometric Imaging of Cellulose and Hemicellulose in Populus Tissue. *Anal. Chem.* **2011**, *83*, 6722.

[23]   D. C. Perdian, Y. J. Lee, Imaging MS Methodology for More Chemical Information in Less Data Acquisition Time Utilizing a Hybrid Linear Ion Trap−Orbitrap Mass Spectrometer. *Anal. Chem.* **2010**, *82*, 9393.

[24]   B. Shrestha, J. M. Patt, A. Vertes, In Situ Cell-by-Cell Imaging and Analysis of Small Cell Populations by Mass Spectrometry. *Anal. Chem.* **2011**, *83*, 2947.

[25]   B. Li, N. Bjarnholt, S. H. Hansen, C. Janfelt, Characterization of barley leaf tissue using direct and indirect desorption electrospray ionization imaging mass spectrometry. *J. Mass Spectrom.* **2011**, *46*, 1241.

[26] O. Fiehn, Metabolomics--the link between genotypes and phenotypes. *Plant molecular biology* **2002**, *48*, 155.

[27] K. Hanhineva, I. Rogachev, H. Kokko, S. Mintz-Oron, I. Venger, S. Karenlampi, A. Aharoni, Non-targeted analysis of spatial metabolite composition in strawberry (Fragariaxananassa) flowers. *Phytochem.* **2008**, *69*, 2463.

[28] M. Stoeckli, D. Staab, A. Schweitzer, Compound and metabolite distribution measured by MALDI mass spectrometric imaging in whole-body tissue sections. *Int. J. Mass Spectrom.* **2007**, *260*, 195.

[29] S. Jackson, K. Baldwin, L. Muller, V. Womack, J. A. Schultz, C. Balaban, A. Woods, Imaging of lipids in rat heart by MALDI-MS with silver nanoparticles. *Analytical and bioanalytical chemistry* **2014**, *406*, 1377.

[30] S. Kaspar, M. Peukert, A. Svatos, A. Matros, H.-P. Mock, MALDI-imaging mass spectrometry – An emerging technique in plant biology. *Proteomics* **2011**, *11*, 1840.

[31] P. Sjövall, J. Lausmaa, B. Johansson, Mass Spectrometric Imaging of Lipids in Brain Tissue. *Anal. Chem.* **2004**, *76*, 4271.

[32] D. R. Ifa, J. M. Wiseman, Q. Song, R. G. Cooks, Development of capabilities for imaging mass spectrometry under ambient conditions with desorption electrospray ionization (DESI). *Int. J. Mass Spectrom.* **2007**, *259*, 8.

[33] R. L. Caldwell, R. M. Caprioli, Tissue profiling by mass spectrometry: a review of methodology and applications. *Mol. Cell. Proteomics* **2005**, *4*, 394.

[34] A. Römpp, S. Guenther, Y. Schober, O. Schulz, Z. Takats, W. Kummer, B. Spengler, Histology by Mass Spectrometry: Label-Free Tissue Characterization Obtained from High-Accuracy Bioanalytical Imaging. *Angew. Chem. Int. Ed.* **2010**, *49*, 3834.

[35] M. Veit, G. F. Pauli, Major Flavonoids from Arabidopsis thaliana Leaves†. *J. Nat. Prod.* **1999**, *62*, 1301.

[36] P. Chaurand, S. A. Schwartz, M. L. Reyzer, R. M. Caprioli, Imaging mass spectrometry: principles and potentials. *Toxicol. Pathol.* **2005**, *33*, 92.

[37] T. Hayasaka, N. Goto-Inoue, N. Zaima, Y. Kimura, M. Setou, Organ-Specific Distributions of Lysophosphatidylcholine and Triacylglycerol in Mouse Embryo. *Lipids* **2009**, *44*, 837.

[38] B. Prideaux, V. r. Dartois, D. Staab, D. M. Weiner, A. Goh, L. E. Via, C. E. Barry Iii, M. Stoeckli, High-Sensitivity MALDI-MRM-MS Imaging of Moxifloxacin

Distribution in Tuberculosis-Infected Rabbit Lungs and Granulomatous Lesions. *Anal. Chem.* **2011**, *83*, 2112.

[39]   S. Kang, H. S. Shim, J. S. Lee, D. S. Kim, H. Y. Kim, S. H. Hong, P. S. Kim, J. H. Yoon, N. H. Cho, Molecular proteomics imaging of tumor interfaces by mass spectrometry. *J. Proteome Res.* **2010**, *9*, 1157.

[40]   S. Cha, H. Zhang, H. I. Ilarslan, E. S. Wurtele, L. Brachova, B. J. Nikolau, E. S. Yeung, Direct profiling and imaging of plant metabolites in intact tissues by using colloidal graphite-assisted laser desorption ionization mass spectrometry. *Plant J.* **2008**, *55*, 348.

[41]   D. Hölscher, R. Shroff, K. Knop, M. Gottschaldt, A. Crecelius, B. Schneider, D. G. Heckel, U. S. Schubert, A. Svatoš, Matrix-free UV-laser desorption/ionization (LDI) mass spectrometric imaging at the single-cell level: distribution of secondary metabolites of Arabidopsis thaliana and Hypericum species. *Plant J.* **2009**, *60*, 907.

[42]   D. M. G. Anderson, V. A. Carolan, S. Crosland, K. R. Sharples, M. R. Clench, Examination of the distribution of nicosulfuron in sunflower plants by matrix-assisted laser desorption/ionisation mass spectrometry imaging. *Rapid Commun. Mass Spectrom.* **2009**, *23*, 1321.

[43]   P. Nemes, A. A. Barton, A. Vertes, Three-Dimensional Imaging of Metabolites in Tissues under Ambient Conditions by Laser Ablation Electrospray Ionization Mass Spectrometry. *Anal. Chem.* **2009**, *81*, 6668.

[44]   C. Somerville, M. Koornneef, A fortunate choice: the history of Arabidopsis as a model plant. *Nat. Rev. Genet.* **2002**, *3*, 883.

[45]   Analysis of the genome sequence of the flowering plant Arabidopsis thaliana. *Nature* **2000**, *408*, 796.

[46]   K. Baerenfaller, J. Grossmann, M. A. Grobei, R. Hull, M. Hirsch-Hoffmann, S. Yalovsky, P. Zimmermann, U. Grossniklaus, W. Gruissem, S. Baginsky, Genome-Scale Proteomics Reveals Arabidopsis thaliana Gene Models and Proteome Dynamics. *Science* **2008**, *320*, 938.

[47]   W. I. Mentzen, J. Peng, N. Ransom, B. J. Nikolau, E. S. Wurtele, Articulation of three core metabolic processes in Arabidopsis: fatty acid biosynthesis, leucine catabolism and starch metabolism. *BMC Plant Biol.* **2008**, *8*, 76.

[48]   W. Mentzen, E. Wurtele, Regulon organization of Arabidopsis. *BMC Plant Biol.* **2008**, *8*, 99.

[49]   R. J. Bino, R. D. Hall, O. Fiehn, J. Kopka, K. Saito, J. Draper, B. J. Nikolau, P. Mendes, U. Roessner-Tunali, M. H. Beale, R. N. Trethewey, B. M. Lange, E. S.

Wurtele, L. W. Sumner, Potential of metabolomics as a functional genomics tool. *Trends Plant Sci.* **2004**, *9*, 418.

[50]   P. Bais, S. M. Moon, K. He, R. Leitao, K. Dreher, T. Walk, Y. Sucaet, L. Barkan, G. Wohlgemuth, M. R. Roth, E. S. Wurtele, P. Dixon, O. Fiehn, B. M. Lange, V. Shulaev, L. W. Sumner, R. Welti, B. J. Nikolau, S. Y. Rhee, J. A. Dickerson, PlantMetabolomics.org: A Web Portal for Plant Metabolomics Experiments. *Plant Physiol.* **2010**, *152*, 1807.

[51]   C. Ringli, L. Bigler, B. M. Kuhn, R.-M. Leiber, A. Diet, D. Santelia, B. Frey, S. Pollmann, M. Klein, The Modified Flavonol Glycosylation Profile in the Arabidopsis rol1 Mutants Results in Alterations in Plant Growth and Cell Shape Formation. *Plant Cell* **2008**, *20*, 1470.

[52]   C. Schoenbohm, S. Martens, C. Eder, G. Forkmann, B. Weisshaar, Identification of the Arabidopsis thaliana flavonoid 3'-hydroxylase gene and functional expression of the encoded P450 enzyme. *Biol. Chem.* **2000**, *381*, 749.

[53]   Y. Chen, J. Allegood, Y. Liu, E. Wang, B. Cachon-Gonzalez, T. M. Cox, A. H. Merrill, Jr., M. C. Sullards, Imaging MALDI mass spectrometry using an oscillating capillary nebulizer matrix coating system and its application to analysis of lipids in brain from a mouse model of Tay-Sachs/Sandhoff disease. *Anal. Chem.* **2008**, *80*, 2780.

[54]   L. Kerhoas, D. Aouak, A. Cingöz, J.-M. Routaboul, L. Lepiniec, J. Einhorn, N. Birlirakis, Structural Characterization of the Major Flavonoid Glycosides from Arabidopsis thaliana Seeds. *J. Agric. Food Chem.* **2006**, *54*, 6603.

[55]   K. Yonekura-Sakakibara, T. Tohge, F. Matsuda, R. Nakabayashi, H. Takayama, R. Niida, A. Watanabe-Takahashi, E. Inoue, K. Saito, Comprehensive Flavonol Profiling and Transcriptome Coexpression Analysis Leading to Decoding Gene–Metabolite Correlations in Arabidopsis. *The Plant Cell Online* **2008**, *20*, 2160.

[56]   J. B. Harborne, C. A. Williams, Advances in flavonoid research since 1992. *Phytochem.* **2000**, *55*, 481.

[57]   R. F. Reich, K. Cudzilo, J. A. Levisky, R. A. Yost, Quantitative MALDI-MSn Analysis of Cocaine in the Autopsied Brain of a Human Cocaine User Employing a Wide Isolation Window and Internal Standards. *J. Am. Soc. Mass. Spectrom.* **2010**, *21*, 564.

[58]   T. R. Northen, O. Yanes, M. T. Northen, D. Marrinucci, W. Uritboonthai, J. Apon, S. L. Golledge, A. Nordstrom, G. Siuzdak, Clathrate nanostructures for mass spectrometry. *Nature* **2007**, *449*, 1033.

[59] B. N. Walker, J. A. Stolee, A. Vertes, Nanophotonic ionization for ultratrace and single-cell analysis by mass spectrometry. *Anal. Chem.* **2012**, *84*, 7756.

[60] K. Shrivas, T. Hayasaka, Y. Sugiura, M. Setou, Method for Simultaneous Imaging of Endogenous Low Molecular Weight Metabolites in Mouse Brain Using TiO2 Nanoparticles in Nanoparticle-Assisted Laser Desorption/Ionization-Imaging Mass Spectrometry. *Anal. Chem.* **2011**, *83*, 7283.

[61] Y. K. Kim, H. K. Na, S. J. Kwack, S. R. Ryoo, Y. Lee, S. Hong, S. Hong, Y. Jeong, D. H. Min, Synergistic effect of graphene oxide/MWCNT films in laser desorption/ionization mass spectrometry of small molecules and tissue imaging. *ACS Nano* **2011**, *5*, 4550.

[62] A. Amantonico, J. Y. Oh, J. Sobek, M. Heinemann, R. Zenobi, Mass spectrometric method for analyzing metabolites in yeast with single cell sensitivity. *Angew. Chem. Int. Ed. Engl.* **2008**, *47*, 5382.

[63] R. Shroff, A. Svatos, Proton sponge: a novel and versatile MALDI matrix for the analysis of metabolites using mass spectrometry. *Anal. Chem.* **2009**, *81*, 7954.

[64] R. Chen, S. Chen, C. Xiong, X. Ding, C. C. Wu, H. C. Chang, S. Xiong, Z. Nie, N-(1-naphthyl) ethylenediamine dinitrate: a new matrix for negative ion MALDI-TOF MS analysis of small molecules. *J. Am. Soc. Mass. Spectrom.* **2012**, *23*, 1454.

[65] A. Thomas, J. L. Charbonneau, E. Fournaise, P. Chaurand, Sublimation of New Matrix Candidates for High Spatial Resolution Imaging Mass Spectrometry of Lipids: Enhanced Information in Both Positive and Negative Polarities after 1,5-Diaminonaphthalene Deposition. *Anal. Chem.* **2012**, *84*, 2048.

[66] K. Demeure, L. Quinton, V. Gabelica, E. De Pauw, Rational selection of the optimum MALDI matrix for top-down proteomics by in-source decay. *Anal. Chem.* **2007**, *79*, 8678.

[67] L. Molin, R. Seraglia, F. R. Dani, G. Moneti, P. Traldi, The double nature of 1,5-diaminonaphthalene as matrix-assisted laser desorption/ionization matrix: some experimental evidence of the protonation and reduction mechanisms. *Rapid Commun. Mass Spectrom.* **2011**, *25*, 3091.

[68] N. A. Hagan, C. A. Smith, M. D. Antoine, J. S. Lin, A. B. Feldman, P. A. Demirev, Enhanced in-source fragmentation in MALDI-TOF-MS of oligonucleotides using 1,5-diaminonapthalene. *J. Am. Soc. Mass. Spectrom.* **2012**, *23*, 773.

[69] J. A. Hankin, R. M. Barkley, R. C. Murphy, Sublimation as a method of matrix application for mass spectrometric imaging. *J. Am. Soc. Mass. Spectrom.* **2007**, *18*, 1646.

[70]   J. E. Stewart, *Optical Principles and Technology for Engineers*, Marcel Dekker, Inc., New York, New York, **1996**, pp. 149-150.

[71]   R. F. Steinhoff, J. Krismer, K. Eyer, S. R. Fagerer, A. Ibàñez, M. Pabst, R. Zenobi, Rapid estimation of the energy charge from cell lysates using matrix-assisted laser desorption/ionization mass spectrometry: Role of in-source fragmentation. *Anal. Biochem.* **2014**, *447*, 107.

[72]   S. G. Penn, H. Hu, P. H. Brown, C. B. Lebrilla, Direct analysis of sugar alcohol borate complexes in plant extracts by matrix-assisted laser desorption/ionization fourier transform mass spectrometry. *Anal. Chem.* **1997**, *69*, 2471.

[73]   G. Glauser, G. Marti, N. Villard, G. A. Doyen, J.-L. Wolfender, T. C. J. Turlings, M. Erb, Induction and detoxification of maize 1,4-benzoxazin-3-ones by insect herbivores. *Plant J.* **2011**, *68*, 901.

[74]   N. Smirnoff, G. L. Wheeler, Ascorbic Acid in Plants: Biosynthesis and Function. *Crit. Rev. Biochem. Mol. Biol.* **2000**, *35*, 291.

[75]   G. Agati, C. Brunetti, M. Di Ferdinando, F. Ferrini, S. Pollastri, M. Tattini, Functional roles of flavonoids in photoprotection: New evidence, lessons from the past. *Plant Physiol. Biochem.* **2013**, *72*, 35.

[76]   R. C. Gueldner, E. Snook Maurice, B. R. Wiseman, N. W. Widstrom, D. S. Himmelsbach, C. E. Costello, in *Naturally Occurring Pest Bioregulators, Vol. 449*, American Chemical Society, **1991**, pp. 251.

[77]   N. Sato, Roles of the acidic lipids sulfoquinovosyl diacylglycerol and phosphatidylglycerol in photosynthesis: their specificity and evolution. *J. Plant Res.* **2004**, *117*, 495.

[78]   A. Svatoš, Mass spectrometric imaging of small molecules. *Trends Biotechnol.* **2010**, *28*, 425.

[79]   K. E. Burnum, S. L. Frappier, R. M. Caprioli, Matrix-Assisted Laser Desorption/Ionization Imaging Mass Spectrometry for the Investigation of Proteins and Peptides. *Annual Review of Analytical Chemistry* **2008**, *1*, 689.

[80]   N. Goto-Inoue, T. Hayasaka, N. Zaima, M. Setou, Imaging mass spectrometry for lipidomics. *Biochim. Biophys. Acta* **2011**, *1811*, 961.

[81]   D. F. Smith, K. Aizikov, M. C. Duursma, F. Giskes, D. J. Spaanderman, L. A. McDonnell, P. B. O'Connor, R. M. Heeren, An external matrix-assisted laser desorption ionization source for flexible FT-ICR Mass spectrometry imaging with internal calibration on adjacent samples. *J. Am. Soc. Mass. Spectrom.* **2011**, *22*, 130.

[82] Y. Schober, T. Schramm, B. Spengler, A. Rompp, Protein identification by accurate mass matrix-assisted laser desorption/ionization imaging of tryptic peptides. *Rapid Commun. Mass Spectrom.* **2011**, *25*, 2475.

[83] C. D. Cerruti, F. Benabdellah, O. Laprévote, D. Touboul, A. Brunelle, MALDI Imaging and Structural Analysis of Rat Brain Lipid Negative Ions with 9-Aminoacridine Matrix. *Anal. Chem.* **2012**, *84*, 2164.

[84] D. Gode, D. A. Volmer, Lipid imaging by mass spectrometry - a review. *The Analyst* **2013**, *138*, 1289.

[85] L. S. Eberlin, C. R. Ferreira, A. L. Dill, D. R. Ifa, R. G. Cooks, Desorption electrospray ionization mass spectrometry for lipid characterization and biological tissue imaging. *Biochim. Biophys. Acta* **2011**, *1811*, 946.

[86] M. K. Passarelli, N. Winograd, Lipid imaging with time-of-flight secondary ion mass spectrometry (ToF-SIMS). *Biochim. Biophys. Acta* **2011**, *1811*, 976.

[87] J. S. Fletcher, J. C. Vickerman, N. Winograd, Label free biochemical 2D and 3D imaging using secondary ion mass spectrometry. *Curr. Opin. Chem. Biol.* **2011**, *15*, 733.

[88] F. Benabdellah, A. Seyer, L. Quinton, D. Touboul, A. Brunelle, O. Laprevote, Mass spectrometry imaging of rat brain sections: nanomolar sensitivity with MALDI versus nanometer resolution by TOF-SIMS. *Analytical and bioanalytical chemistry* **2010**, *396*, 151.

[89] T. Leefmann, C. Heim, S. Siljestrom, M. Blumenberg, P. Sjovall, V. Thiel, Spectral characterization of ten cyclic lipids using time-of-flight secondary ion mass spectrometry. *Rapid Commun. Mass Spectrom.* **2013**, *27*, 565.

[90] S. Sole-Domenech, P. Sjovall, V. Vukojevic, R. Fernando, A. Codita, S. Salve, N. Bogdanovic, A. H. Mohammed, P. Hammarstrom, K. P. Nilsson, F. M. LaFerla, S. Jacob, P. O. Berggren, L. Gimenez-Llort, M. Schalling, L. Terenius, B. Johansson, Localization of cholesterol, amyloid and glia in Alzheimer's disease transgenic mouse brain tissue using time-of-flight secondary ion mass spectrometry (ToF-SIMS) and immunofluorescence imaging. *Acta neuropathologica* **2013**, *125*, 145.

[91] K. Schuhmann, R. Almeida, M. Baumert, R. Herzog, S. R. Bornstein, A. Shevchenko, Shotgun lipidomics on a LTQ Orbitrap mass spectrometer by successive switching between acquisition polarity modes. *J. Mass Spectrom.* **2012**, *47*, 96.

[92] R. Knochenmuss, A quantitative model of ultraviolet matrix-assisted laser desorption/ionization. *J. Mass Spectrom.* **2002**, *37*, 867.

[93]   Bruker Daltonics, Inc., *The New ultrafleXtreme*. http://www.bruker.com/fileadmin/user_upload/8-PDF-Docs/Separations_MassSpectrometry/Literature/Brochures/ultrafleXtreme_Brochure_2012_eBook.pdf. **2012**. Accessed July 3, 2014.

[94]   A. Rompp, B. Spengler, Mass spectrometry imaging with high resolution in mass and space. *Histochemistry and cell biology* **2013**, *139*, 759.

[95]   A. Zavalin, J. Yang, R. Caprioli, Laser beam filtration for high spatial resolution MALDI imaging mass spectrometry. *J. Am. Soc. Mass. Spectrom.* **2013**, *24*, 1153.

[96]   C. Perrot-Rechenmann, M. Joannes, D. Squalli, P. Lebacq, Detection of phosphoenolpyruvate and ribulose 1,5-bisphosphate carboxylase transcripts in maize leaves by in situ hybridization with sulfonated cDNA probes. *J. Histochem. Cytochem.* **1989**, *37*, 423.

[97]   W. Majeran, Y. Cai, Q. Sun, K. J. van Wijk, Functional Differentiation of Bundle Sheath and Mesophyll Maize Chloroplasts Determined by Comparative Proteomics. *The Plant Cell Online* **2005**, *17*, 3111.

[98]   K. Strupat, V. Kovtoun, H. Bui, R. Viner, G. Stafford, S. Horning, MALDI Produced Ions Inspected with a Linear Ion Trap-Orbitrap Hybrid Mass Analyzer. *J. Am. Soc. Mass. Spectrom.* **2009**, *20*, 1451.

[99]   J. C. Jurchen, S. S. Rubakhin, J. V. Sweedler, MALDI-MS Imaging of Features Smaller than the Size of the Laser Beam. *J. Am. Soc. Mass. Spectrom.* **2005**, *16*, 1654.

[100]   N. Fabre, I. Rustan, E. de Hoffmann, J. Quetin-Leclercq, Determination of flavone, flavonol, and flavanone aglycones by negative ion liquid chromatography electrospray ion trap mass spectrometry. *J. Am. Soc. Mass. Spectrom.* **2001**, *12*, 707.

[101]   R. Turgeon, Phloem Loading: How Leaves Gain Their Independence. *BioScience* **2006**, *56*, 15.

[102]   T. Suzuki, S.-J. Kim, H. Yamauchi, S. Takigawa, Y. Honda, Y. Mukasa, Characterization of a flavonoid 3-O-glucosyltransferase and its activity during cotyledon growth in buckwheat (Fagopyrum esculentum). *Plant Science* **2005**, *169*, 943.

[103]   N. Sato, Roles of the acidic lipids sulfoquinovosyl diacylglycerol and phosphatidylglycerol in photosynthesis: their specificity and evolution. *J Plant Res* **2004**, *117*, 495.

[104]   P. G. Roughan, Phosphatidylglycerol and chilling sensitivity in plants. *Plant Physiol* **1985**, *77*, 740.

[105] J. R. Kenrick, D. G. Bishop, The Fatty Acid composition of phosphatidylglycerol and sulfoquinovosyldiacylglycerol of higher plants in relation to chilling sensitivity. *Plant Physiol* **1986**, *81*, 946.

[106] E. H. Seeley, R. M. Caprioli, 3D Imaging by Mass Spectrometry: A New Frontier. *Anal. Chem.* **2012**, *84*, 2105.

[107] C. Wu, A. L. Dill, L. S. Eberlin, R. G. Cooks, D. R. Ifa, Mass spectrometry imaging under ambient conditions. *Mass Spectrom. Rev.* **2013**, *32*, 218.

[108] P. J. Horn, A. R. Korte, P. B. Neogi, E. Love, J. Fuchs, K. Strupat, L. Borisjuk, V. Shulaev, Y. J. Lee, K. D. Chapman, Spatial mapping of lipids at cellular resolution in embryos of cotton. *The Plant cell* **2012**, *24*, 622.

[109] J. H. Jun, Z. Song, Z. Liu, B. J. Nikolau, E. S. Yeung, Y. J. Lee, High-Spatial and High-Mass Resolution Imaging of Surface Metabolites of Arabidopsis thaliana by Laser Desorption-Ionization Mass Spectrometry Using Colloidal Silver. *Analytical chemistry* **2010**, *82*, 3255.

[110] M. Burrell, C. Earnshaw, M. Clench, Imaging Matrix Assisted Laser Desorption Ionization Mass Spectrometry: a technique to map plant metabolites within tissues at high spatial resolution. *Journal of experimental botany* **2007**, *58*, 757.

[111] G. B. Yagnik, A. R. Korte, Y. J. Lee, Multiplex mass spectrometry imaging for latent fingerprints. *J. Mass Spectrom.* **2013**, *48*, 100.

[112] P. Chaurand, D. S. Cornett, P. M. Angel, R. M. Caprioli, From whole-body sections down to cellular level, multiscale imaging of phospholipids by MALDI mass spectrometry. *Mol. Cell. Proteomics* **2011**, *10*, O110 004259.

[113] A. R. Korte, Y. J. Lee, Multiplex mass spectrometric imaging with polarity switching for concurrent acquisition of positive and negative ion images. *J. Am. Soc. Mass. Spectrom.* **2013**, *24*, 949.

[114] Y. Chen, Y. Liu, J. Allegood, E. Wang, B. Cachon-Gonzalez, T. M. Cox, A. H. Merrill, Jr., M. C. Sullards, Imaging MALDI mass spectrometry of sphingolipids using an oscillating capillary nebulizer matrix application system. *Methods Mol Biol* **2010**, *656*, 131.